



University of Kentucky
UKnowledge

Theses and Dissertations--Physics and
Astronomy

Physics and Astronomy


2019

PROMPT FISSION NEUTRON ENERGY SPECTRUM OF $n+^{235}\text{U}$

Jason M. McGinnis

University of Kentucky, jasonmc5@yahoo.com

Author ORCID Identifier:

 <https://orcid.org/0000-0001-6587-0208>

Digital Object Identifier: <https://doi.org/10.13023/etd.2019.179>

[Right click to open a feedback form in a new tab to let us know how this document benefits you.](#)

Recommended Citation

McGinnis, Jason M., "PROMPT FISSION NEUTRON ENERGY SPECTRUM OF $n+^{235}\text{U}$ " (2019). *Theses and Dissertations--Physics and Astronomy*. 63.

https://uknowledge.uky.edu/physastron_etds/63

This Doctoral Dissertation is brought to you for free and open access by the Physics and Astronomy at UKnowledge. It has been accepted for inclusion in Theses and Dissertations--Physics and Astronomy by an authorized administrator of UKnowledge. For more information, please contact UKnowledge@lsv.uky.edu.

STUDENT AGREEMENT:

I represent that my thesis or dissertation and abstract are my original work. Proper attribution has been given to all outside sources. I understand that I am solely responsible for obtaining any needed copyright permissions. I have obtained needed written permission statement(s) from the owner(s) of each third-party copyrighted matter to be included in my work, allowing electronic distribution (if such use is not permitted by the fair use doctrine) which will be submitted to UKnowledge as Additional File.

I hereby grant to The University of Kentucky and its agents the irrevocable, non-exclusive, and royalty-free license to archive and make accessible my work in whole or in part in all forms of media, now or hereafter known. I agree that the document mentioned above may be made available immediately for worldwide access unless an embargo applies.

I retain all other ownership rights to the copyright of my work. I also retain the right to use in future works (such as articles or books) all or part of my work. I understand that I am free to register the copyright to my work.

REVIEW, APPROVAL AND ACCEPTANCE

The document mentioned above has been reviewed and accepted by the student's advisor, on behalf of the advisory committee, and by the Director of Graduate Studies (DGS), on behalf of the program; we verify that this is the final, approved version of the student's thesis including all changes required by the advisory committee. The undersigned agree to abide by the statements above.

Jason M. McGinnis, Student

Dr. Michael A. Kovash, Major Professor

Dr. Chris Crawford, Director of Graduate Studies

PROMPT FISSION NEUTRON ENERGY SPECTRUM OF $n+^{235}\text{U}$

DISSERTATION

A dissertation submitted in partial fulfillment of the
requirements for the degree of Doctor of Philosophy in the
College of Arts and Sciences
at the University of Kentucky

By
Jason M. McGinnis

Lexington, Kentucky

Director: Dr. Michael A. Kovash, Professor of Physics

Lexington, Kentucky

2019

Copyright© Jason M. McGinnis 2019

ABSTRACT OF DISSERTATION

PROMPT FISSION NEUTRON ENERGY SPECTRUM OF $n+^{235}\text{U}$

Despite nuclear fission prominence in nuclear physics, there are still several fundamental open questions about this process. One uncertainty is the energy distribution of neutrons emitted immediately after fission. In particular the relative energy distribution of neutrons above 8 MeV has been difficult to measure. This experiment measured the prompt neutron energy spectrum of $n+^{235}\text{U}$ from 3-10 MeV. The measurement took place at Los Alamos National Laboratory (LANL) and used a double time-of-flight technique to measure both the beam and fission neutron kinetic energies. Fission event timing was measured with a parallel plate avalanche counter. The fission neutron time-of-flight was measured with 2 m long plastic scintillation detectors. By combining the time-of-flight information with a known flight path the kinetic energy spectrum of neutrons was measured. To eliminate backgrounds various time-of-flight and energy cuts were imposed and an accidental coincidence background was subtracted. An MCNP simulation, including the 2 m neutron detector geometry, was done using the Madland and Nix model as the input energy distribution for the simulated neutrons. Finally, the measured energy spectrum was compared with the MCNP simulated $n+^{235}\text{U}$ fission neutron energy spectrum.

KEYWORDS: Prompt Fission Neutron Spectrum, Plastic Scintillation Detector, Neutron Detector, Monte Carlo Simulation

Jason M. McGinnis

Author

05/03/2019

Date

PROMPT FISSION NEUTRON ENERGY SPECTRUM OF $n+^{235}\text{U}$

By

Jason M. McGinnis

Michael A. Kovash

Director of Dissertation

Chris Crawford

Director of Graduate Studies

05/03/2019

Acknowledgements

This work would not have been possible without the significant contribution of several great people. I would like to thank everyone who helped me during my time as a graduate student.

Michael Kovash: Thank you for letting me figure things out on my own while sharing sage advice when I needed it. You helped me grow as a scientist and taught me the value of keeping good notes.

My Committee: Thank you all for offering guidance and criticism which lead me in the right direction.

Scott Meadows: Thank you for helping with development of the DAQ circuit. There were nearly 1000 connections and you sat there beside me as we puzzled over each one.

Matt Devlin: Thank you for being an excellent point of contact at LANL and bailing us out whenever the PPAC's gas handling system would malfunction.

WNR Staff: Thank you for helping move and assemble our detector setup. A special thanks to Tim Medina for being the go to hardware guy and Bill Waganaar for helping with electronics.

Steve Yates: Thank you for letting us use the Van de Graaff. I learned a great deal from my time in the basement tuning the beam and collecting data.

UK Machine and Electronics Shops: Thank you all for helping me build and repair the various components of this experiment.

Table of Contents

Acknowledgements	iii
List of Tables	vii
List of Figures	viii
1 Introduction	1
1.1 Introduction to Fission	1
1.1.1 Anatomy of Fission	1
1.1.2 Binding Energy and the Liquid Drop Model	2
1.1.3 Nuclear Potential and Fission Activation Energy	5
1.1.4 Deformation of Nucleus	7
1.2 Madland and Nix Model Calculation	7
1.2.1 Summary of Calculation	7
1.2.2 Maxwell and Watt Model Spectra	9
1.2.3 First-Chance Fission	9
1.2.4 Prompt Neutron Multiplicity	12
1.2.5 Multiple-Chance Fission	13
1.2.6 First-Chance Fission, with σ_c dependence	13
1.2.7 σ_c Independence through a_{eff}	14
1.2.8 Sensitivities of Madland and Nix model	16
1.3 Motivation	17
2 Detector Design and Properties	18
2.1 Neutron Detecting Bars	18

2.2	Bar Calibrations and Light Response	19
2.2.1	Energy Calibrations	20
2.2.2	Time Measurement and Calibration	25
2.3	Parallel Plate Avalanche Counter (PPAC)	28
3	Experimental Setup, Measurements and Observations	31
3.1	Detector Geometry at WNR 15L	32
3.2	Circuits and Data Acquisition	38
3.2.1	Circuit Diagrams and Discussion	39
3.2.2	Data Acquisition Details	54
4	Data Analysis	57
4.1	Analysis Summary	57
4.2	DAQ Triggers	60
4.2.1	Trigger Cuts	60
4.3	Neutron Beam Energy	63
4.4	Energy Deposition Analysis	65
4.5	Kinetic Energy Spectrum T(E)	67
4.6	Data Cuts	70
4.6.1	Sorting	71
4.7	Accidental Backgrounds	72
4.7.1	Accidental TOF Spectrum	72
4.7.2	Accidental Energy Spectrum	76
4.8	Coincident Backgrounds	78
4.9	Uncertainty Analysis	79
5	MCNP Simulations	82
5.1	MCNP Pre-Processor and ^{228}Th Simulation	82
5.2	^{252}Cf Simulation	87
5.3	Madland and Nix $n+^{235}\text{U}$ simulations	90

6	Results	93
6.1	^{252}Cf Analysis and Results	93
6.2	^{235}U Results	95
6.3	Conclusions	96
	Appendices	97
A	Appendix A: Neutron Bar Repair	97
	A.1 Repair	97
	A.2 Bar Testing	99
B	Appendix B: Neutron Bar Stand	102
	B.1 Stand Design Specifics	102
C	Appendix C: Proton Recoil	107
D	Appendix D: Fermi-Gas Model Calculation	109
	Bibliography	114
	Vita	115

List of Tables

1.1	Parameters used for $n+^{235}\text{U}$ fission calculation	16
3.1	Bar center position relative to PPAC center	34
4.1	Beam time-of-flight ranges	73

List of Figures

1.1	Binding energy as function of number of nucleons	3
1.2	Illustration of asymmetry in neutrons and protons	4
1.3	Simple model of nuclear potential well and Coulomb barrier	5
1.4	Fission activation energy as function of A	6
1.5	Illustration of fissioning nucleus using the liquid drop model	7
1.6	Madland and Nix calculated spectra overlay	15
1.7	Relative fission yield for various beam energies incident on the PPAC with a PPAC trigger cut	16
1.8	A PFNS measured by Noda et al	17
2.1	Sketch of how light propagates in a bar after an event	20
2.2	Example calibration spectrum from a single photo-tube	21
2.3	Example calibration fit	24
2.4	Compton edge channel number as a function of group number	24
2.5	Bar TOF spectrum with PPAC trigger cut	26
2.6	Time calibration spectrum	27
2.7	Rendering of the PPAC	29
2.8	Photo of the cylindrical PPAC assembly	30
3.1	The proton beam timing	32
3.2	Schematic of the relative distance along the beam line of the PPAC, fission chamber (FC) and beam dump.	33
3.3	Sketch of detector geometry at WNR 15L	35
3.4	The neutron bars on the stand in WNR 15L.	36

3.5	PPAC underneath the bar array with red arrow indicating where the beam emerges.	36
3.6	Close up of PPAC with pre-amps shown to the lower left.	37
3.7	Circuit diagram for a single bar. Arrows are used to indicate signal inputs.	40
3.8	A sketch of linear gate timing of gate and raw signals	41
3.9	BAR-OR circuit diagram.	43
3.10	Fast clear circuit diagram.	45
3.11	PPAC OR circuit diagram.	47
3.12	Trigger circuit	48
3.13	t0 copy circuit diagram	50
3.14	t0/Vramp circuit diagram	51
3.15	Pulser circuit diagram	53
3.16	Fission chamber circuit diagram	55
4.1	PPAC ADC histogram with a PPAC trigger cut but without a fission requirement.	61
4.2	PreBar cut beam neutron TOF to PPAC for a single bar.	62
4.3	PrePPAC trigger cut beam neutrons TOF to PPAC.	62
4.4	Fission chamber trigger cut beam TOF histogram.	63
4.5	Two beam TOF TDCs in a 2D histogram. This histogram shows the overlap between TDC_33 and TDC_34.	64
4.6	Beam TOF histogram with a PPAC trigger	65
4.7	Calibrated energy spectrum from a single PMT of a neutron bar	66
4.8	Geometric mean energy deposition of a single bar with a PreBar Beam-OFF trigger.	67
4.9	Position relative to center of bar with a PPAC trigger.	68
4.10	Meantime spectrum with a PPAC trigger requirement	69
4.11	Measured neutron kinetic energy spectrum for a single bar without background subtraction.	70

4.12	Meantime histogram of a single bar with PPAC trigger cut and energy threshold of 400 keVee.	71
4.13	Average beam frequency as a function of run number	72
4.14	Calculated accidental background TOF spectrum (pink) overlaid with a single bar meantime spectrum (blue).	75
4.15	Calculated accidental background spectrum in pink	76
5.1	Example PTRAC output file	83
5.2	A simulated Compton edge of a 2.6 MeV gamma ray for one PMT .	86
5.3	Simulated TOF spectrum with ^{252}Cf source	88
5.4	Simulated ^{252}Cf prompt fission neutron energy spectrum.	89
5.5	Energy via TOF vs energy deposition of a simulated ^{252}Cf source, with gamma rays turned off.	89
5.6	MN model source neutron energy distribution.	91
5.7	Simulated energy deposition vs ETOF using MN source neutrons. .	91
5.8	Simulated energy via tof spectrum with the MN input spectrum for beam energies between 1 and 5 MeV.	92
5.9	Neutron detection efficiency spectrum with 100 keV bins.	92
6.1	Energy deposition vs energy via TOF for a single bar	94
6.2	All 16 bars measured spectra compared with the ^{252}Cf MCNP simulation	94
6.3	^{235}U PFNS 1 to 5 MeV	95
6.4	^{235}U PFNS 5 to 10 MeV	95

Chapter 1

Introduction

1.1 Introduction to Fission

Nuclear fission is a radioactive decay process, by which unstable nuclei split, or fission usually into two smaller nuclei. Fission is either a spontaneous process or induced by an energetic particle such as a neutron or gamma ray. Nuclear fission is highly energetic, releasing on the order of 200 MeV per fission. This energy is divided among the various secondary particles created during fission, as well as the kinetic energy of the two fission fragments. The secondary particles created by fission are neutrons and gamma rays. These particles, under the right conditions, can induce more fission events creating a chain reaction. These chain reactions can lead to large releases of energy, enough to drive power plants. However, despite nuclear fission looming large in the public eye there are gaps in the understanding of some of its finer points.

1.1.1 Anatomy of Fission

Before fission can begin a fissile nucleus needs enough energy to overcome the fission barrier. For some isotopes, such as ^{252}Cf , getting through the fission barrier requires no outside energy. These nuclei are said to undergo spontaneous fission. That is, there is no need to add extra energy to get the nucleus to fission. For most fissile nuclei some external energy is needed. Usually extra energy is supplied by a neutron or sometimes a gamma ray. This extra energy excites the nucleus allowing it to undergo fission.

After fissioning a few things happen on a very short timescale. First it is important to recognize that the fission fragments are in an excited state. These fragments are excited due to an excess of neutrons and an excess of binding energy left over from the less tightly bound initial nucleus. The excited fragments emit neutrons and gamma rays, at the instant of fission, in order to reach a more stable state. These neutrons and gamma rays are referred to as prompt neutrons and prompt gamma rays.

Finally, after emitting prompt secondary particles the fragments continue to decay via beta and gamma decay. The fastest of these decays typically occur on the order of nanoseconds after fission. Later, isotopes in the decay chain have longer half-lives on the order of minutes to days.

1.1.2 Binding Energy and the Liquid Drop Model

Fission occurs because there is a large difference in the binding energy between the fissile nucleus and the resulting fission fragments. The binding energy B of a given nucleus of mass $m_{nucleus}$ (MeV), with N neutrons of mass $m_n=939.57$ MeV and Z protons of mass $m_p=938.27$ MeV, is calculated using equation 1.1.

$$B = m_n N + m_p Z - m_{nucleus} \quad (1.1)$$

Typically the difference in binding energy before and after fission is around 200 MeV. This large change in binding energy is much greater than what is achieved via alpha decay or any other available decay process. While equation 1.1 is an effective way to calculate the binding energy from known nuclear masses, it does not yield any understanding as to why some nuclei are more tightly bound than others, nor does it provide any structure towards understanding a process like fission. The

semi-empirical mass formula, equation 1.2, is a model fit of nuclear binding energy.

$$B(Z, A) = a_v A - a_s A^{2/3} - a_c Z(Z - 1)A^{-1/3} - a_{sym} \frac{(A - 2Z)^2}{A} \pm \delta$$

$$\delta = +a_p A^{-3/4} \text{ if } N \text{ and } Z \text{ are even}$$

$$\delta = -a_p A^{-3/4} \text{ if } N \text{ and } Z \text{ are odd} \tag{1.2}$$

$$\delta = 0 \text{ if } A \text{ is odd}$$

$$a_v=15.5 \text{ MeV } a_s=16.8 \text{ MeV } a_c=0.72 \text{ MeV } a_{sym}=23 \text{ MeV } a_p=34.0 \text{ MeV}$$

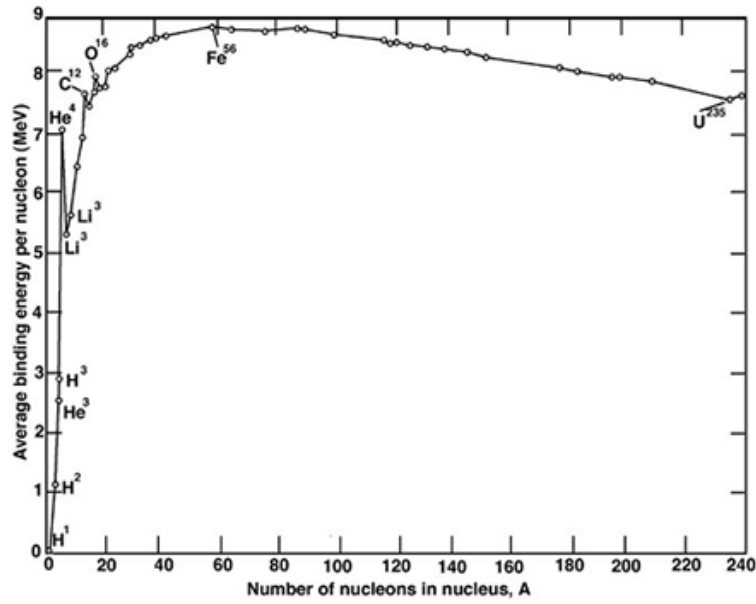


Figure 1.1: Binding energy as function of number of nucleons[1]

The semi-empirical mass formula is also referred to as the liquid drop model. By breaking the semi-empirical mass formula down term by term, it is possible to see the differences and similarities between the binding energy equation 1.2 and a liquid drop. The first term is a volume term, derived from the fact that the nuclear strong force is local, meaning only the nearest neighbor nucleons interact. This leads to a linear relationship with A, as each nucleon feels the same binding energy due to the strong force. The surface term is a correction for the fact that nucleons at the surface do not have as many neighbors as do nucleons in the bulk. These surface nucleons are less tightly bound, thus the correction subtracts from the

overall binding energy. These first two terms are thought of as analogs to a dipole-dipole attraction and surface tension in a drop of water. The Coulomb interaction of protons is repulsive and thus also subtracts from the overall binding energy. This term represents an averaging of what each proton experiences. Since the Coulomb interaction is long range each proton is subject to a force from each other proton. Thus the $(Z-1)A^{-1/3}$ dependence. This term is the charged portion of the charged liquid drop. As stated earlier the last two terms are quantum mechanical in nature. The symmetry term “encourages” the number of neutrons and protons to be equal, by reducing the binding energy proportional to the asymmetry between protons and neutrons. This is due to the shell model structure of the nucleus. Much like atomic orbitals, nucleons have discrete energy levels that they occupy while obeying the Pauli-exclusion principle. Figure 1.2 shows a cartoon to help visualize why symmetry lowers the overall binding energy. If you begin with an equal number of neutrons and protons, then convert some protons into neutrons, those neutrons must occupy the available higher energy states.

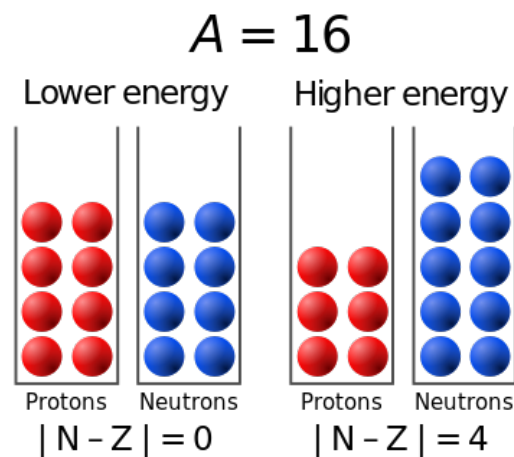


Figure 1.2: Illustration of asymmetry in neutrons and protons[2]. Note that as protons are turned into neutrons, the neutrons must occupy higher energy states than the protons did in the symmetric case.

Lastly, the δ term is the pairing term. This term arises from the fact that spin-1/2 particles of opposite spin tend to pair up before occupying higher energy levels. However, it is important to note that these last two terms are only affected

by the makeup of the nucleus and thus do not play a role in any deformation.

1.1.3 Nuclear Potential and Fission Activation Energy

While fission is possible in many heavy nuclei, it does not happen readily. This is due to the Coulomb barrier illustrated in figure 1.3.

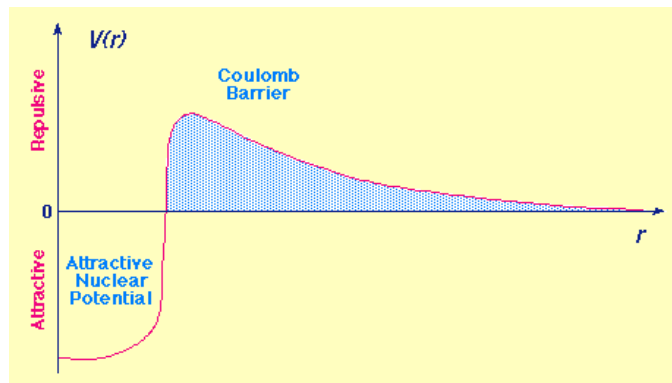


Figure 1.3: Simple model of nuclear potential well and Coulomb barrier [3]. r is the separation between fission fragments, and $V(r)$ is the height of the barrier. A nucleus with sufficiently high energy can tunnel through the barrier and spontaneously fission. This is most likely to happen with mass numbers larger than 250.

The strong force creates a potential well from $r=0$ to some characteristic separation r_n . For $r>r_n$ the interaction is dominated by the Coulomb potential. As the number of nucleons increases the potential well decreases its depth. This is due to a combination of the increasing number of protons creating an outward force and a relative reduction in the surface tension. For nuclei with mass numbers greater than 250, the potential well becomes shallow enough that it is possible for a fragment of the nucleus to tunnel through the Coulomb barrier. When this happens the two fragments are accelerated by Coulomb repulsion and spontaneous fission occurs. For lighter nuclei, tunneling of a fragment through the barrier is only possible if the nucleus captures an energetic particle such as a neutron or gamma ray. This can add enough energy to the system to induce fission. For some nuclei such as ^{235}U adding a neutron will both add energy to the system and effectively lower the fission barrier by raising the binding energy. The binding energy in ^{235}U goes up due to the pairing term in the semi-empirical mass formula. ^{236}U has even-even

pairing and thus adds the pairing term to its binding energy. By doing so ^{236}U has a lower energy ground state and thus is more excited than if a similar energy gamma ray had been absorbed by the original ^{235}U . ^{238}U absorbing a neutron has the exact opposite effect. When ^{238}U captures a neutron it goes from even-even to odd which means its ground state is actually higher in energy. Thus the excitation energy is actually lower than if ^{238}U were to absorb a similarly energetic gamma ray.

The amount of energy needed to overcome the fission barrier is called the activation energy. Figure 1.4 shows the activation energy as a function of A for the most stable nuclei. Stable nuclei above A=200 have a Z/A ratio of around 0.41. The barrier is very small above A=230 – on the order of 5 MeV. The lighter curve in figure 1.4 is the same as the darker curve, just with shell model corrections added. These corrections create peaks in activation energy around shell closures. These shell closures are analogous to filling atomic orbitals and create extra stable nuclei, which is why there is a spike in activation energy near these closures.

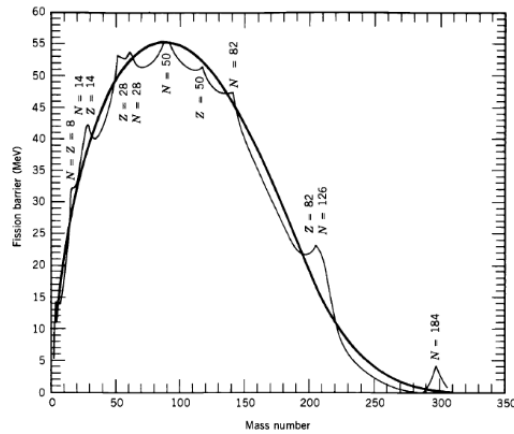


Figure 1.4: Fission activation energy as function of A[1]. Thick black line is liquid drop model while the thinner line has shell model corrections added. Notice that as A increases the barrier gets smaller provided $A > 100$. For each value of A a certain Z/A ratio is assumed. This means that activation energy is a function of not just A but also Z.

1.1.4 Deformation of Nucleus

The liquid drop model provides a useful framework for dealing with the effects of nuclear deformations. A common deformation is to stretch a spherical nucleus into an ellipsoid. The distance R from the center of an ellipsoid to its surface is given by equation 1.3.

$$\begin{aligned} R &= R_o(1 + \beta P_2(\cos(\theta))) \\ P_2(\cos(\theta)) &= \frac{3\cos(\theta)^2 - 1}{2} \end{aligned} \tag{1.3}$$

Where R_o is the average distance to the surface and the angle θ is measured from the semi-major axis. The eccentricity given by $\epsilon = \beta\sqrt{\frac{5}{4\pi}}$ is a useful parameter for finding the major and minor axes given by $a = (1 + \epsilon)R_o$ and $b = \frac{R_o}{\sqrt{1 + \epsilon}}$. Note that, since $ab^2 = 1$ the volume of the nucleus $V = ab^2(\frac{4}{3}\pi R_o^3) = \frac{4}{3}\pi R_o^3$ is unchanged by this deformation. As the eccentricity increases the surface area of the nucleus also increases along with the average distance between protons. Eventually as the surface of the nucleus becomes large enough, and the proton repulsion small enough, fission will occur. This gives a useful way to envision fission as a drop that is deformed until the forces holding the two halves together give way and two separate drops form. This is illustrated in fig1.5.

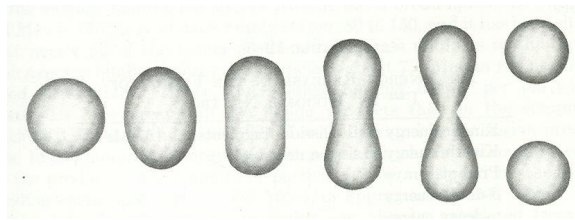


Figure 1.5: Illustration of fissioning nucleus using the liquid drop model.

1.2 Madland and Nix Model Calculation

1.2.1 Summary of Calculation

The Madland and Nix (MN) model predicts the prompt fission neutron spectrum (PFNS) for a given isotope and excitation energy. The MN model is an example

of an evaporation model. Evaporation models treat the fission fragments as having high temperatures that then cool by emitting neutrons. The center-of-mass temperature-dependent distribution $\phi(\epsilon, T)$ describes the energy spectrum of the evaporated neutrons of energy ϵ . The probability of a neutron having temperature T is given by the triangular probability distribution $P(T)$. The maximum temperature T_m the neutrons are allowed is found by applying the Fermi gas model. The temperature-independent center-of-mass energy spectrum $\Phi(\epsilon)$ is obtained by integrating the product of $P(T)$ and $\phi(\epsilon, T)$ over T from 0 to T_m . The fission fragment is assumed to have a kinetic energy of $A_f \cdot E_f$ where A_f is the mass number of the fragment and E_f is the average kinetic energy per nucleon. The value of E_f for each fragment is obtained from the use of energy and momentum conservation. The spectrum $\Phi(\epsilon)$ is then transformed from the center-of-mass frame into the lab frame where the neutron energy E is measured. This is done by integrating $\Phi(\epsilon)$ over ϵ from $(\sqrt{E} - \sqrt{E_f})^2$ to $(\sqrt{E} + \sqrt{E_f})^2$. The lab-frame energy spectrum is the PFNS of a fragment $N(E, E_f)$. The average of the heavy and light fragment's $N(E, E_f)$ is taken and this gives the final PFNS of the initial nucleus $N(E)$.

This spectrum of $N(E)$ is only valid for first-chance fission and must be modified for multiple-chance fission. First-chance fission is when the nucleus fissions after capturing a neutron but without emitting any neutrons before fission. Multiple-chance fission occurs when the nucleus, after capturing a neutron, emits one or more neutrons before fission. The most common multiple-chance fissions are 2nd and 3rd chance fission where one and two neutrons respectively are emitted from the nucleus. The probability of, 1st, 2nd and 3rd chance fission $P_1(E_n)$, $P_2(E_n)$ and $P_3(E_n)$, are calculated as a function of beam energy E_n by Madland and Nix[4]. To calculate the final PFNS when multiple-chance fission is involved the PFNS $N(E)$ is calculated for each chance of fission 1st, 2nd and 3rd. For the 1st chance case $N_1(E)$ is calculated as before but for the 2nd and 3rd chance cases the excitation energy of the system is reduced. The energy reduction ΔE_1 for 2nd chance fission, is equal to the binding energy $B_n(A-1)$ plus $\langle \epsilon_1 \rangle$, the average

emitted neutron energy. The energy $\langle \epsilon_1 \rangle$ is found by calculating the first moment of the center-of-mass spectrum $\Phi(\epsilon)$ with respect to ϵ . The excitation energy reduction ΔE_2 for 3rd chance fission is the sum of ΔE_1 , $B_n(A-2)$ and $\langle \epsilon_2 \rangle$ which is found the same way as for 2nd chance except A goes to $A-1$. Finally, the total PFNS $N(E)$ is found by taking the average of $N_1(E)$, $N_2(E)$, and $N_3(E)$, weighted by their respective probabilities.

1.2.2 Maxwell and Watt Model Spectra

Before Madland and Nix (MN)[4], fission neutron spectra were first measured, then fit to either a Watt or Maxwell spectrum. The Watt spectrum $W(E)$, given by equation 1.4, as a function of fission neutron energy E and fit parameters a , b , and C .

$$W(E) = C * \exp(-a * E) * \sinh(\sqrt{b * E}) \quad (1.4)$$

This method of characterizing a prompt neutron spectrum is still used in popular simulation codes like MCNP5. That is because equation 1.4 is easy to use and the parameters a and b are well known for common fission nuclei such as ^{235}U . However, a drawback to this approach is, there is no way to deduce the parameters a and b without first measuring the neutron spectrum in question. This becomes quite the limitation due to the large number of fissile nuclei and the fact that most have very short half lives and are difficult to produce large enough samples to do a measurement. A better approach is to develop a model that uses inputs such as mass number and beam energy to predict the prompt fission neutron spectrum (PFNS) of a given nuclei. The MN model is an example of such a model.

1.2.3 First-Chance Fission

The advantage of the MN or Los Alamos model over other approaches to calculating prompt fission neutron energy distributions is its predictive power. Watt and

Maxwellian fits are good for interpolating data but cannot estimate unmeasured fission neutron spectra. Detailed in this section is how to calculate the MN prompt fission neutron spectrum $N(E)$ for first-chance fissions. First-chance fissions are, as their name suggests, fission events where fission occurs before any neutrons are emitted. This is in contrast to multiple-chance fission where the incident neutron has enough energy to cause the compound nucleus to emit neutrons before undergoing fission. The average total excitation energy of the fissioning nucleus $\langle E^* \rangle$, is the energy available to the prompt neutrons[4]. The average energy release per fission $\langle E_r \rangle$ is the average sum of the energy of all the secondary particles emitted after fission and the average total kinetic energy of the fragments $\langle E_f^{tot} \rangle$. The binding energy per nucleon B_n is how much energy is needed to remove one nucleon from the nucleus. The incident neutron energy E_n is the kinetic energy of the neutron that induced fission. The excitation energy E^* in terms of $\langle E_r \rangle$, $\langle E_f^{tot} \rangle$, B_n , and E_n is given by equation 1.5.

$$\langle E^* \rangle = \langle E_r \rangle + B_n + E_n - \langle E_f^{tot} \rangle \quad (1.5)$$

The center-of-mass prompt fission neutron energy spectrum is given by equation 1.6, in terms of the center-of-mass neutron energy ϵ and the fragment's nuclear temperature T [5].

$$\phi(\epsilon) = \frac{\epsilon}{T^2} \exp\left(-\frac{\epsilon}{T}\right) \quad (1.6)$$

The nuclear temperature T is obtained from the excitation energy E^* and the level density parameter a from equation 1.7. This equation is a result from the Fermi-gas model description[4][6] of a nucleus made up of non-interacting neutrons and protons. The derivation of equation 1.7 is done in appendix D.

$$E^* = aT^2 \quad (1.7)$$

The maximum temperature T_m is given by equation 1.8 and is the maximum temperature allowed by the temperature distribution $P(T)$.

$$T_m = \sqrt{\frac{\langle E^* \rangle}{a}} \quad (1.8)$$

The distribution $P(T)$ was first obtained by Terrell[7] by looking at experimental data for various fission fragment kinetic energies and applying equation 1.7. The resultant $P(T)$ was mostly triangular with just a slight tail at $T > T_m$. However, a sharp cutoff is imposed at T_m instead of allowing $P(T)$ to tail off. This creates a triangular distribution that makes calculations simpler with little effect on the final $N(E)$ distribution. The level density parameter a is $a = \frac{A}{11\text{MeV}}$

$$P(T) = \begin{cases} \frac{2T}{T_m^2} & 0 \leq T \leq T_m \\ 0 & T > T_m \end{cases} \quad (1.9)$$

The center-of-mass neutron energy spectrum $\Phi(\epsilon)$ is given by equation 1.10, with the exponential integral given by $E_1(x) = \int_0^\infty \frac{\exp(-t)}{t} dt$.

$$\begin{aligned} \Phi(\epsilon) &= \int_0^\infty \phi(\epsilon) P(T) dT = \frac{2\epsilon}{T_m^2} \int_0^{T_m} \frac{\exp(-\frac{\epsilon}{T})}{T} dT \\ &= \frac{2\epsilon}{T_m^2} E_1\left(\frac{\epsilon}{T_m}\right) \end{aligned} \quad (1.10)$$

Since fission fragments are not stationary in the lab frame, the center-of-mass neutron energy spectrum needs to transform into the lab frame. This is done by integrating $\Phi(\epsilon)$ over all possible velocities, as shown by equation 1.11.

$$N(E, E_f) = \frac{1}{4\sqrt{E_f}} \int_{(\sqrt{E}-\sqrt{E_f})^2}^{(\sqrt{E}+\sqrt{E_f})^2} \frac{\Phi(\epsilon)}{\sqrt{\epsilon}} d\epsilon \quad (1.11)$$

After calculating the integral, the individual fragment prompt fission neutron spectrum $N(E, E_f)$ is given by equation 1.12.

$$N(E, E_f) = \frac{1}{3\sqrt{E_f T_m}} [u_+^{\frac{3}{2}} E_1(u_+) - u_-^{\frac{3}{2}} E_1(u_-) + \gamma(\frac{3}{2}, u_+) - \gamma(\frac{3}{2}, u_-)] \quad (1.12)$$

With $u_{\pm} = \frac{(\sqrt{E} \pm \sqrt{E_f})^2}{T_m}$ and $\gamma(t, x) = \int_0^x u^{t-1} \exp(-u) du$. The fragment kinetic energy E_f , of the heavy and light fragments, is obtained via conservation of momentum. If En is small compared to the rest mass of both fragments, which is reasonable for beam neutrons below 20 MeV, then the fragment energies E_f^L and E_f^H are obtained by equation 1.13, where A_L and A_H are the average mass numbers of the light and heavy fragments, and A is the mass number of the fissioning compound nucleus.

$$\begin{aligned} E_f^L &= \frac{A_H}{A_L} \frac{\langle E_f^{tot} \rangle}{A} \\ E_f^H &= \frac{A_L}{A_H} \frac{\langle E_f^{tot} \rangle}{A} \end{aligned} \quad (1.13)$$

Finally, by assuming each fragment has a roughly equal chance of emitting prompt fission neutrons, the PFNS of the fissioning nucleus $N(E)$ is found by equation 1.14.

$$N(E) = \frac{N(E, E_f^L) + N(E, E_f^H)}{2} \quad (1.14)$$

1.2.4 Prompt Neutron Multiplicity

The average neutron multiplicity $\bar{\nu}_p$ is the average number of neutrons emitted during fission. The average energy of these emitted neutrons $\langle \eta \rangle$ is the sum of the separation energy $\langle S_n \rangle$ and the average center-of-mass energy $\langle \epsilon \rangle$ as shown in equation 1.15.

$$\langle \eta \rangle = \langle S_n \rangle + \langle \epsilon \rangle \quad (1.15)$$

Thus the total excitation energy E^* , given by equation 1.16 is the sum of these neutron energies and the average total energy from gamma-ray emission $\langle E_\gamma^{tot} \rangle$.

$$\langle E^* \rangle = \bar{\nu}_p \langle \eta \rangle + \langle E_\gamma^{tot} \rangle \quad (1.16)$$

Rearranging equation 1.16 yields the average neutron multiplicity $\bar{\nu}_p$ given by equation 1.17.

$$\bar{\nu}_p = \frac{\langle E^* \rangle - \langle E_\gamma^{tot} \rangle}{\langle S_n \rangle + \langle \epsilon \rangle} \quad (1.17)$$

1.2.5 Multiple-Chance Fission

At incident neutron energies above 6 MeV multiple-chance fission becomes a possibility. To account for this equation 1.18 is employed. P_{fi} represent the i 'th chance at fission probability. These values were taken from table IV of the Madland and Nix paper [4]. The other values are calculated using equations 1.6, 1.20, and 1.17 using parameters appropriate for the changing mass number between chance fissions.

$$N(E) = \frac{P_{f1}^A \bar{\nu}_{p1} N_1(E) + P_{f2}^A (\phi_1(E) + \bar{\nu}_{p2} N_2(E)) + P_{f3}^A (\phi_1(E) + \phi_2(E) + \bar{\nu}_{p3} N_3(E))}{P_{f1}^A \bar{\nu}_{p1} + P_{f2}^A (1 + \bar{\nu}_{p2}) + P_{f3}^A (2 + \bar{\nu}_{p3})} \quad (1.18)$$

1.2.6 First-Chance Fission, with σ_c dependence

Introducing the neutron capture cross section σ_c modifies the method of calculation of $N(E)$. The functional dependence of σ_c on ϵ is found via a cubic spline fit of capture cross section data[4]. If σ_c is dependent on the center-of-mass neutron energy ϵ then, equation 1.12 becomes equation 1.19.

$$N(E, E_f, \sigma_c) = \frac{1}{2T_m^2 \sqrt{E_f}} \int_{(\sqrt{E}-\sqrt{E_f})^2}^{(\sqrt{E}+\sqrt{E_f})^2} \sigma_c(\epsilon) d\epsilon \int_0^{T_m} k(T) T \exp\left(\frac{-\epsilon}{T}\right) dT \quad (1.19)$$

The normalization factor $k(T)$ eliminates the dependence of $N(E, E_f)$ on the magnitude of σ_c . Instead $N(E, E_f)$ only depends on the shape of σ_c 's dependence on ϵ .

$$k(T) = \left(\int_0^\infty \sigma_c(\epsilon) \epsilon \exp\left(\frac{-\epsilon}{T}\right) d\epsilon \right)^{-1} \quad (1.20)$$

While it is possible to calculate $N(E, E_f, \sigma_c)$ using the above equations it is impractical. This is due to σ_c 's piecewise nature combined with the need to carry out the double integral numerically. The computation times are very long on the order of an hour for each bin with fission neutron energy bin sizes of 100 keV. The computation time is reduced by introducing an approximate model of σ_c instead of the fitted piecewise function. However, this introduces uncertainties that are avoided by an alternative approach that encapsulates the effects of σ_c without including it directly in the calculation. This approach is covered in the next section.

1.2.7 σ_c Independence through a_{eff}

At energies above 6 MeV the PFNS is sensitive to a but at low energies are not very sensitive to a . The effects of σ_c on the calculation are then approximated by a changing a to a_{eff} . The value of a_{eff} is found by substituting a_{eff} for a in equation 1.12, and then tuning a_{eff} to fit a neutron spectrum for one value of E_n , usually thermal neutrons as there is a lot of good data available. For ^{235}U the value of a_{eff} as a function of mass number A , is given by equation 1.21.

$$a_{eff} = \frac{A}{10 \text{ MeV}} \quad (1.21)$$

This calculated spectrum is used as an input energy spectrum for our MCNP simulations. These simulations are meant to simulate integrated 1-5 and 5-10 MeV beam energy bins. Therefore, the $N(E)$ calculated spectrum for each beam energy E_n from 0 to 10 MeV, were divided into 1-5 and 5-10 MeV groups. Prompt fission neutron spectra with explicit beam energy dependence $N(E, E_n)$ were used

to calculate a resultant PFNS for each group of beam energies. Figure 1.6 shows an overlay of the various $N(E, E_n)$.

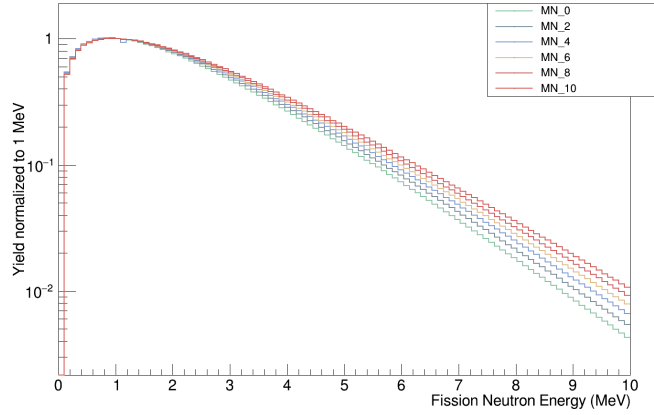


Figure 1.6: This figure is an overlay of various E_n MN model calculation neutron spectra for $n+^{235}\text{U}$. The beam energy E_n is denoted at the end of each label, for example MN_2 has $E_n=2$ MeV.

The 1-5 MeV PFNS $N(E)_{1-5}$ is given by equation 1.22, and 5-10 MeV is given by 1.23.

$$N(E)_{1-5} = \frac{\sum_{E_n=1}^5 w(E_n) * N(E, E_n)}{\sum_{E_n=1}^5 w(E_n)} \quad (1.22)$$

$$N(E)_{5-10} = \frac{\sum_{E_n=5}^{10} w(E_n) * N(E, E_n)}{\sum_{E_n=5}^{10} w(E_n)} \quad (1.23)$$

The weight factors $w(E_n)$ are obtained by integrating the average $n+^{235}\text{U}$ fission rate over beam energies $E_n - 0.5$ MeV to $E_n + 0.5$ MeV. Figure 1.7 shows the fission yield as a function of E_n .

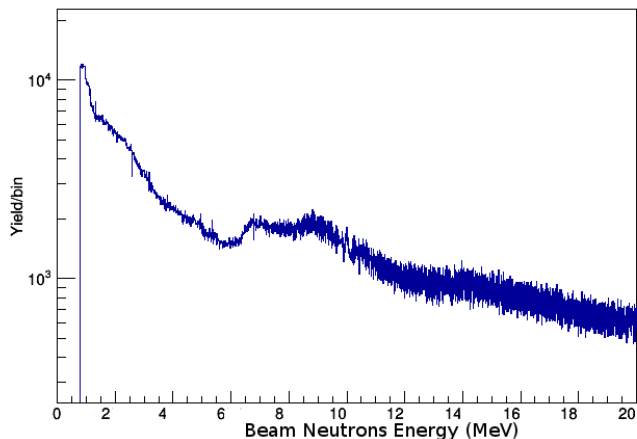


Figure 1.7: Relative fission yield for various beam energies incident on the PPAC with a PPAC trigger cut. This data was collected using the DAQ described in Chapter 3.

Our own data was used here because the fission rates at various neutron beam energies needed to match what was actually collected during the experiment at WNR 15L.

1.2.8 Sensitivities of Madland and Nix model

The MN model has several inputs, only a few of which are controlled during an experiment such as the beam energy and atomic number of the fissioning nucleus. The rest are a function of the nucleus itself and the fission process. The effects of changing nuclear excitation energy $\langle E^* \rangle$ are shown in figure 1.6. Assuming the level density parameter a and mass ratio of the heavy and light fission fragments, then it is possible to extract $\langle E^* \rangle$ from the measured PFNS by fitting the model to the measured spectrum.

Table 1.1: Parameters used for $n+^{235}\text{U}$ fission calculation

Input Variable	Value
A_L	96
A_H	140
A	236
$\langle E_r \rangle$	186.98 MeV
$\langle E_f^{tot} \rangle$	171.8 MeV
B_n	6.546 MeV
a_{eff}	23.6 MeV

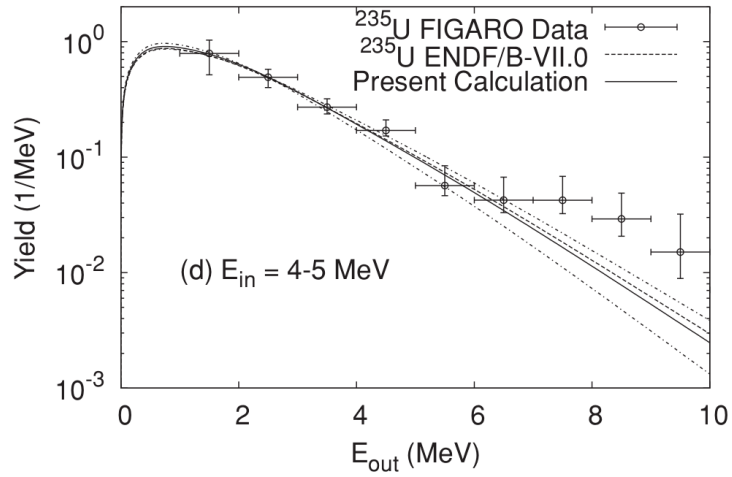


Figure 1.8: A PFNS measured by Noda et al.[9] showing divergence from the MN model.

1.3 Motivation

Prompt fission neutron spectra (PFNS) are important inputs in many fission related applications, such as simulations of nuclear fuel assemblies. However, there are large uncertainties in the measured PFNS of important isotopes such as ^{235}U , particularly above 6 MeV and below 500 keV [8]. Further, even more recent measurements of PFNS of ^{235}U have yielded results that do not agree with the MN model[9]. Fig1.8 demonstrates such a disagreement. Thus measuring, and comparing to the MN model, the PFNS above 6 MeV is the priority of this work.

Chapter 2

Detector Design and Properties

2.1 Neutron Detecting Bars

The neutron bars (or referred to as “bars”) are 2 m 10 cm x 10 cm BC-408[10] plastic scintillating detectors. The scintillator was produced by Bicron. The bars are flanked on each end by a light guide and a photomultiplier tube (PMT)[11]. When a neutron or gamma ray enters the detector there is a chance to interact with the material. Gamma rays will Compton scatter, leaving a recoiling electron. While neutrons will usually scatter off of a proton, causing the proton to recoil. They can instead scatter off of a carbon nucleus. In that case they create a recoil, which may be in the 2^+ state, thus creating a 4.4 MeV gamma ray[12]. The effects of these gamma rays on the detection efficiency are covered in Chapter 5. The charged particles created by neutron and gamma ray interactions generate light which is collected by the PMTs. The PMT anode then generates an electric signal pulse that is analyzed by the data acquisition system (DAQ). This electric signal pulse is referred to as a raw signal. The time it takes for a signal to go from 10% to 90% of its maximum voltage is called the rise time. For the neutron bars the rise time is approximately 5 ns. The max voltage of a signal pulse depends on the energy deposited in the detector. The range of voltages in the detectors was 100 mV to 3 V for most signals. Cosmic-ray backgrounds produce much higher maximum voltages. The integral of the voltage over time for a signal pulse is a function of the energy deposited.

2.2 Bar Calibrations and Light Response

There are a few subtleties that arise from using long scintillators. Light generated by interactions in a scintillator travels initially in a random direction. The light is then guided to either end of the bar by total internal reflection. On average an event will divide half the light between each end of the bar. The PMTs on end of the bars are physically labeled either “TOP” or “BOTTOM”, but since the bars are parallel to the ground in this experiment we will refer to them as “left” and “right”. The amount of light that reaches each end is not just determined by how many photons travel in that direction. The effects of light attenuation reduce the number of photons that reach each PMT. The attenuation length of BC-408 plastic scintillator is about 2 m. The light attenuation effect is corrected for in the data. This is due to the fact that the amount of light that reaches either end is attenuated, which is modeled by equation 2.1. Where N_{side} is the amount of light that reaches one PMT either left or right, $N_{0,side}$ is the initial amount of leftward or rightward light, λ represents the attenuation length, L is the bar length of 2 m, and x is the distance from left PMT.

$$\begin{aligned} N_{left} &= N_{0,left} * e^{-\frac{x}{\lambda}} \\ N_{right} &= N_{0,right} * e^{-\frac{L-x}{\lambda}} \end{aligned} \tag{2.1}$$

Figure 2.1 is a sketch of how the light propagates inside the bar after an event. It is important to note that on average $N_{0,left} = N_{0,right} = N_0/2$ where N_0 is the total number of photons generated by an event. The geometric mean N_{geo} of N_{left} and N_{right} is independent of x as shown in equation 2.2.

$$\begin{aligned} N_{geo} &= \sqrt{N_{left} * N_{right}} \\ N_{geo} &= \sqrt{N_{0,left} * N_{0,right} * e^{-\frac{x-x-L}{\lambda}}} \\ N_{geo} &= \sqrt{N_{0,left} * N_{0,right} e^{-\frac{L}{\lambda}}} \end{aligned} \tag{2.2}$$

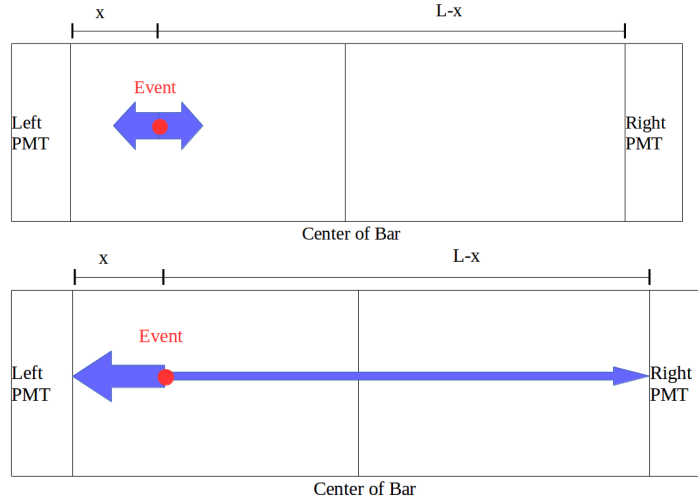


Figure 2.1: Sketch of how light propagates in a bar after an event (red) at position x . The photons are represented by blue arrows with the width of the arrow indicating how many photons are heading in that direction. The top figure shows that right after the event the amount of light going left vs right is about equal. The bottom image shows the effect of light attenuation after the light reaches the PMTs at either side with the right side receiving less light than the left.

Equation 2.2 shows that the geometric mean, light response is the same as if the event occurred in the center of the bar. The center of the bar has $x = L/2$. This position has the property that if a gamma-ray source is placed there then, similar amounts of light will reach both tubes. This is exploited when calibrating PMT pulse height by placing a gamma-ray source at the center of the bar. This ensures both PMTs will on average measure the same number of photons from events caused by the gamma source. Each PMT will measure an average number of photons $\frac{N_0}{2} * e^{-\frac{L}{2\lambda}}$ per event which is the same amount of light as N_{geo} measures. Thus by calibrating the PMT pulse height using gamma sources at the center of the bar the geometric mean is also calibrated.

2.2.1 Energy Calibrations

Gamma-ray sources, particularly sources with strong isolated peaks, make for good calibrations. Gamma rays Compton scatter inside of plastic scintillators. Equation 2.3 determines the energy of an electron recoil E_e for any incident gamma-ray

energy E_γ , with θ representing the angle between the scattered gamma ray and the axis parallel to the incident gamma ray.

$$E_e = E_\gamma \left(1 - \frac{1}{1 - \frac{E_\gamma}{m_e} (1 - \cos(\theta))} \right) \quad (2.3)$$

An energy maximum occurs at $\theta = \pi$. This maximum is called the Compton edge, and is always lower in energy than the original gamma-ray energy. In the bar detectors, instead of a sharp cutoff there is a more gradual slope, albeit much more sharp than the surrounding exponential background. Fig. 2.2 demonstrates this.

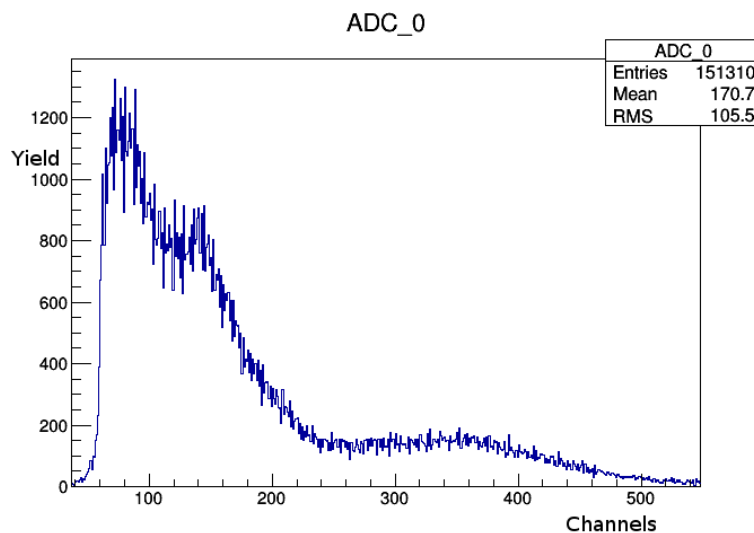


Figure 2.2: Example calibration spectrum from a single photo-tube. The source is uncollimated ^{22}Na which produces both 511 keV and 1.27 MeV gamma rays. Below channel 200 the dominate feature is the Compton edge created by the 511 keV gamma rays; above channel 400 is a Compton edge created by 1.27 MeV gammas.

A simple but reliable method to energy calibrate using Compton edges is to measure the channel number of the Compton edge. The channel number of the Compton edge is the channel which has half the yield of the maximum of the Compton edge. For calibration two Compton edge channels are measured C_1 and C_2 with Compton edge energies of E_{e1} and E_{e2} . Then equation 2.4 determines the MeVee/channel calibration, Cal , and equation 2.5 determines the pedestal,

ped.

$$Cal = \frac{E_{e1} - E_{e2}}{C_1 - C_2} \quad (2.4)$$

$$ped = C_1 - \frac{E_{e1}}{Cal} \quad (2.5)$$

When calibrating with a gamma-ray source it is important to note that the energy calibration is only valid for other gamma rays. For neutron-induced proton recoils the energy measured is not measured in MeV, but instead mega electron equivalent (MeVee). Electron equivalent is a measure of energy that links the integral of a signal pulse and the energy deposited by a recoiling electron. PMTs can only measure the light generated by an interaction and do not know whether the light was generated by a proton or electron. Electrons generate an amount of light proportional to their energy. This means that an MeVee is the amount of light generated by a 1 MeV electron. Proton recoils produce less light than an electron of equal energy. To go from MeVee to MeV, a proton light response function is needed.

In order to measure neutrons from 1 to 10 MeV a full energy scale range of 10 MeVee would suffice. For the gamma-ray sources ^{232}Th was chosen for its 2.6 MeV and ^{22}Na for its 1.27 MeV gamma ray. To calibrate the detectors calibration runs were taken with the Th and Na separately by placing a source at the center of a bar and collecting data for about 10 minutes. The sources were wedged between two bars allowing for the calibration of all 16 bars in 8 runs. These calibration runs were used primarily for diagnostic purposes, but also served to determine the pedestal. Calibration runs are very time consuming; a full 16 bar calibration was only done when something significant changed with the setup. Otherwise the Th sample was left approximately 2.5 m away and in line of sight of the bars at all times. This allowed the bars to collect some calibration data during the entire experiment. Since the beam has a duty factor of 5%, we collect 55 minutes of calibration data per hour of run time. Due to the Th source distance

from the bars, 5 hours of data were needed to extract a viable Compton edge for calibration.

There were over 100 hours of data collected and each hour needed a calibration. Even in 5-hour groups there were still 32 PMT channels (both tubes of a bar are calibrated independently) per group equating to over 640 energy spectra to calibrate. This would take too long by hand so a fitting program was developed to fit the Compton edges instead. The program fit a Gaussian-convoluted step function plus an exponential background to the calibration spectra. Equation 2.6 is the fit function used with A, B, C, σ , and x_{edge} as fit parameters, and x the channel number.

$$f(x) = A * \exp(-B * x) + C * \sigma * (1 - \operatorname{erf}(\frac{x - x_{edge}}{\sigma})) \quad (2.6)$$

The parameters σ and x_{edge} have some significant meanings. σ represents the channel spread of the Compton edge, i.e. the energy resolution of the detector. The channel value of the Compton edge is represented by x_{edge} . The procedure used to fit this function is to first fit the exponential background omitting the 100 channels where the Compton edge is dominant. For example, the histogram shown in figure 2.3 was fit over channels 200 to 400 to fit the background. Then, fix the background parameters in equation 2.6 and find a new fit except only over the range where the Compton edge is dominant. Finally, using the fit parameters from the previous step calculate a final calibration fit without fixing the background variables and extract x_{edge} . The χ^2 optimization routine Minuit was used and is found in the ROOT software package. Figure 2.3 shows an example spectrum with the final fit function overlaid with the data.

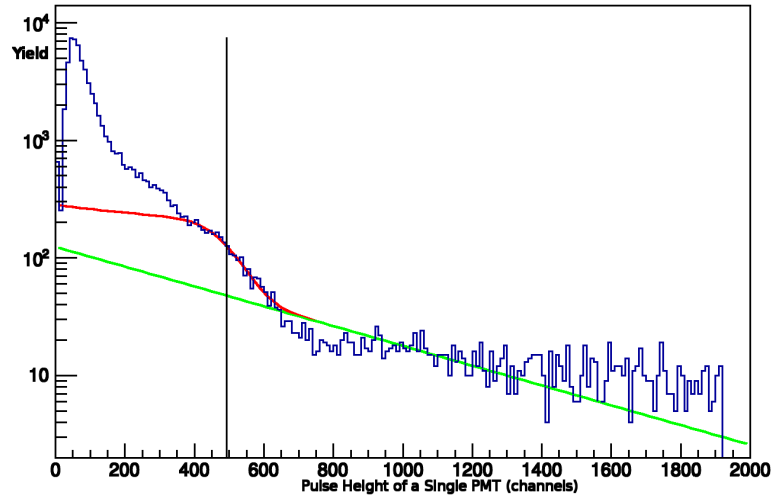


Figure 2.3: Example calibration fit. Blue histogram is Th data. Green curve is fitted exponential background while red curve is background plus fitted edge. Lastly, the black vertical line shows the x_{edge} parameter.

The Compton edge channel is tracked as a function of group number. Groups are a collection of 5 one-hour data runs. Figure 2.4 shows the evolution of the Compton edge over the entire data set for a single PMT.

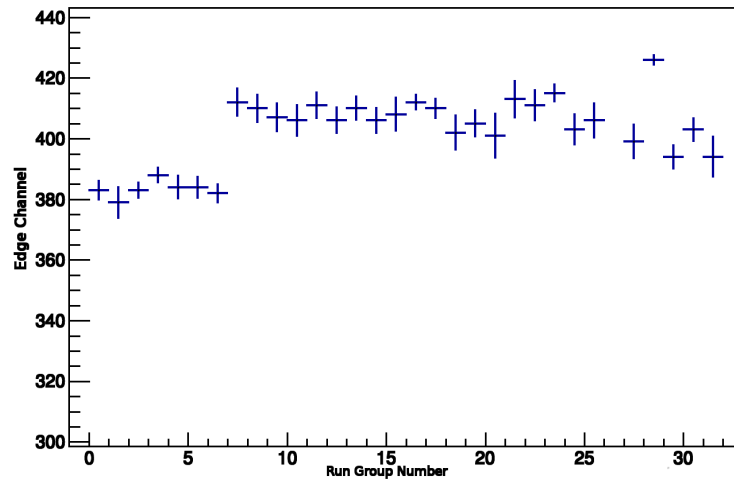


Figure 2.4: Compton edge channel number as a function of group number. Groups are 5-hour runs. At the 6th group a discrete change in the Compton edge channel occurs. This is due to a change in the pedestal that was the result of a CAMAC crate failure.

Once the pedestal and Compton edges are known for each of the 32 PMTs

and for each run, both are put into an array and used to calibrate each event. The energy $E(x)$ in MeVee of an event is calculated using the channel number x , the pedestal obtained from the calibration runs described earlier, and the energy calibration as a function of run number $C(\text{run})$. Equation 2.7 is used to go from channel number to energy in MeVee.

$$\begin{aligned}
 E(x) &= C(\text{run}) * (x - \text{ped}) \\
 C(\text{run}) &= \frac{2.38 \text{ MeVee}}{x_{\text{edge}} - \text{ped}}
 \end{aligned}
 \tag{2.7}$$

2.2.2 Time Measurement and Calibration

Time spectra are collected from detectors using a device known as a Time-to-Digital Converter (TDC). A TDC measures the time difference between two timing signals. The two timing signals are referred to as a start and a stop. Timing signals are NIM logic pulses typically created by discriminators that are connected to a detector. Leading-edge discriminators are electronic modules that convert analog signal pulses into NIM logic pulses. The discriminator creates a logic pulse the moment when the signal pulse reaches a voltage above a set threshold. Due to the finite rise time of leading edge discriminators, the timing of the logic pulse depends not only on the timing of the event, but also on its amplitude. This phenomenon is known as time walk. In order to avoid time walk and ensure good timing, Constant Fraction Discriminators (CFD) are used. The CFD timing signals are independent of the maximum signal pulse voltage and depend only on the event timing itself. A typical time measurement setup will usually involve at least two detectors, for example a fission chamber which measures when a fission event occurs, and the neutron bars which measure when a neutron is detected. The TDC start is the fission chamber timing and the TDC stop is the bar timing. This time difference is the neutron time-of-flight (TOF).

TDC calibrations require a t_0 reference time. Simultaneous with a fission event there is a release of prompt gamma rays that travel to the bars. The TOF of these

gamma rays is used as the t_0 for the bar TDCS with a PPAC trigger. Gamma flashes create a characteristic peak in a TOF spectra, as shown by the peak at 0 ns in figure 2.5. A similar gamma flash occurs when the WNR spallation target is hit by protons to generate neutrons. By subtracting the gamma flash time from each event, the resulting TDC spectrum is relative to the gamma flash time. The TOF of a gamma flash is found by dividing the length of its flight path by the speed of light. With the known TOF of the gamma flash it is then possible to determine each event's time relative to fission or spallation.

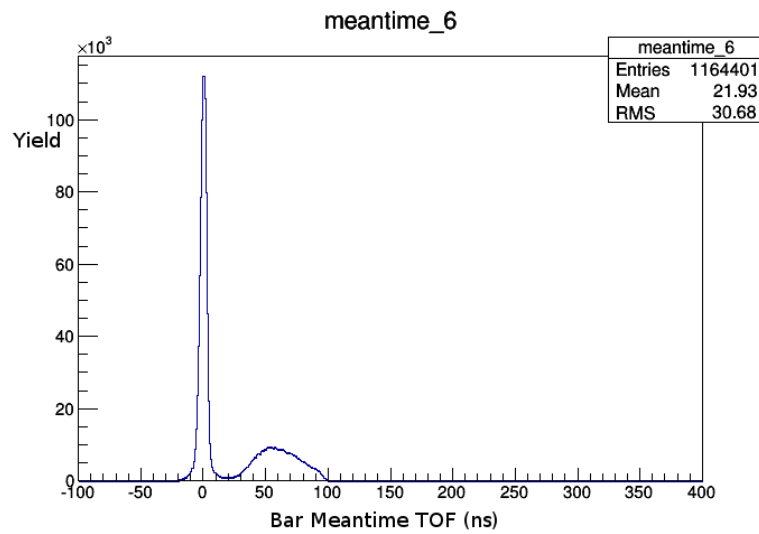


Figure 2.5: Example bar TOF spectrum with PPAC trigger cut and gamma flash at 0 nanoseconds. The width of this feature is a function of the timing resolution. In this example the gamma source is about 1.9 m from the detector. Therefore, to get the true time-of-flight add 6.3 ns to the measured TOF of each event.

The nanosecond/channel TDC calibration is done using a device known as a “time calibrator” (Ortec model 462). This device gives regular TDC start signals every R nanoseconds, where R is the range, set by the module. The range needs to set longer than the maximum time difference measured. A TDC stop follows $k \cdot T$ nanoseconds after the TDC start, with the period between possible pulses T and a random integer k between 1 and R/T . The period is always an integer multiple of T . There are R/T TDC start/stop combinations. The TDC measures the time difference between each TDC start and stop. Since the TDCs measure

time down to 0.25 ns and each start/stop time difference is of the form $k \cdot T$ with $T > 10$ ns then, these time differences are discrete peaks in the TDC spectrum. Figure 2.6 shows an example spectrum. The peaks in the spectrum are separated by T , which is 40 ns in this case.

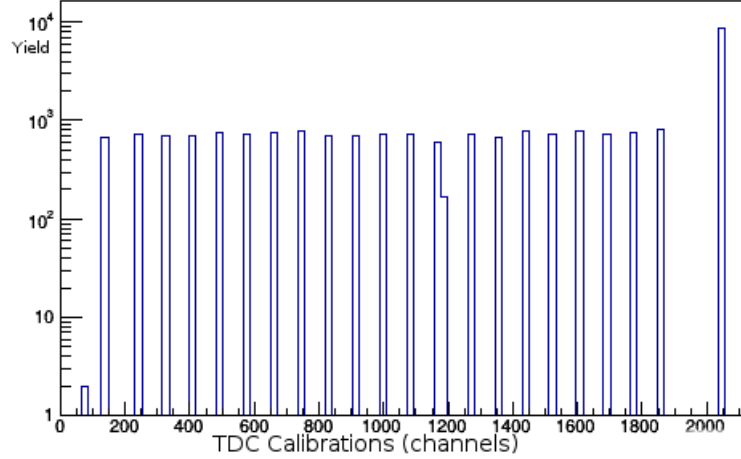


Figure 2.6: Example time calibration spectrum. The time difference between each peak is 40 ns. By measuring the channel difference between peaks the nanoseconds/channel conversion is extracted as a function of channel number.

By measuring the channel difference between peaks, the nanoseconds/channel conversion is extracted as a function of channel number. A program was written to extract the channel number of each peak. The program takes the difference between subsequent peak channels. These differences are associated with the midpoint channel number c_i between the two peaks. The list of channel differences are then then converted to nanoseconds per channel by equation 2.8.

$$T_i = \frac{40 \text{ ns}}{\text{peak}_{i+1} - \text{peak}_i} \quad (2.8)$$

From here a first-order polynomial fit is done on the list of T_i 's. The resultant first order polynomial is the first derivative of the final time calibration function. The fit function $t'(c)$ is given by equation 2.9 with the fit parameters a , b , and as a function of the channel number c .

$$t'(c) = a * c + b \quad (2.9)$$

Integrating equation 2.9 yields the conversion from channel to time $t(c)$ given by equation 2.10. Equation 2.9 has the same definitions as equation 2.9 but with an arbitrary constant t_{offset} added.

$$t(c) = \frac{a}{2} * c^2 + b * c + t_{offset} \quad (2.10)$$

It is convenient to set t_{offset} such that the gamma flash peak is at zero. The value of parameter b extracted from the spectrum in figure 2.6 is nearly 0.24 ns/ch. While a is very small, the quadratic term contributes less than 1% at even the largest time differences. This implies the TDCs are nearly linear.

2.3 Parallel Plate Avalanche Counter (PPAC)

In order to make TOF measurements of prompt fission neutrons using the neutron detecting bars, a signal needs to act as a start for the TDCs. The PPAC fills this role by measuring the time of fission. PPACs are generally made up of three parts: an anode, cathode, and a sample foil sandwiched in between. The sample foil is a thin disc of uranium electroplated onto a titanium disc 3 μm thick. The surface density of the uranium on each side of each foil is 400 $\mu\text{g}/\text{cm}^2$ [13]. Isobutane gas with a pressure of around 4 Torr then fills the space between the foil and charged plates. When fission occurs the charged fission fragments ionize the surrounding gas. The free electrons are accelerated by the electric potential created by the voltage applied to the parallel plates. These electrons then ionize more of the gas creating a Townsend avalanche[14]. The number of electrons created N_e is modeled by equation 2.11, with the number of electrons created by the initial ionization N_0 , the gap between the anode and cathode L , and the parameter λ which is a function of the gas flowing in the PPAC.

$$N_e = \frac{N_0 \lambda}{L} \exp\left(\frac{L}{\lambda}\right) \quad (2.11)$$

In order to achieve higher fission rates ten such layers were assembled in the PPAC. The ten layers are surrounded by a thin aluminum cylindrical sheath with thin plastic windows on either end. Figure 2.7 shows a rendering of the PPAC. The PPAC assembly is then placed on a stand in line with the beam. Each individual PPAC layer has its own voltage source and signal output. However, the voltages of the PPAC pre-amps are set in groups as there are only 3 pre-amps with four inputs and outputs each. By matching PPAC layers with similar gains into the same pre-amp it is possible to adjust the voltages of these pre-amps such that the output of all layers is similar. Once gain matched, the PPAC layers are put into a mixer to create a single PPAC output. It is this output that is sent to the DAQ electronics. Figure 2.8 shows the PPAC in its stand at WNR 15L beam line.

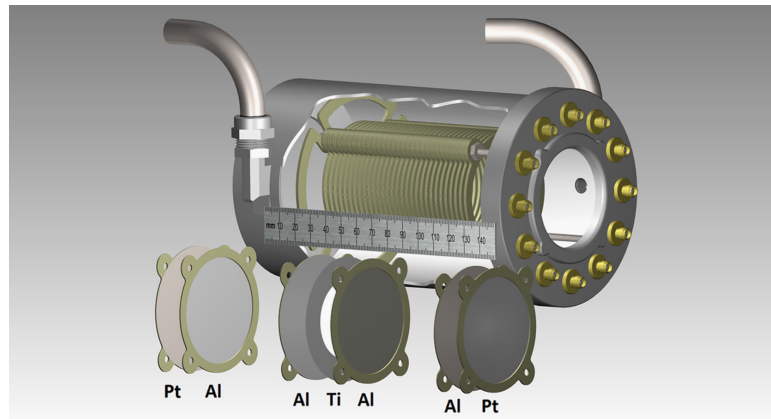


Figure 2.7: Rendering of the PPAC[13]. The Ti foil in the center has the U electroplated onto either side of the disk. The Al disks on either side form the cathode and are at ground potential. There is 3 mm between the cathodes and the Al disk anodes. Platinum disks are placed between the PPAC layers. Each disk is held by a G-10 fiberglass ring.[13]

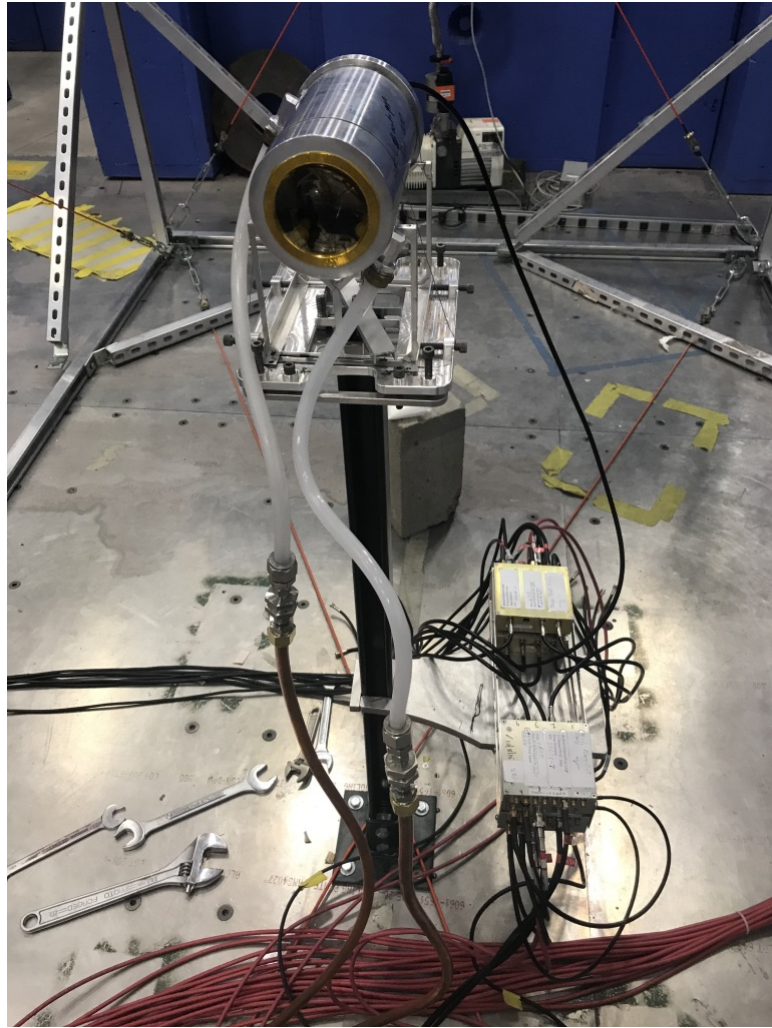


Figure 2.8: Photo of the cylindrical PPAC assembly. The white tubes carry the isobutane gas. The black cables carry the voltage and signal. This is the ^{252}Cf PPAC, which only has one active layer thus has only one cable.

Chapter 3

Experimental Setup, Measurements and Observations

In order to measure the prompt fission neutron spectrum (PFNS) of ^{235}U a neutron beam is required. The beam needs a reasonable neutron flux and a range of neutron energies between 1 and 15 MeV. At the Los Alamos Neutron Science Center (LANSCE)[15] there is an 800 MeV proton linear accelerator. Some of these protons are diverted to a tungsten spallation target. The beam protons then collide with target nuclei and eject neutrons. The spallation neutrons scatter in all directions. At WNR, a 1" beam width is produced by adding shielding to collimate the spallation neutrons. The energy of the spallation neutrons vary from a few eV to above 100 MeV. Two filters were placed near the end of the collimation. One was a 0.25" thick cylindrical piece of polyethylene and the other was a 0.25" thick cylindrical piece of lead. These filters eliminated low energy neutrons and gamma rays. The proton beam is bunched so that neutron production occurs at discrete times. These proton bunches come every $1.8 \mu\text{s}$ and are referred to as micro-pulses. However, the beam cycles between on and off every 10 ms with bundles of micro-pulses that last for $625 \mu\text{s}$. A bundle of micro-pulses is referred to as a macro-pulse. Figure 3.1 shows a sketch of the beam timing.

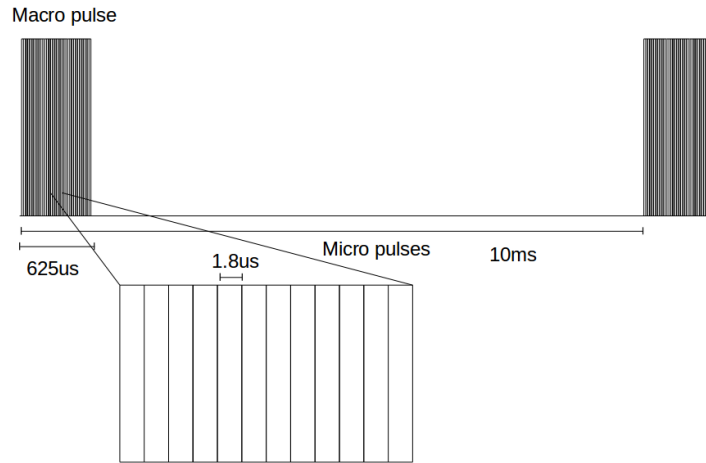


Figure 3.1: The proton beam timing. There is $1.8 \mu\text{s}$ between each micro-pulse, and each macro-pulse is $625 \mu\text{s}$ long. The macro-pulses come with a frequency of 100 Hz.

3.1 Detector Geometry at WNR 15L

The entire detector setup was positioned above and around the PPAC. The PPAC is centered 21.5 m downstream from the spallation target. Figure 3.2 is a schematic of the relative position of the PPAC and spallation target, as well as the fission chamber (FC) and beam dump. The beam dump is a large mass of concrete that captures the neutron beam, preventing the beam from going any further. The beam dump for WNR 15L is over 90 m downstream from the spallation target[15]. The fission chamber is an ionization chamber similar to the PPAC, but is primarily used to characterize the neutron beam. The fission chamber is discussed in more detail later in the section.

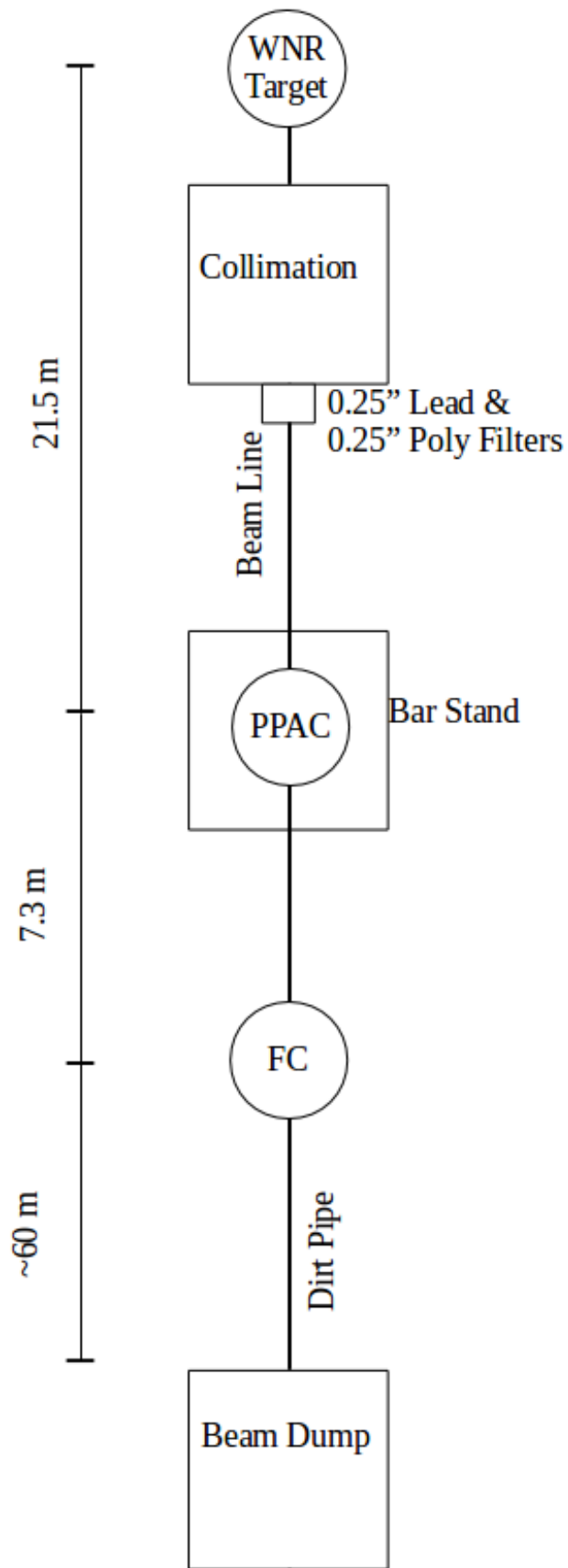


Figure 3.2: Schematic of the relative distance along the beam line of the PPAC, fission chamber (FC) and beam dump.

The PPAC was centered on the beam using lasers. The bars were held in an arc by a pair of 1/4" aluminum plates atop an aluminum unistrut stand, with each bar center approximately 1.9 m away from the PPAC. To keep track of the individual bars for analysis and diagnostic purposes the bars were numbered from 0-15 sequentially starting from the bar closest to the beam aperture. The distance from the PPAC to each bar was measured using a tape measure held at the PPAC center then extended to reach the bottom surface of each bar and centered lengthwise along the bar. The measured distances from the center of the PPAC to the center of the bottom surface of each bar are given in table 3.1.

Table 3.1: Bar center position relative to PPAC center

Bar number	Distance from Bottom Surface Bar Center to Center of PPAC (cm)
0	185
1	188
2	191
3	192
4	193
5	195
6	196
7	197
8	197
9	196
10	196
11	195
12	194
13	193
14	191
15	189

The asymmetry between the 0-7 half of the arc and the 8-15 half was due to a warped piece of unistrut that held the aluminum plates. The bar arc is 3.0 m above the ground at the center, while the PPAC is 1 m above the ground. The ground in this case is actually an aluminum plate that covers a 2 m deep pit. The aluminum plate floor is relatively thin and allows most neutrons through. When these neutrons reach the concrete at the bottom of the pit the effective solid angle of the bar array is reduced by about a factor of 3 relative to the solid

angle seen by the PPAC. Furthermore, by having to travel 3 m down then 5 m back to the detectors, the TOF of these neutrons is too long relative to the prompt fission neutrons. Neutrons that enter concrete can produce gamma rays. These gamma rays only take at most 26 ns to reach the bars from the bottom of the pit. However, it takes over 68 ns for a 10 MeV neutron to reach the bottom of the pit. The combined travel time of 94 ns is the same as a 2 MeV fission neutron would take to travel from the PPAC to the center of a bar. Since fission neutrons above 9 MeV are less than 1% as frequent as 2 MeV neutrons, this effect is tolerated. However, this experiment is most interested in fission neutron energies above 3 MeV where this effect is even less of an issue. Figure 3.3 shows a sketch of the detector setup.

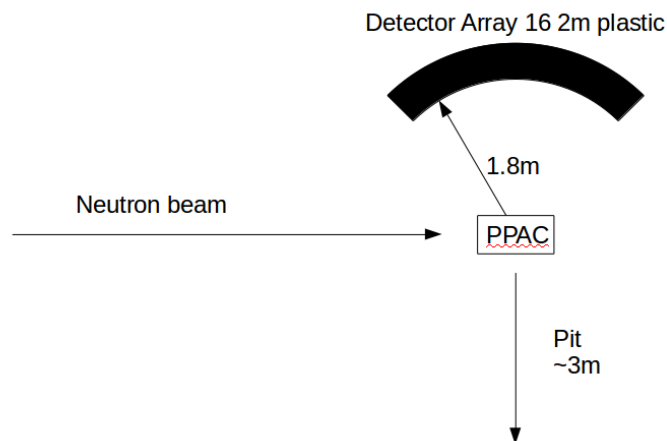


Figure 3.3: Sketch of detector geometry at WNR 15L. The neutron bars are in an arc 1.8 m from the PPAC. The PPAC stand sits above a 3 m deep concrete pit.

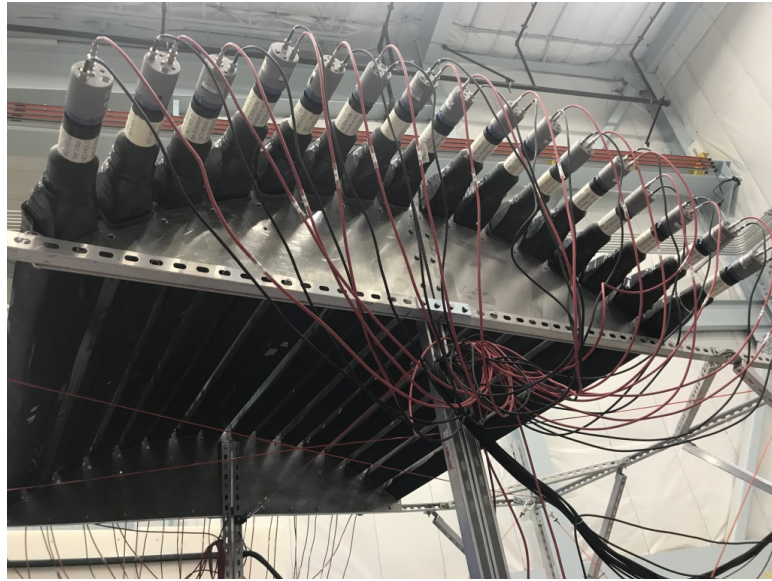


Figure 3.4: The neutron bars on the stand in WNR 15L.

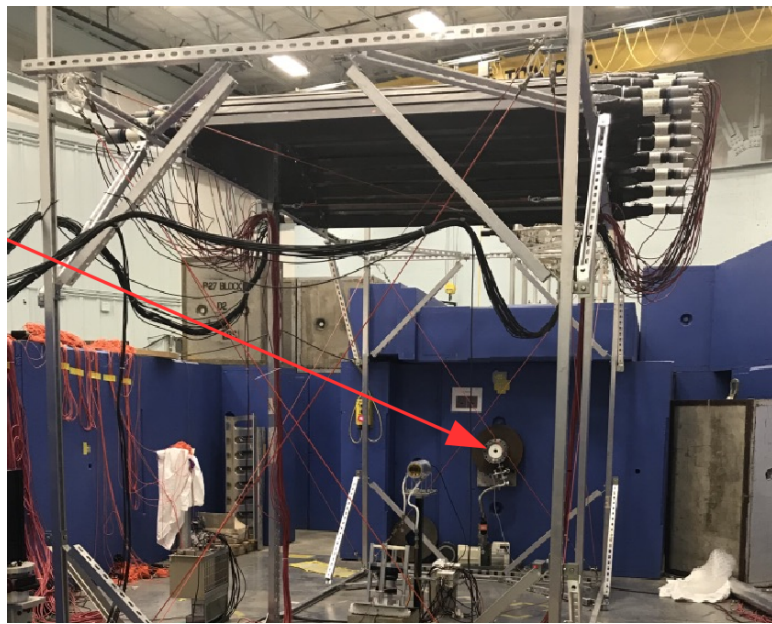


Figure 3.5: PPAC underneath the bar array with red arrow indicating where the beam emerges.

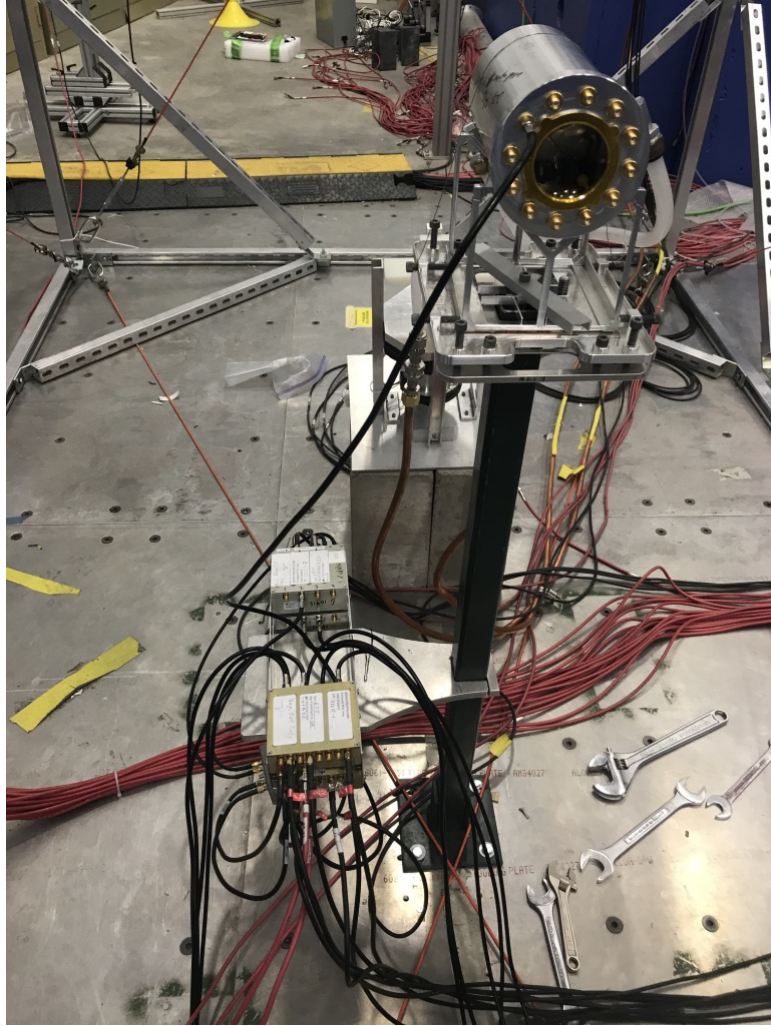


Figure 3.6: Close up of PPAC with pre-amps shown to the lower left.

With each bar at approximately the same distance to the PPAC, similar detection rates of fission neutrons are expected. A typical count rate of around 12 kHz per bar was observed during the experiment. These counts were primarily backgrounds. The count rate in the bars depends heavily on the intensity of the beam. As both the flux and occasionally the frequency of the beam would fluctuate, so too did the count rates. Several bars exhibited anomalous count rates relative to their neighbors during the experiment. Bar 0, which was closest to the beam aperture, experienced the highest count-rate nearly double the rate of bars near the center of the array. This behavior was attributed to perhaps incomplete shielding near the aperture, and bar 0 subsequently shielding the other bars. The last three bars, 13, 14, and 15, also experienced higher count rates. In particular

it was noted that, in these last three bars the PMT nearest the neighboring flight path 30L experienced a higher count rate than the PMT on the other side of the bar. The bars were nearly 1 m above the shielding blocks. It is possible that due to this lack of shielding, some scattering from nearby experiments contributed to the count rate in the detectors.

3.2 Circuits and Data Acquisition

The data acquisition system (DAQ) developed for this setup was designed to handle various triggers. A trigger is a logic pulse that causes the DAQ to write an event to disk. An event is a collection of coincident detector pulse height and timing data, which is attributed to a physical event such as a fission or cosmic ray event. The trigger types the DAQ was designed for include PPAC, PreBar, PrePPAC, and Fission Chamber(FC) triggers. A PPAC trigger records fission events in the PPAC and prompt fission neutrons when they are detected in the bars. The PreBar trigger records singles triggers in each bar during periods of beam on and calibration data while the beam is off. The PrePPAC trigger records the singles events in the PPAC. The FC trigger is used to measure the accidental bar coincidence background.

The DAQ was made up of two main parts; the analog circuit which quickly analyzed raw signals from detectors using NIM modules, and the data acquisition part which took the analyzed signals and recorded them as integers using ADCs and TDCs. Analog-to-Digital Converters (ADCs) convert integrated signal pulse height into an integer number. Time-to-Digital Converters (TDCs) are used to record the time difference between a start signal and a stop signal, and then store that difference as an integer. The ADCs and TDCs pass data into a control module that passes the data onto a laptop where it is written into an ASCII file.

3.2.1 Circuit Diagrams and Discussion

The bar circuit was designed to collect pulse height and timing data. There were sixteen bars thus the circuit for one bar was repeated sixteen times. The diagram for the bar circuit is shown in figure 3.7. The labels “Bar A” and “Bar B” indicate the raw signals from the PMTs at either end of a single neutron bar. The raw signals were split into two signals by a $50\ \Omega$ passive splitter. A passive splitter was chosen to avoid saturation, which occurs above 2 V in the LeCroy 428 fan-in/out active splitter.

One output of the splitter goes on to form an energy branch. The purpose of this branch of the circuit is to carry the PMT anode signal, through a linear gate, and to a FERA (ADC) channel. The raw signal from the splitter output is delayed by 50 ns before becoming the signal input for a Phillips 7145 linear gate. The linear gate output signal has the same pulse height as the input provided a gate signal is active in the gate input of the module. However, during periods when there is no gate signal the pulse height of the output signal is zero V. The effect of this is only the piece of the input signal that is within the time period the gate is active is output. This process is referred to as gating and the length of the logic pulse is referred to as the gate width. Gating the bar signals increases energy resolution because the pulse height goes from its peak voltage to less than 10% in 50 ns. Thus, by setting a gate of 50 ns the majority of the pulse height information is captured without admitting additional noise. Figure 3.8 shows a sketch of the relative timing of the raw signal and NIM logic.

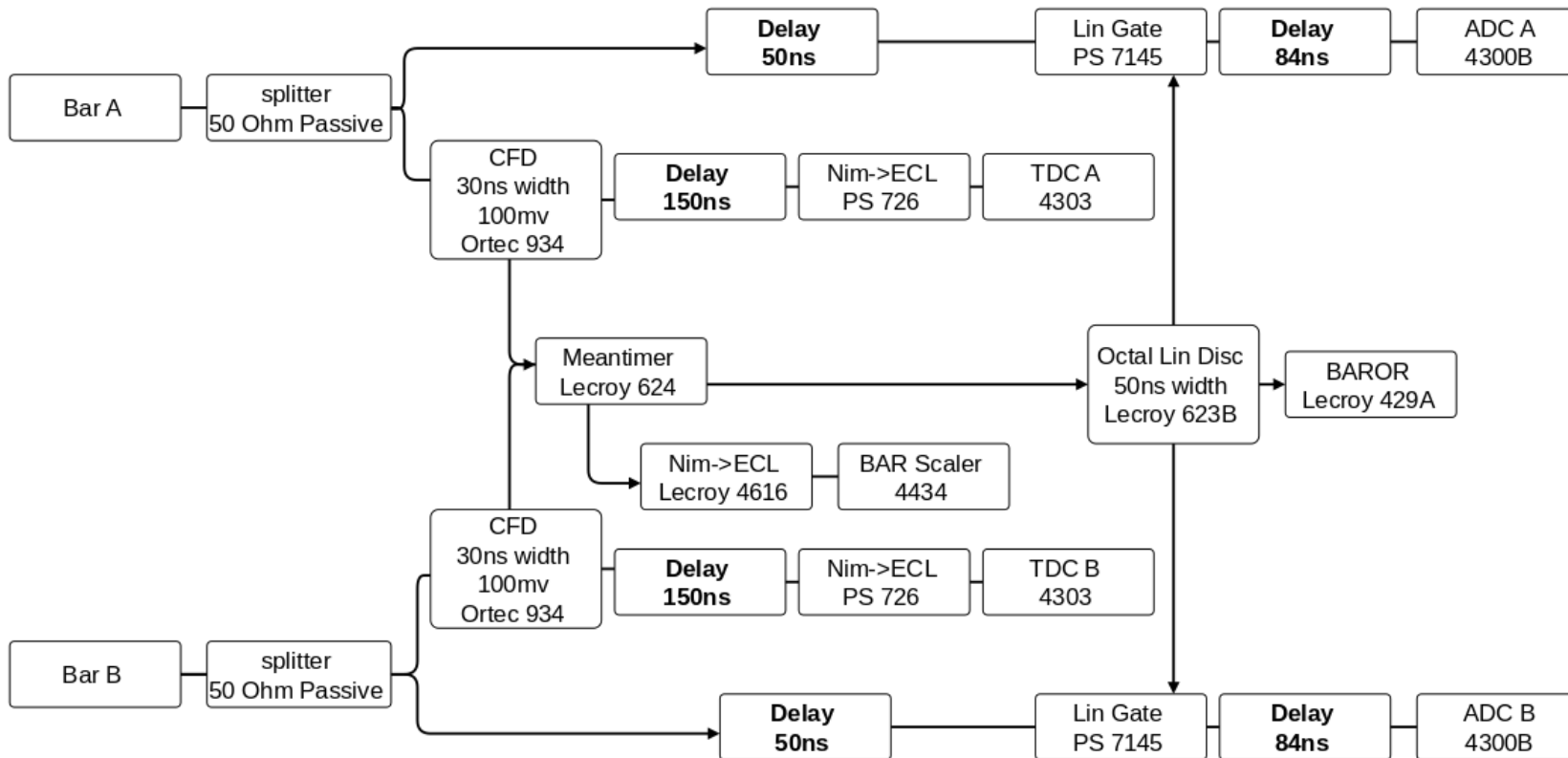


Figure 3.7: Circuit diagram for a single bar. Arrows are used to indicate signal inputs.

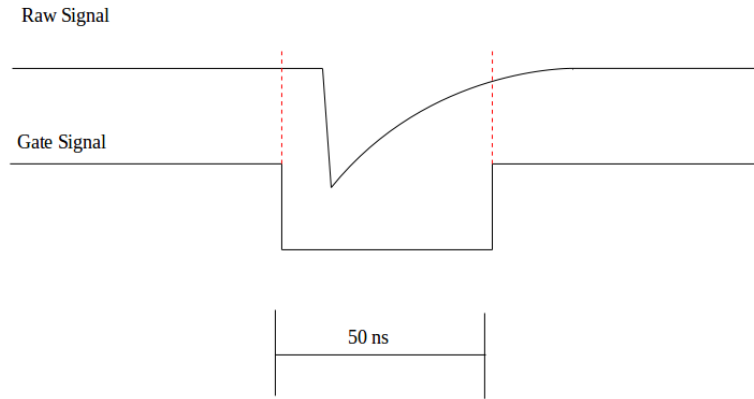


Figure 3.8: A sketch of linear gate timing of gate and raw signals. Only the signal between the red dashed lines becomes the output of the linear gate.

The output from the linear gate is then further delayed by 84 ns before it is plugged into a patch panel. From the patch panel a ribbon cable carries 16 signals to a LeCroy 4300B FERA ADC. If the signal arrives in coincidence with a FERA gate (described in the DAQ section) then the ADC will convert the signal into a number and read by the control module.

The other branch from the passive splitter forms a timing branch where the timing logic and data are analyzed. The splitter output is connected to an Ortec 934 CFD which creates the NIM logic pulses used to measure the timing of an event. The CFD creates NIM logic pulses with timing relative to the raw signal input. The CFD's timing is independent of the amplitude of the input pulse. A threshold of 100 mV was set in each CFD to start, and was later adjusted to ensure similar count rates in each detector. The CFD signal was then delayed by 150 ns before it was input into a NIM to ECL converter. From this converter, a ribbon cable carried 16 signals to the stop input on a LeCroy 4303 TFC module. The TFC module outputs a square pulse when it receives a start signal from the trigger logic. The length of this square pulse is equal to the time difference between the start and the stop signals. The amplitude of this pulse was adjusted so that a start signal without a stop signal will overflow, but stops received just before the closure of the FERA gate will not. Doing this adjustment gives the smallest ns/ch possible for a given FERA gate width.

Another CFD output was input into a LeCroy 624 mean-timer module. This module actually takes two separate CFD outputs as inputs—one from each end of a bar. The output of the mean-timer is a NIM logic pulse with a timing relative to the mean-time of the two input pulses. So in effect the mean-timer outputs a pulse with timing relative to the mean-time of the bar as opposed to timing relative to each tube separately. One output of the mean-timer is sent to a LeCroy 4434 scaler module to collect total count data. The other output is sent to a LeCroy 623B octal discriminator where it was regenerated with a signal width of 50 ns. This is done because the mean-timer does not generate logic pulses with widths needed for gating the linear gates. Two of the octal discriminator's outputs are sent to the gate input of the A and B side linear gates, while the third output is used for trigger logic and is input into a LeCroy 429A NIM logic fan in/out the outputs of this logic fan are referred to as the BAR-OR. Figure 3.9 is a circuit diagram for the BAR-OR. One logic output goes to the Blank OR which is used for the fast clear circuit described in a later section. The other two outputs are input into pre-scalers with pre scale factors of 800 and 400 for beam on/off respectively. An output from each pre-scaler is sent to a logic fan and OR'd together, then the output is delayed by 222 ns and sent to a TDC to form the PreBar trigger tag TDC channel. An output from each pre-scaler is also sent to the Trigger OR circuit for processing.

The FERA fast clear circuit is used in place of more complicated coincidence trigger logic. The central idea of the fast clear circuit is to trigger the FERA gate on every possible event, but then clear the ADCs and TDCs if there is not at least one bar coincidence or pre-scale trigger. Pre-scale triggers are allowed past the fast clear because it is their purpose to measure singles events. This in effect forms a coincidence between the triggers which clear the DAQ and the detectors which prevent the clearing. There are two inputs into the fast clear the Clear OR and the Blank OR.

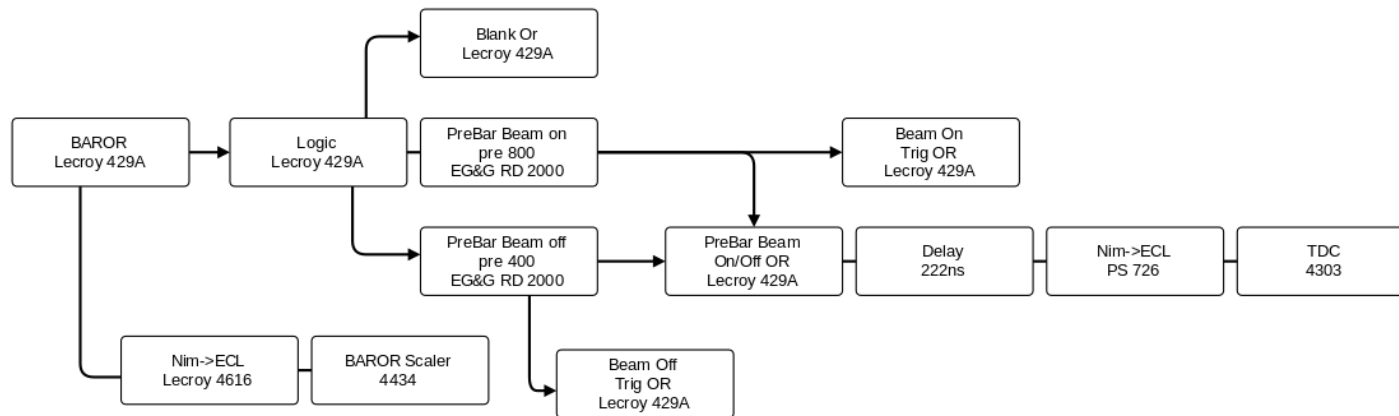


Figure 3.9: BAR-OR circuit diagram.

The Clear OR is an OR of all trigger signals used to trigger the DAQ. The Clear OR signal is input into a gate generator. The gate generator outputs a gate that is 600 ns long and is then input into the CMC clear which clears and resets the DAQ in 2 μ s. The CMC is the FERA memory and control module. The Blank OR is an OR of all sixteen bars, PrePPAC and PreBar. The pre-scaled triggers are also sent to this OR so that the pre-scaled triggers can make it past the fast clear. The Blank OR is input into a gate generator which then generates an 800 ns long gate pulse which is a square pulse similar to a NIM logic pulse. This gate is then input into the blank input on the gate generator meant for the Clear OR signal. If the Clear OR arrives at the gate generator in coincidence with the blank signal then the gate generator will output no signal. If the Clear OR's gate generator outputs no signal then the DAQ will not receive a clear signal and the event data are read out and stored on disk. This process takes approximately 15 μ s. It is important that the 800 ns long Blank OR and the Clear OR are in coincidence for desirable events. To ensure this, the 800 ns gate and Clear OR signals are viewed on an oscilloscope and delays are added to the Clear OR such that the Clear OR signal is coming in 400 ns after the beginning of the 800 ns gate. This is done because PPAC signals generate the Clear ORs, and in most cases it is the bars that generate the Blank OR. To accommodate a 400 ns range for the TDCs there was at least 400 ns of tolerance in the fast clear, allowing for signals that were up to 400 ns too early or too late. The fast clear circuit diagram is shown in figure 3.10. The PPAC OR circuit is used to measure PPAC event timing and use pulse height to distinguish alpha particles from fission fragments. Due to the low count rate of each individual layer, all ten PPAC pulse height output signals were input into a mixer to OR the signals together forming the PPAC OR. A NIM bin containing the mixer was left inside the experimental area about 2 m from the PPAC. A long cable then carried the mixer output to a linear fan in/out. One output of the linear fan takes the signal to a linear gate with a similar setup to the bar circuit. The linear gate output is sent to an ADC channel. This ADC

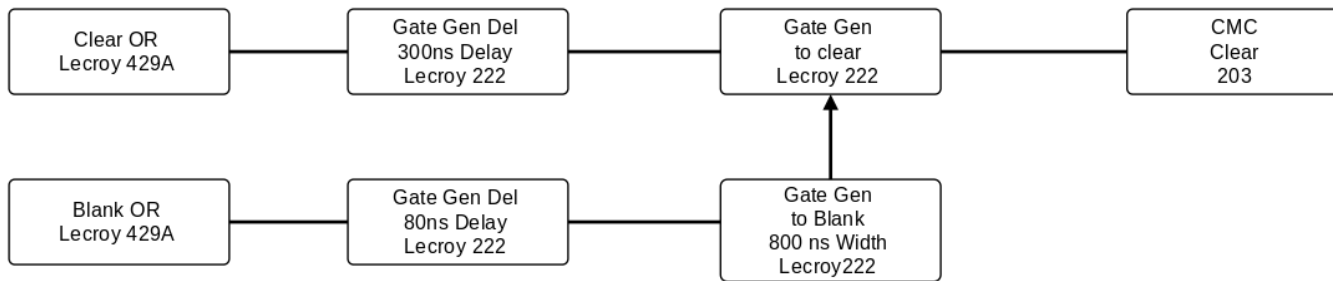


Figure 3.10: Fast clear circuit diagram.

channel is used to distinguish alpha particles from fission fragments. The other output from the PPAC OR linear fan goes to a timing filter amplifier. This module is used to shape the pulse in order to achieve better timing resolution. A CFD is used to generate the NIM logic pulses that are then carried to a PPAC logic circuit and a TDC to generate PPAC timing data. The PPAC logic branch has outputs to the Beam-ON trigger, the Clear OR and a scaler. The logic branch also outputs to a pre-scaler set at a pre-scale factor of 50. This pre-scaled signal is used to generate PPAC pre-scale events which are vital for accidental background estimations. The trigger logic circuit handles triggering the DAQ. A trigger is any event that causes the DAQ to begin the process of collecting data from ADCs and TDCs. All triggers are collected into two separate logic modules, one for the Beam-ON triggers and one for Beam-OFF. The Beam-ON/OFF ORs, as their names suggest, are collections of triggers meant for when the beam is on or off. The Beam-ON OR is in coincidence with a $640 \mu\text{s}$ gate that is generated by the first t_0 of the macro-pulse. The t_0 is sent when the protons from the accelerator reach the spallation target. The Beam-OFF OR is similarly in coincidence with a 9 ms gate which comes 1 ms after the t_0 . Each of these triggers are sent to TDCs and both are used as trigger flags for later off-line analysis. Both the Beam-ON and Beam-OFF triggers are vetoed by the CMC veto. The CMC veto signal is a logic pulse send by the CMC when it is busy. The two Beam-ON/OFF triggers are ORd together to form a final master trigger. The master trigger is used to generate the signal start of the TFC modules. The master trigger also forms a 500 ns gate, the “FERA gate” which is sent to the CMC to start the DAQ. The beam t_0 is a timing signal sent when a proton pulse reaches the spallation target and creates neutrons. Thus the t_0 signal is important for analyzing the neutron beam energy. It is needed for background estimations as the accidental background rate is proportional to the neutron flux, which is a function of time relative to t_0 . The t_0 /Vramp circuit is designed to record the t_0 timing as well as to estimate when an event takes place during the $625 \mu\text{s}$ macro-pulse. To record

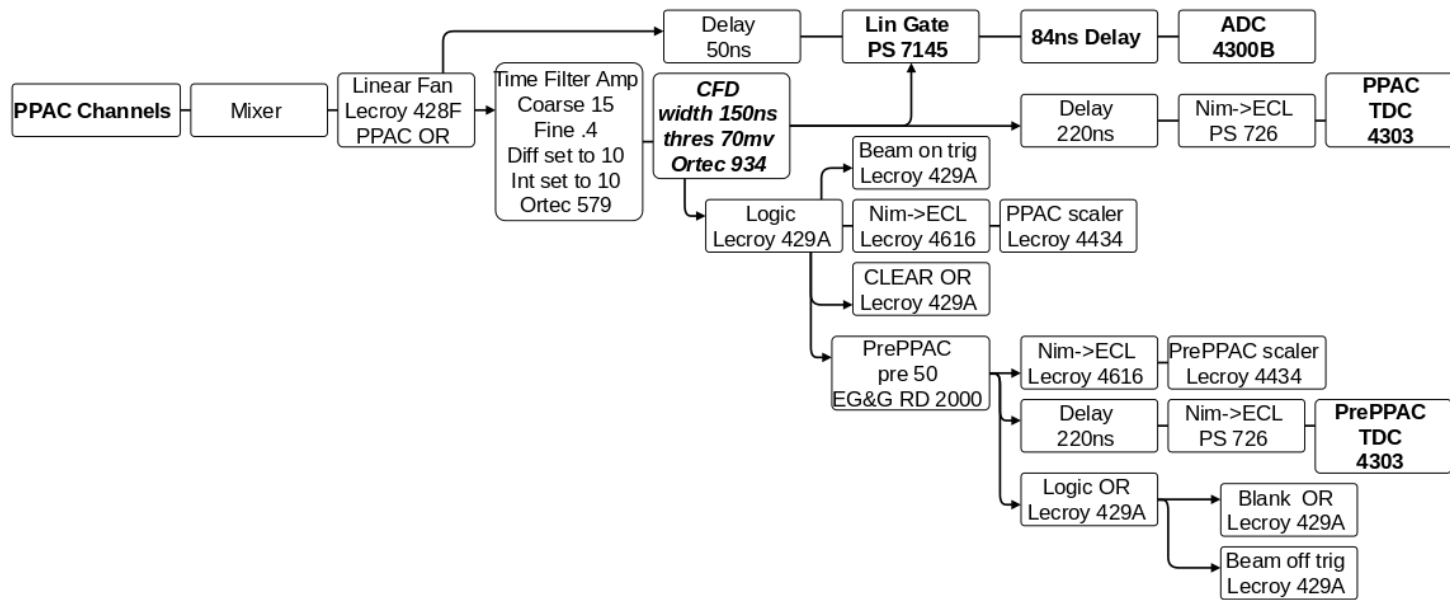


Figure 3.11: PPAC OR circuit diagram.

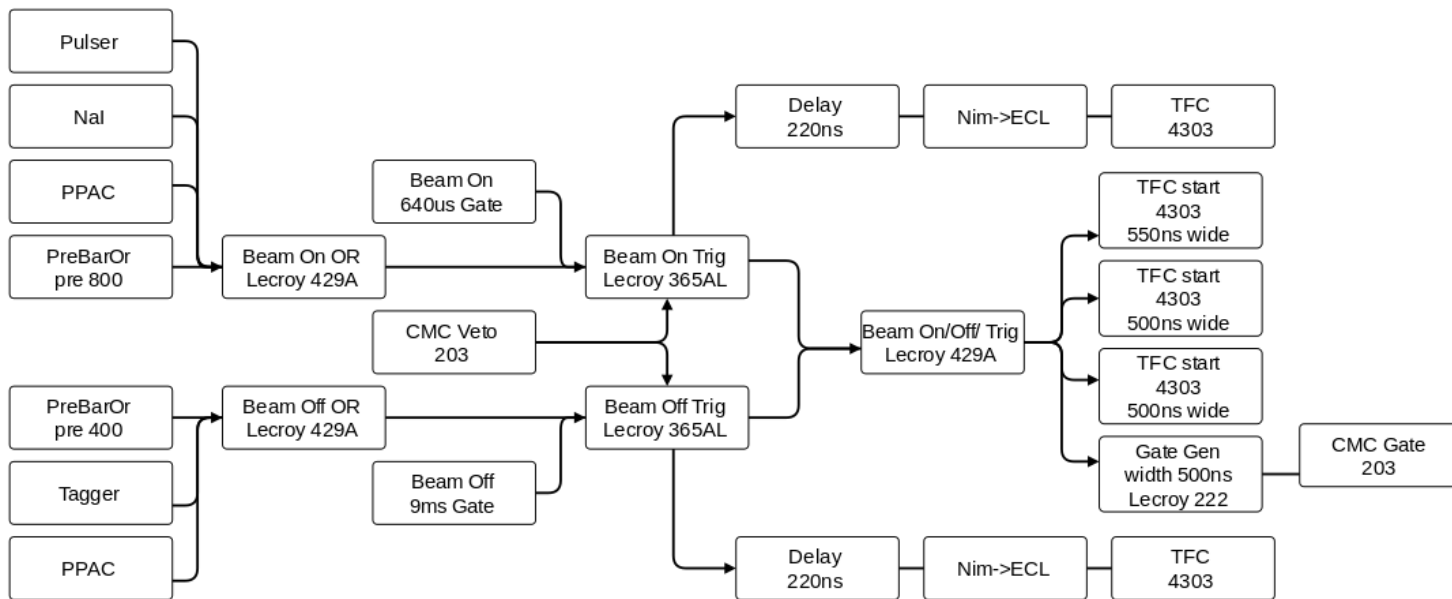


Figure 3.12: Trigger circuit

the timing of the t_0 , several copies of the pulse are made, each with a different amount of signal delay. The reason for the copies and delay is the TDCs can only measure time differences up to 500 ns. Since each micro-pulse is 1800 ns long, more than one TDC channel is needed. By delaying each copy by an increasing amount, when an event does occur the t_0 is recorded on scale in at least one TDC. By knowing the amount of delay between each TDC, and analyzing the overlap between each TDC, it is possible to stitch them together to form a full 1.8 μs t_0 time-of-flight histogram. The first copy of t_0 goes straight into a TDC, while the next copy is delayed by 370 ns. Then, each copy of t_0 is delayed by 370 ns relative to the previous copy. To do this, t_0 is input into a logic fan and two copies are made. Then one is sent to a TDC and the other to a 370 ns delay box. From the delay box the delayed t_0 signal is sent to another logic fan and repeats the splitting to TDC and delay process. This routine is repeated enough times to ensure the entire 1.8 μs micro-pulse is covered. Figure 3.13 is one link in the t_0 copy chain. A voltage ramp module (Vramp) is used to measure the time relative to the start of the macro-pulse. It does this by beginning the linear voltage ramp when it receives the t_0 as a start signal. The output of the Vramp is sent to a linear gate, gated by a 50 ns wide gate started by the Beam-ON trigger. Since the voltage ramp is linear, whenever an event takes place the integrated charge is unique to that particular time relative to t_0 . To this end the Vramp has a calibration mode. In calibration mode the Vramp will go to 0 V for 5 μs every 45 μs . These breaks are used to create a time-to-charge calibration for the Vramp ADC spectrum. The proton beam is bunched into macro-pulses with a frequency of 120 Hz. The WNR target receives 100 Hz and the remaining 20 Hz of the beam is diverted elsewhere. However, when the 20 Hz beam is not diverted, WNR received the entire 120 Hz. The method used to estimate accidental backgrounds requires knowledge of the beam frequency. To this end a 1 kHz pulser with a Beam-ON coincidence requirement was installed. If there is a change in the beam frequency, the number of pulses measured per hour also changes accordingly. An

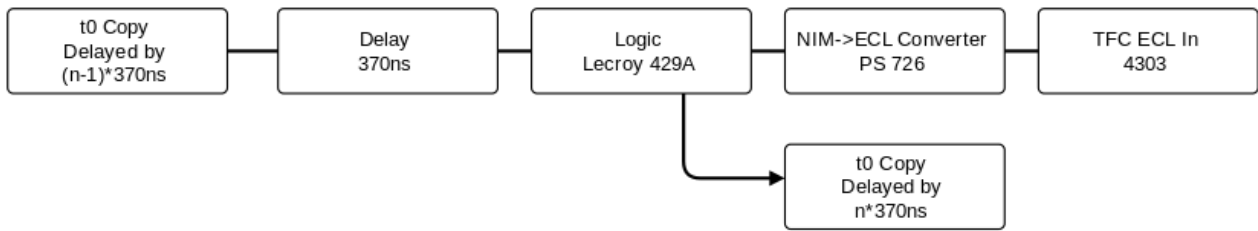


Figure 3.13: t0 copy circuit diagram

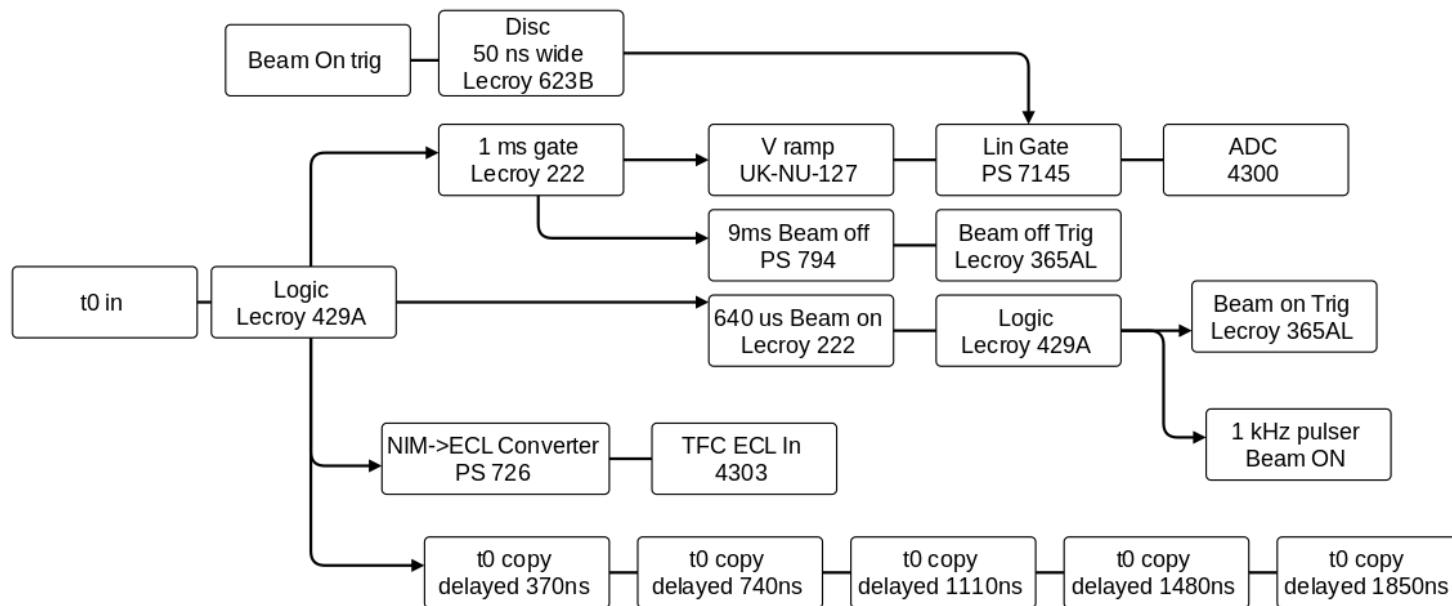


Figure 3.14: t0/Vramp circuit diagram. Each element of t0 copy outputs to a TDC but delayed by the specified amount.

issue with this method is the fact that the beam regularly shuts down for short periods of time. If the beam goes off during a run the frequency measured using the pulser will not match up with the actual beam frequency. A potential method to get around this issue which was not implemented is to set up a 1 Hz pulser with a simple beam online requirement to keep track of the beam uptime during a run. For this data run however, runs were simply excluded from the analysis if there was significant beam downtime. As determined by a beam-down cut which combined run start time and beam current data. The start time of data run files was found in a header line at the start of each file. The beam current log file provided by LANL contained the beam current averaged over one minute bins for the entire run cycle. A run was determined to have significant beam-down time if more than 5 minutes of the run had a beam current of $0 \mu\text{A}$. However, most runs that did not satisfy this cut, failed because the beam was down for the entire run due to maintenance.

The 1 kHz pulser is also useful for determining dead-time. To do this, two copies of the pulser signal with a Beam-ON coincidence requirement are created. One copy is sent to a scaler directly. This scaler is referred to as the real-time scaler. The other is sent to a coincidence module with the CMC veto signal input into the module's veto input. If a logic signal is received into the veto input then the output of the coincidence module is suppressed. This combination in effect creates a pulser that only counts during Beam-ON DAQ live-time. By plugging this signal into a scaler a live-time scaler is created. The difference between the real-time and live-time scalers is proportional to the dead-time. Since there is a Beam-ON requirement, this dead-time measurement is an estimate of the dead time during Beam-ON micro-pulses. A second fission chamber (FC), which was eluded to in a previous section, was also used in this experiment. Data from FC were primarily used to measure the accidental backgrounds. This FC was 727 cm downstream from the PPAC. This long distance meant that any coincidence between the bars and the fission chamber was accidental. Another nice quality

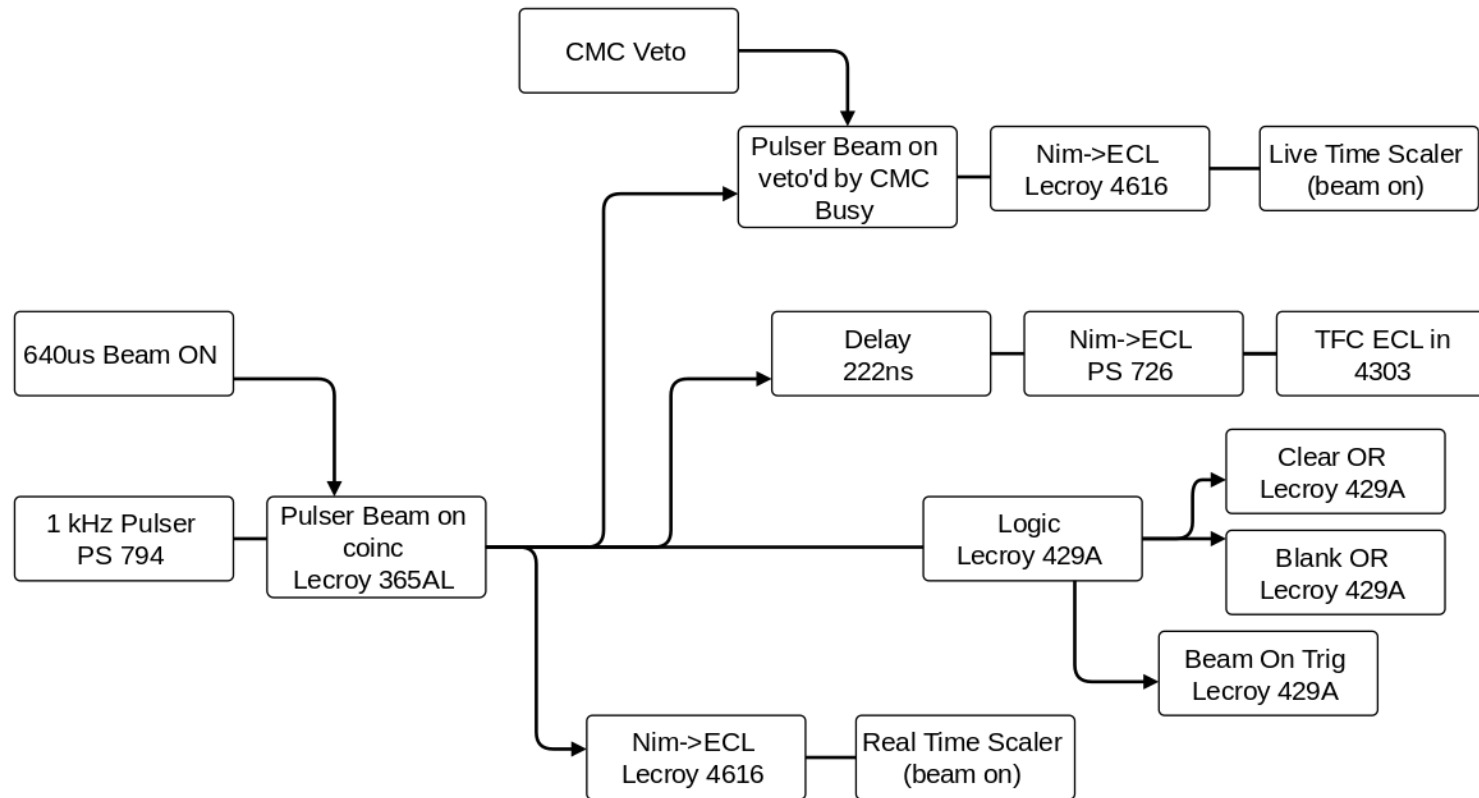


Figure 3.15: Pulsar circuit diagram

of the fission chamber is its count rate is proportional to the beam intensity. This means that the measured accidental rate from the fission chamber and the estimated rate from the analysis should agree. The circuit used to collect fission chamber data was similar to the neutron bars, albeit much simpler. The fission chamber's raw signal is split, and then sent to a linear gate which is self gated by a CFD. The linear gate output is then sent to an ADC. This ADC channel is used to separate alphas from fission fragments, similar to the PPAC. The CFD outputs are sent to a TDC, scaler, and two trigger logic inputs. The fission chamber is part of the Beam-ON trigger, as well as a Blank-OR for stopping the fast clear and ensuring the event is written to disk. This is important due to the lower count rate of the fission chamber.

3.2.2 Data Acquisition Details

The DAQ for this experiment needed to have low dead-time. The LeCroy Fast Encoding and Readout ADC (FERA) was chosen for its low dead-time of just 15 μs per event. Adding additional FERA modules does not increase this dead-time. Each ADC has 16 channels. To create a FERA-based TDC, the Fast Encoding Time-to-Charge Converter (TFC) is used. The TFC takes 16 channels of ECL logic inputs which it interprets as a stop signal for each channel. The 16 channels are all started by the same signal which is also an ECL input. The TFC outputs an ECL logic pulse along a ribbon cable to a FERA ADC. The logic pulse has a width determined by the time difference between the start and stop signals. The height of the logic output was manually adjusted to achieve the desired time resolution. This combination of TFC and ADC is referred to as a TDC for this DAQ. The FERA modules are controlled by a CMC 203 FERA controller. This module coordinated the ADCs by passing along a FERA gate which the ADCs used as a start to begin integrating charge. The CMC also acted as a memory module, holding up to 2 MB of data. When the module's memory reaches half full or when a specified amount of time has passed, it sends the data to the CAMAC

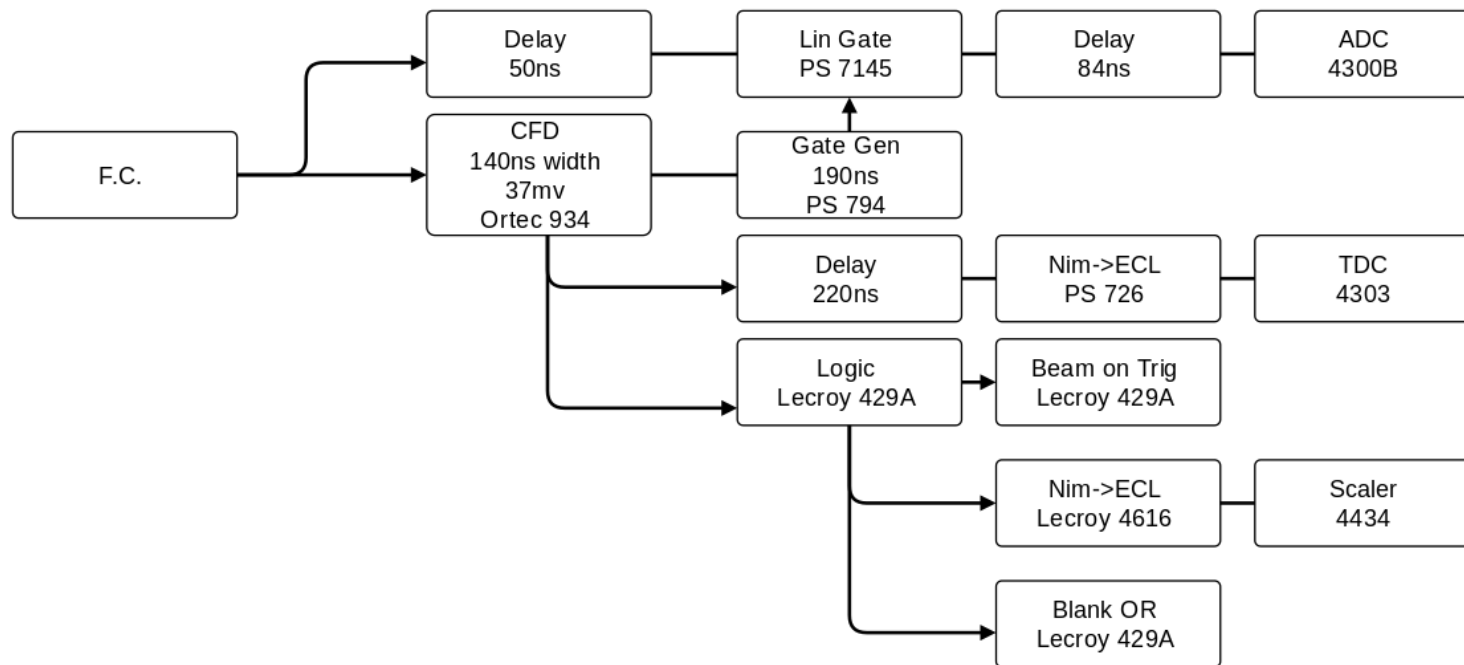


Figure 3.16: Fission chamber circuit diagram

crate controller. From there the data are sent to the DAQ laptop via a USB cable where they are written to disk.

The FERA gate is a logic pulse with a width equal to the width of the input NIM logic pulse. For this experiment the FERA gate was 500 ns long. The FERA gate is passed along a serial bus to each LeCroy 4300B FERA ADC gate input. While the FERA gate is open each ADC integrates the voltage input of each channel. After the ADCs are done integrating, the data are read out along a ribbon cable to the CMC controller.

The software used to control the DAQ was Kmax. Kmax is a java-based DAQ control software. The Kmax tool-sheets, which are a combination of on-screen buttons and histograms and java code, are highly customizable. Once a tool-sheet is compiled its buttons become active and the DAQ can be initialized. After initializing the FERA modules the software then only communicate with the CAMAC controller when the CAMAC controller is ready to send data. The data transfer between the Kmax software and the CAMAC controller is slow compared with the dead-time of the FERA modules. Due to this slow connection, data readouts were as infrequent as possible. If the event rate exceeds a certain threshold then the Kmax software will crash as it cannot handle the excess data. Event rates which lead to crashes depend on the number of ADCs in use. For this experiment six ADCs were used and an event rate exceeding 2500 events/sec would lead to a crash. If a crash does occur the data is saved to an ASCII file. Further, the Kmax software is set up to use a timer to automatically create a new data file periodically after a set amount of time has passed. A typical run time is one hour for each data file. Kmax also updates online histograms whenever data are read out. These histograms are useful for diagnostic purposes.

Chapter 4

Data Analysis

4.1 Analysis Summary

The goal of the data analysis is to give meaning to the raw data, by interpreting it in the physical context of the experiment. Every hour the DAQ closes an ASCII file containing all the data collected over that hour. These files are referred to as “run files” or “runs”. The run files were organized into rows and columns. The rows had 128 elements separated into columns, and each element in a row are considered to be coincident with each other. Each column corresponded to a particular TDC or ADC channel and went in order from 0 to 79 for the ADCs and 0 to 47 for the TDCs. The ADCs and TDCs were distinguished by the fact that the ADC channels were listed first in every row. The run files were then sorted using ROOT. The sorting involved first filling a ROOT tree file. The advantage of a ROOT tree file is the coincidence structure of the data is maintained. This allows for analysis of the tree file instead of the original run file. The tree files were then analyzed by a C++ based algorithm that performed calculations and filled histograms on an event-by-event basis. Events in this context are the data on a single row of the original ASCII file. TDC channels each spanned a range of 500 ns, while ADC ranges depended on each ADC’s unique calibration. Each detector and bar PMT was assigned to a unique ADC and TDC channel, with the exception of the beam pick-off as it needed four TDC channels to span its full 1800 ns range.

The DAQ triggers were each assigned a TDC channel. These channels had a

unique feature known as a self timing peak which is a very narrow peak caused by the trigger starting and stopping its own TDC. The time difference between the start and stop is non-zero due to a signal delay but the time difference is a constant, which leads to the narrow peak. When a self-timing peak is present in the TDC channel of a trigger, that trigger started the DAQ. The trigger sets the start time for all TDCs. Therefore, it is essential to know which trigger started the DAQ as all TDC data taken for an event are measured relative to that triggers timing.

After the trigger of an event is determined the data cuts are applied. Data cuts are any logical requirement that an event must fulfill to be included in a histogram or analytical calculation. Trigger cuts are an element of every TOF histogram since the zero time of the TDC is determined by the trigger. Energy threshold cuts are a test if the measured energy deposition is above a set value or not. These cuts are required in bar TOF histograms and the energy via TOF (ETOF) histogram. After cuts are applied calculations are made. A few of the important calculations are: the neutron flight path (FP), ETOF, and the mean energy deposition. The neutron flight path is determined by a combination of the measured perpendicular distance from the PPAC to the center of the bar, and the measured distance from the center of the bar to where the event took place. The distance from bar center is obtained from the measured difference in the time it took the light generated by the event to reach each PMT. The ETOF is calculated using the FP result and the measured mean bar TOF. The mean TOF of a neutron is measured using the average of the TOFs measured by the PMTs on either end of the bar. The mean energy deposition is calculated by taking the geometric mean of the two energy-calibrated ADCs of a bar. The mean energy is useful for threshold cuts because it is independent of where along the bar the event took place. Beam energy cuts are applied only allowing events with beam TOF (t_f) values between t_1 and t_2 . The times t_1 and t_2 are the TOF of the low energy and high energy beam neutron cutoffs. The beam energy cuts are 1 to 5 MeV, and 5 to 10 MeV.

After the calculations are done the histograms are filled.

Finally, the accidental backgrounds are calculated using the PreBar and PrePPAC singles data. The accidental backgrounds are a function of fission time (t_f) and neutron time (t_n). These times are relative to the beam time t_0 . So t_f is the beam neutron TOF to reach the PPAC and t_n is the sum of t_f and the TOF from the PPAC to the bar t_m . The singles count rates per micro-pulse for the PPAC and bars were estimated by averaging them over an hour. This was done by measuring t_f and t_n and filling TOF histograms for each run, then dividing each 1 ns bin by the number of micro-pulses per hour N . Since N varied for some runs, a method was created to establish which hours had a large change in N and these runs were omitted from the analysis. The omission of runs was done because the accidental background estimation relies on a valid calculation of instantaneous rates, and the average is only valid if the rates stayed nearly constant through the hour. The singles fission and bar rates are the probability of detecting a fission or bar event per micro-pulse. Thus the product of these probabilities is the probability of an accidental coincidence. Once the average rates were calculated they were multiplied to form the accidental coincidence rate. The accidental coincidence rate is then multiplied by the number of micro-pulses to give the number of accidental coincidences per hour, $A(t_n, t_f)$, for each combination of t_n and t_f . The difference between t_n and t_f is t_m , which is the mean TOF of a fission neutron. An accidental TOF spectrum $A(t_m)$ is formed by creating 1 ns wide bins for each value of t_m between -100 ns and 400 ns. The times are relative to the fission gamma flash so negative times are accidental background bar events that occur before a fission event. Then, each bin is filled with the sum of every $A(t_n, t_f)$ that has a combination of t_n and t_f that satisfy $t_n - t_f = t_m$. The accidental TOF spectrum is then transformed into an ETOF spectrum $A(E)$ with energy via TOF E . The net PFNS is then the bin-by-bin difference of the ETOF spectrum and $A(E)$.

4.2 DAQ Triggers

A DAQ trigger is a logic pulse that acts as the TDC start and begins the process that culminates in writing the ADC and TDC values to disk. There are four triggers used in this experiment; PPAC, PrePPAC, PreBar, and FC. These triggers are useful for collecting different kinds of data. The types of data they collect depends on the zero time they set as well as when during the Beam-ON/OFF cycle the trigger is active. The PPAC trigger is triggered by a coincidence of a bar and the PPAC both exceeding their CFD thresholds. The PPAC trigger collects PPAC pulse height, beam neutron TOF to PPAC, bar pulse height, and bar TOF relative to fission. These data are used to ultimately generate an ETOF histogram for fission neutrons. The PrePPAC and PreBar are pre-scaled triggers. This means that they only trigger the DAQ on every PS triggers where PS is the pre-scale factor. The PrePPAC trigger is a singles trigger that is triggered by the pulse height of the PPAC exceeding its CFD threshold and it is the 1 in 50 triggers the pre-scale module lets through. The PrePPAC trigger collects PPAC pulse height and beam neutron TOF to PPAC data. These data are used for the accidental background calculation. The PreBar is triggered by any bar exceeding its CFD threshold and it is the 400th trigger since the last PreBar trigger. The PreBar collects bar pulse height and beam neutron TOF to bar data. Finally, the FC trigger is triggered by the coincidence of the FC and a bar. The FC collects FC pulse height, bar pulse height, beam neutron TOF to the FC, and bar TOF relative to FC.

4.2.1 Trigger Cuts

The PPAC trigger set the zero time for two important TOFs: the fission neutron TOF from the PPAC to a bar, and the beam neutron TOF to the PPAC. The PPAC trigger cut for the purposes of this analysis also requires that the PPAC triggered on a fission event. The PPAC is sensitive to both fission fragments and alpha particles. To avoid using PPAC triggers that are triggered by alpha particles,

a fission cut is placed on the PPAC pulse height ADC. The alpha particles will manifest themselves in this ADC as a so called alpha tail. This alpha tail appears as a peak in the ADC due to the pulse height threshold of the PPAC's CFD. The fission events generate greater pulse heights thus the fissions manifest as a broad Gaussian peak which overlaps with the alpha tail. Thus the fission cut is created by requiring the PPAC pulse height ADC value to exceed 120 channels. Figure 4.1 shows the PPAC ADC histogram.

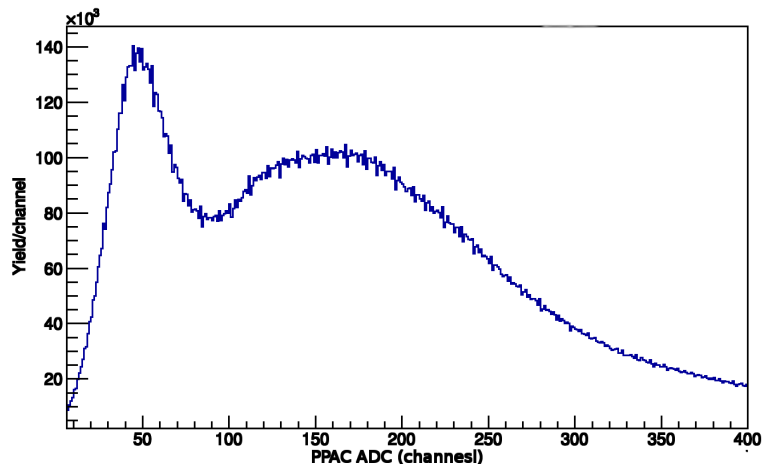


Figure 4.1: PPAC ADC histogram with a PPAC trigger cut but without a fission requirement.

The peak below 100 channels is the alpha tail, while the bump above 100 channels are fission events. The fission event cut is at 120 channels to mitigate the effects of the alpha tail. As its name suggests, alphas create a tail that continues underneath the fission peak. Some alpha events make it past the fission cut and become a form of accidental background. These background events are accounted for in the accidental background calculation by imposing the same fission cut on the PrePPAC trigger.

The PreBar trigger cut during the beam off period allows for ADC calibration data collection. The PreBar trigger cut during the beam on period allows for the bar singles event rate data collection. Figure 4.2 shows a beam TOF histogram with a PreBar cut for a single bar. The yield is proportional to the accidental background and this will become very important when discussing the background

subtraction.

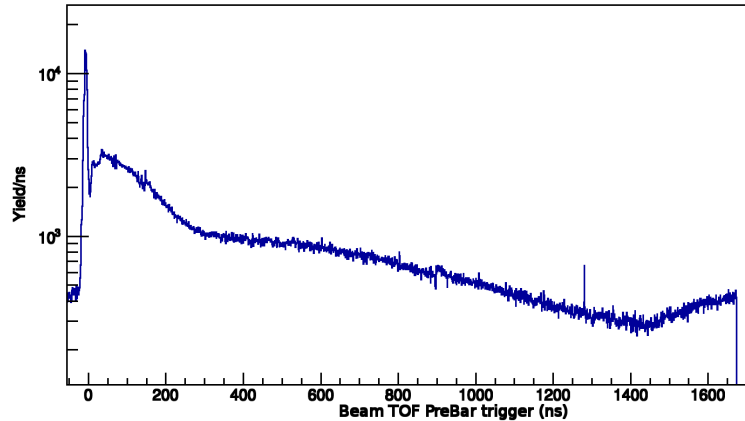


Figure 4.2: PreBar cut beam neutron TOF to PPAC for a single bar.

The gamma flash is much more prominent than in the PPAC triggered TOF histogram because gamma rays directly from the beam have a much better chance of being detected by the bars than causing photo-fission in the PPAC.

The PrePPAC trigger cut is primarily used to measure the singles rate of the PPAC at various times during a beam micro-pulse. Figure 4.3 shows the beam neutron TOF to PPAC histogram which is used to calculate the accidental background along with the similar histogram from the PreBar trigger.

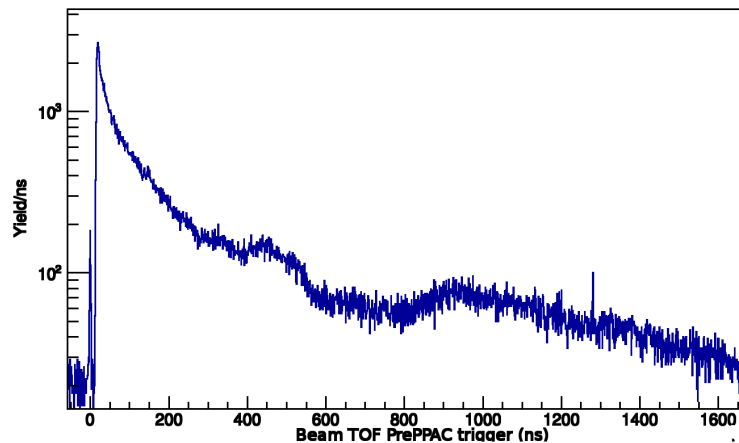


Figure 4.3: PrePPAC trigger cut beam neutrons TOF to PPAC.

The FC trigger is used to collect data that directly measures the shape of the accidental background for comparison with the calculated accidental background. The FC trigger achieves this by setting a cut on the FC ADC to select only alpha

particles. Due to the large 7.3 m FP from the FC to the bars, any coincidence between the detectors is likely accidental. Figure 4.4 shows the beam neutron TOF to FC histogram.

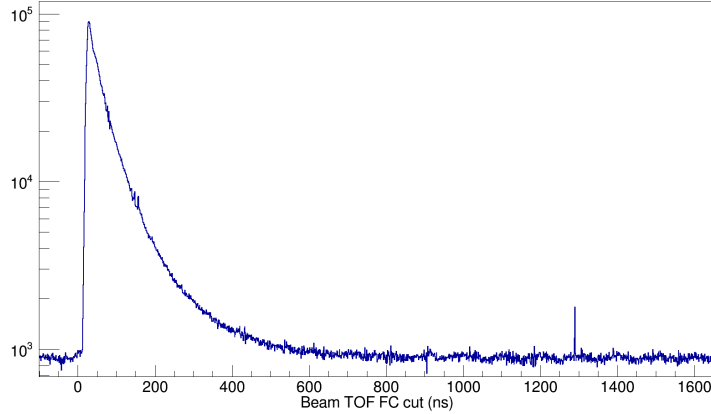


Figure 4.4: Fission chamber trigger cut beam TOF histogram.

The Beam-On/Off trigger requirements are tags that indicate whether a trigger occurred during beam-on or beam-off period. For the PreBar trigger this distinction is very important as during beam on the PreBar trigger is collecting important background data while during beam off it is collecting calibration data.

4.3 Neutron Beam Energy

Neutron beam energy is an important input into the MN model, and so this spectrum must be measured and used to create beam energy cuts. Equation 4.3 is used to calculate the kinetic energy of the neutron that caused a fission event in the PPAC. The FP from the spallation target to the center of the PPAC is 21.5 m. The TOF of the beam neutron is measured using four TDCs due to the 1800 ns between micro-pulses and each TDC only covering 500 ns. When calculating the accidental background a full 1800 ns TOF spectrum is required, thus the four TDCs are unified using a method called 'stitching'. The stitching process involves creating an overlap window in successive TDC channels such that some events are in common between the two TDCs. By plotting these paired TDCs on a 2D histogram the overlapping coverage is obvious. Figure 4.5 shows such an overlap.

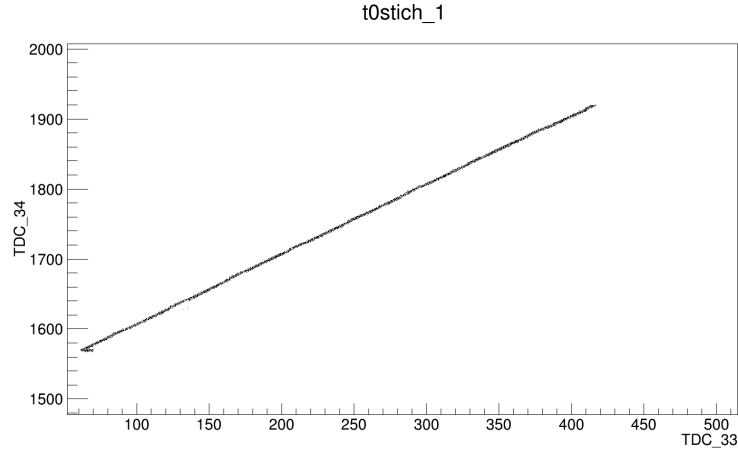


Figure 4.5: Two beam TOF TDCs in a 2D histogram. This histogram shows the overlap between TDC_33 and TDC_34.

For each TDC a start and stop channel is defined using 2D histograms like figure 4.5. The start channel of the first TDC is simply its first channel while its stop channel is defined by selecting an overlap channel with the next TDC in the sequence. This overlap channel is found by making a 2D overlap histogram like figure 4.5, then choosing a TDC channel that lies on the correlation line that is formed. The correlation between the two TDCs forms a line because each TDC has nearly the same ns/channel conversion function which is itself nearly linear. The start of the next TDC is the channel that is paired with the stop of the previous TDC via the correlation line. Continue this method until each of the four TDCs has a start and stop. The last TDC uses its last channel before the overflow as its stop. The starts and stops create a time window for each TDC. Each TDC time window is then calibrated using the techniques discussed in Chapter 2. The first TDC time window has its start time set such that the gamma flash is at time 0 ns. The gamma flash is caused by beam gamma rays inducing photo fission in the PPAC. As an aside, the PreBar and FC triggers have different gamma flash timing due to the difference in FP. These triggers are then given different start times for the first TDC to compensate. Each subsequent TDC then has its start time defined by the start time of the previous TDC plus the time range from start to stop of its time window. Figure 4.6 shows the final beam TOF histogram with vertical black lines indicating where one TDC ends and another begins.

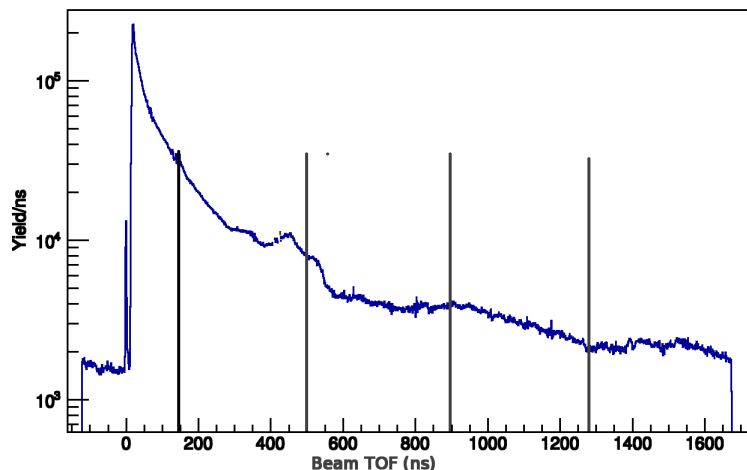


Figure 4.6: Beam TOF histogram with a PPAC trigger. The gamma flash is set to 0 ns. The black vertical lines indicate where one TDC in the stitch chain ends and another begins. They are not equally spaced because not all TDCs have exactly the same number of usable channels.

4.4 Energy Deposition Analysis

The CFD pulse height threshold determines, as a function of neutron energy deposition, the detection efficiency of the bars. The MCNP simulations covered in Chapter 5 can determine this efficiency, but only for neutron energy deposition measured in MeVee. Thus, accurately calibrating pulse height spectra into energy deposition spectra is important for finding the detection efficiency. The steps of the calibration process were covered in Chapter 2 but a brief summary follows.

The pedestal of each ADC is measured by unplugging each detector from its linear gate. A $50\ \Omega$ terminator is then put in place of the input signal. The ADC spectra collected from these runs shows the pedestal as a peak. After the pedestal peaks are recorded the detector signal linear gate inputs are replaced. The pedestal peak channel for each ADC is then subtracted from the measured pulse height channel as part of the energy calibration procedure. During beam-off periods, which is 95% of the runtime, the PreBar trigger collects calibration data. A Th source was placed in the target area which creates 2.6 MeV gamma rays. These gamma rays Compton scatter in the bars and the recoiling electron creates a number of photons proportional to its energy. Compton scattering creates a sharp edge at an

energy of 2.38 MeV that stands above the background and is used for calibration. The ADCs then have their measured pulse-height spectra fit to an exponential background with a Gaussian convoluted step as an approximation for the Compton edge. The fit parameter that defines the edge of the step function is then used to define the Compton edge channel. This Compton edge channel is then used to define the channel-to-energy conversion factor in MeVee.

After calibrating the ADCs, the CFD pulse height threshold manifests itself as an energy deposition threshold. To determine this threshold a method similar to determining a Compton edge channel is used. A peak forms at energies just above the threshold and for energies below this peak there is a sharp decline in yield. Figure 4.7 shows a typical single PMT energy deposition spectrum with a PreBar Beam-OFF trigger. The 2.38 MeVee Compton edge is also visible.

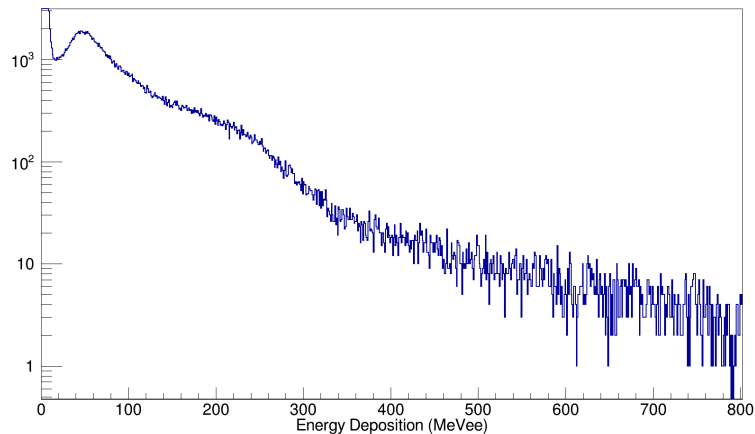


Figure 4.7: Calibrated energy spectrum from a single PMT of a neutron bar. The trigger is PreBar with a Beam-OFF trigger requirement.

The individual PMT energy signals for a single bar are combined using the geometric mean to form an energy deposition for the bar. Due to the fact that the geometric mean is independent of position it is convenient to use this quantity for further analysis instead of the individual PMT deposition measurements. Figure 4.8 shows a geometric mean plot with PreBar Beam-OFF trigger.

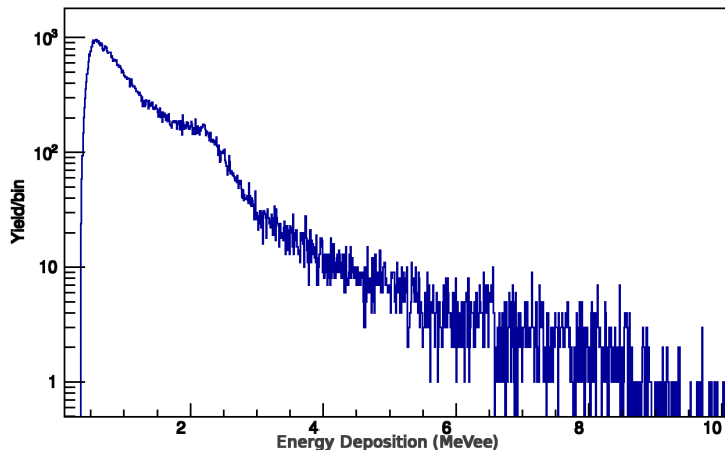


Figure 4.8: Geometric mean energy deposition of a single bar with a PreBar Beam-OFF trigger.

The 2.38 MeV Compton edge is sharper in this plot than in figure 4.7. This is due to the position independence of the geometric mean.

4.5 Kinetic Energy Spectrum $T(E)$

The prompt fission neutron energy spectrum is obtained from the measured TOF spectrum and the measured flight path of the fission neutrons. The flight path (FP) of fission neutrons is the combination of two quantities; the distance from the center of the bar Δx where the neutron was detected, and the distance D from the PPAC to the center of the neutron bar.

$$FP(\Delta x) = \sqrt{\Delta x^2 + D^2} \quad (4.1)$$

The distance from the PPAC to the center of each bar was measured using a tape measure and the distances are listed in Chapter 3. The position relative to center of the bar was measured by taking the time difference between the TDCs of the left and right PMTs of each bar. The time difference was then calibrated by collecting data using a collimated gamma ray source placed at various points along a bar and then measuring the time difference. These data were then fit to a 2nd-order polynomial using a least-squares fit. Equation 4.2 shows the 2nd-order

polynomial used to go from the time difference Δt in ns to bar position Δx in cm.

$$\Delta x = 0.062(\Delta t)^2 + 8.3\Delta t - 2.1 \quad (4.2)$$

The largest time difference measured in the bars is 12 ns, which means the quadratic component never accounts for more than 10% of the relation between position and time difference. Figure 4.9 shows an example Δx plot with a PPAC trigger.

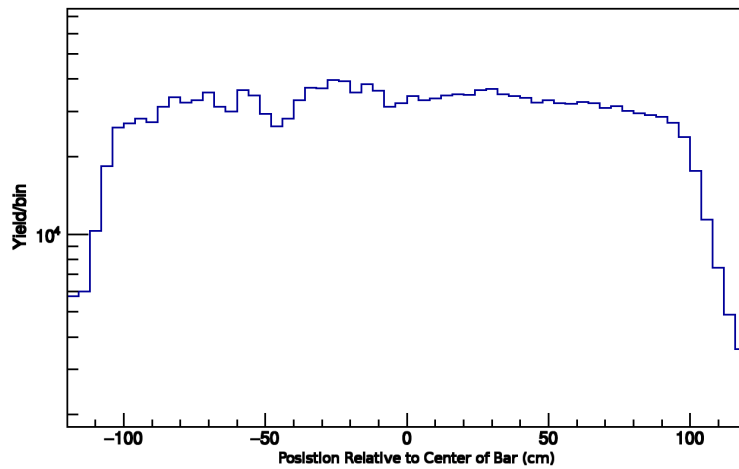


Figure 4.9: Position relative to center of bar with a PPAC trigger.

The step drop-offs at 100 and -100 cm are created at the ends of the 200 cm long scintillator, and thus events cannot physically occur beyond those positions. However, some x positions are measured beyond ± 100 cm. These events beyond 100 cm are the result of finite timing resolution. The CFD and thickness of the bar contribute to a finite timing resolution δt . In fact one method of measuring δt is to fit the edge of the time difference plot using a Gaussian-convoluted step function, similar to how the Compton edge was fitted. The result of this fit was $\delta t=1.8$ ns. Another method to obtain the value of δt is to impose a center-of-bar cut on the bar TOF with a PPAC trigger.

The TOF of the fission neutrons is obtained by calculating the mean of the TOFs measured by each PMT of a bar. The TOF measured by each PMT is dependent on the energy of the neutron, its FP and Δx . However, the mean of the PMT TOFs

is independent of Δx and only depends on FP and the neutron energy. This mean will be referred to as the meantime and will be useful for determining both the accidental backgrounds and the PFNS. Figure 4.10 shows an example meantime spectrum. The neutrons appear in this spectrum, in the region of interest between 40 ns and 100 ns, while the gamma flash is set at 0 ns.

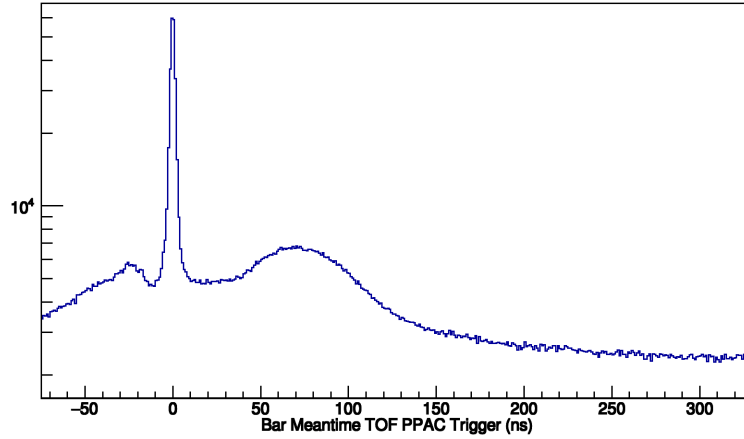


Figure 4.10: Meantime spectrum with a PPAC trigger requirement. The region of interest for fission neutrons is between 40 ns and 100 ns.

With the neutron TOF and FP known, the neutron kinetic energy T is calculated using equation 4.3 with the neutron's rest mass M_n . The quantity T then fills a histogram forming a measured PFNS which includes accidentals. The accidental backgrounds are subtracted later in the analysis.

$$\beta(FP, t_m) = \frac{FP}{FP + c * t_m}$$

$$\gamma = \frac{1}{\sqrt{1 - \beta^2}} \quad (4.3)$$

$$T = (\gamma - 1)M_n$$

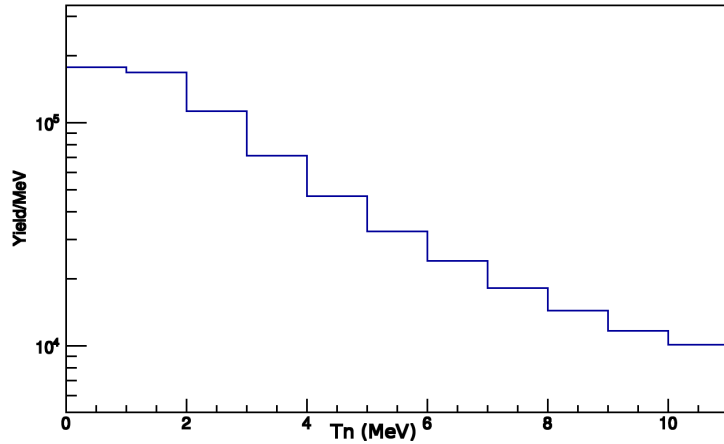


Figure 4.11: Measured neutron kinetic energy spectrum for a single bar without background subtraction.

4.6 Data Cuts

Data cuts are a set of criteria that each event needs to fulfill before it is added to a histogram. The goals of these data cuts are to establish the start time of TDCs in the case of trigger cuts, and in other cases to reduce background contributions. The criteria of a data cut are established by the physical constraints of the experiment. Most data cuts are implemented using an inequality. For example, a software energy threshold might be imposed on the mean bar energy deposition such that only events above 400 keVee make it into the neutron TOF histogram. This software threshold is imposed to ensure all detectors have the same energy threshold despite having different hardware thresholds. Another method of imposing a data cut is to use logical combinations of triggers or other data cuts.

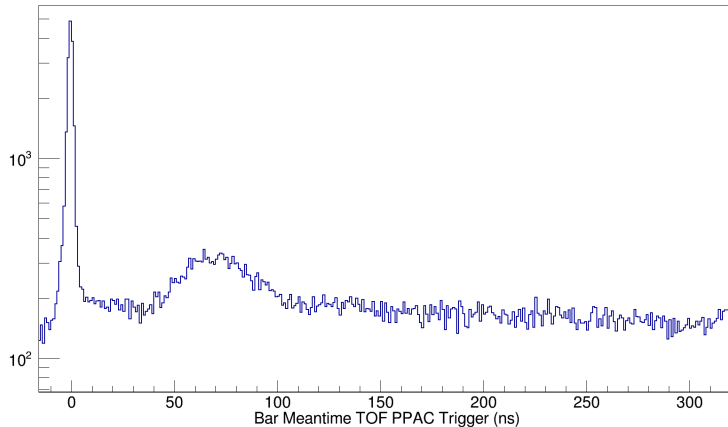


Figure 4.12: Meantime histogram of a single bar with PPAC trigger cut and energy threshold of 400 keVee.

Figure 4.12 shows the effect of an energy threshold on a single bar mean TOF spectrum. The region between the gamma flash and neutron bump at 40 ns is dominated by accidental backgrounds, as is the region beyond 100 ns. Within the 40 to 100 ns window are the fission neutrons plus the accidental contribution.

4.6.1 Sorting

Sorting cuts help reduce backgrounds by removing events that have anomalous behavior or are in a region that produce large backgrounds. The ADC/TDC on-scale cut requires that an event both exceed the software energy threshold, and the TDC measures a TOF less than the overflow. The TDC measures an overflow whenever no stop signal is received before the end of the 500 ns long FERA gate. Since the bars measure low energy events which occur at all times, the ADC on-scale cut removes some accidental coincidences. The beam energy cuts separate single-chance fission events which occur below 5 MeV from multiple-chance fission events which occur above 5 MeV. These beam energy cuts also act as a low-energy threshold and a high-energy cutoff.

The accidental background calculation requires a nearly constant beam frequency because the calculation relies on hour-long average rates to approximate instantaneous rates. The beam stability cut attempts to satisfy this condition by requiring the measured average beam frequency to stay within a specified range. The beam

stability cut did not sort event-by-event, but instead run-by-run to remove runs that did not have a sufficiently stable beam. The stability cut only allows measured average beam frequencies between 95 and 107 Hz as shown in figure 4.4. The average beam frequency was measured using a constant Beam-ON coincident pulser scaler. The number of recorded pulses was directly proportional to the number of beam macro-pulses. A conversion factor was measured by counting the number of pulses for an hour-long run when the beam was known to be at 100 Hz. This conversion factor was then used to determine the average beam frequency for all hour-long runs.

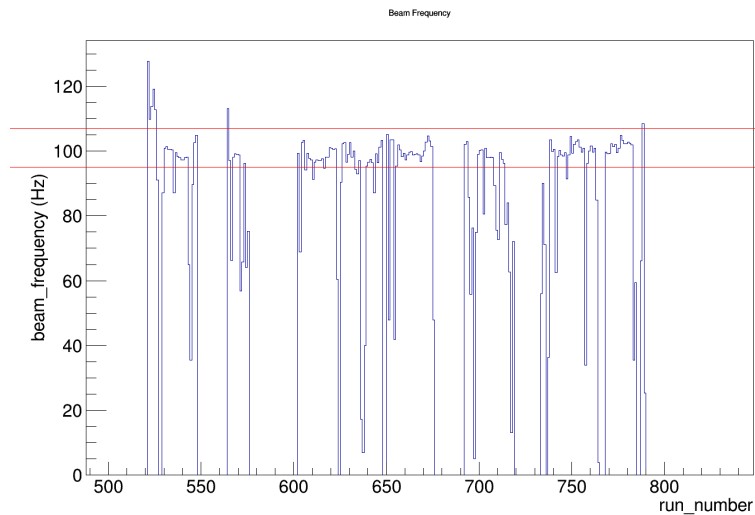


Figure 4.13: Average beam frequency as a function of run number. Only runs with an average frequency between the red lines satisfy the beam stability cut.

4.7 Accidental Backgrounds

4.7.1 Accidental TOF Spectrum

Accidental backgrounds are caused by uncorrelated coincidences between detectors. In this case the uncorrelated coincidence is between a PPAC fission and an uncorrelated bar event. While the FC trigger can measure this background, a more precise approach was used to calculate it using the measured singles rates of both the PPAC and each bar. The method used was developed at LANCSE by John O'Donnell[16] for use in coincidence measurements. The PPAC and bar

singles rates, when combined with the micro-pulse rate, determine the accidental coincidence rate. This is done by calculating the per micro-pulse probability $R_f(t)$ of detecting a fission in the PPAC, and this rate $R_n(t)$ for each bar. The general probability $R_x(t)$ is calculated by the ratio of the Yield(t) and the number of micro-pulses N, as shown in equation 4.4.

$$R_x(t) = \frac{Y_x(t)}{N} \quad (4.4)$$

The quantity $Y_x(t)$ is the measured PPAC or bar total run yield for beam neutrons with TOF t . To differentiate between PPAC fission singles and bar singles, both PrePPAC and PreBar trigger cuts are used. $Y_x(t)$ is scaled by the known prescale factor, since the singles triggers are pre-scaled. The prescale factors are 400 for the bar singles and 50 for the PPAC. Finally, the number of micro-pulses $N=1.29*10^8$ micro-pulses/hour for hour-long runs. Given the singles probabilities R_n and R_f for the bar singles and PPAC, respectively, the accidental probability per micro-pulse is given by equation 4.5. $Y(t_f, t_m)$ is determined for a given beam neutron TOF to PPAC, t_f , and fission neutron TOF from PPAC to bar t_m . The variable t_m is analogous to the measured bar meantime with a PPAC trigger cut.

$$Y(t_f, t_m) = R_f(t_f) * R_n(t_f + t_m) \quad (4.5)$$

The next step in this process is to sum $Y(t_f, t_m)$ over t_f from t_{f1} to t_{f2} . This yields the probability $Z(t_m)$, which is the chance per micro-pulse of an accidental having a TOF t_m . The specific time ranges are shown in the table below.

Table 4.1: Beam time-of-flight ranges

Energy range (MeV)	t_{f1} (ns)	t_{f2} (ns)
1-5	620.6	1476.3
5-10	417.9	620.6

$$Z(t_m) = \sum_{t=t_{f1}}^{t_{f2}} Y(t, t_m) \quad (4.6)$$

The accidental background TOF spectrum $X(t_m)$ is calculated by multiplying $Z(t_m)$ by the number of micro-pulses N .

$$X(t_m) = N * Z(t_m) \quad (4.7)$$

Figure 4.14 shows an overlay of the measured TOF spectrum and the calculated accidental background spectrum for one bar. The accidental spectrum does a good job of not only matching the shape but also the magnitude of the background in the region of interest. Only at long times after the end of fission neutron bump do the measured spectrum and accidentals diverge. It is possible that for those longer times fission neutrons that were emitted incident on the pit or walls could find their way back to the bars and form a coincident background. However, if this is the case then the high up geometry of the bars prevents these neutrons from reaching the detectors in time to contribute to the measured PFNS in the range from 4-10 MeV.

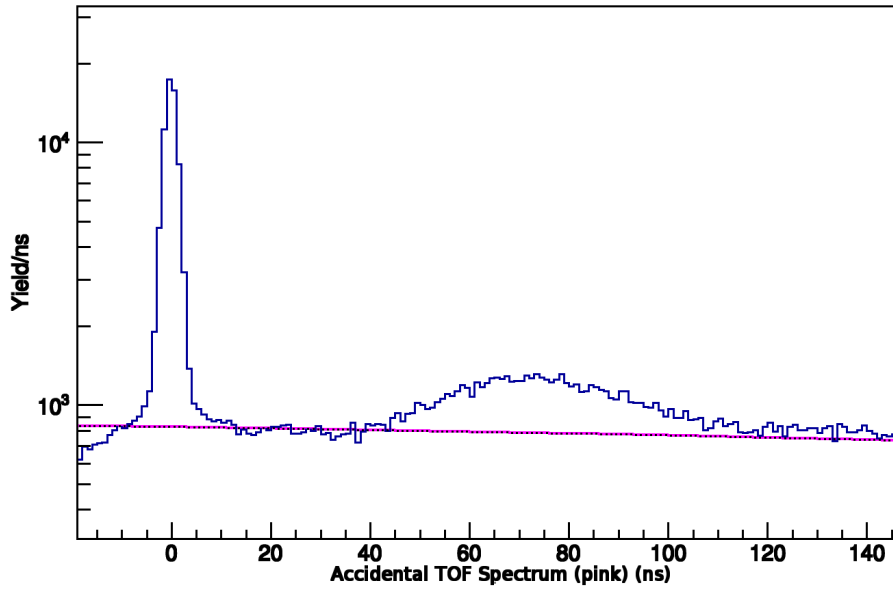


Figure 4.14: Calculated accidental background TOF spectrum (pink) overlaid with a single bar meantime spectrum (blue).

To further test this method the PPAC fission singles rate was replaced in the accidental calculation with the FC alpha singles. This has the effect of calculating the accidental spectrum that is collected by the FC trigger. If this method is viable, then the estimated accidental spectrum should agree with the FC trigger measured accidental spectrum. Figure 4.15 is a demonstration of such a result for beam energy 1-5 MeV.

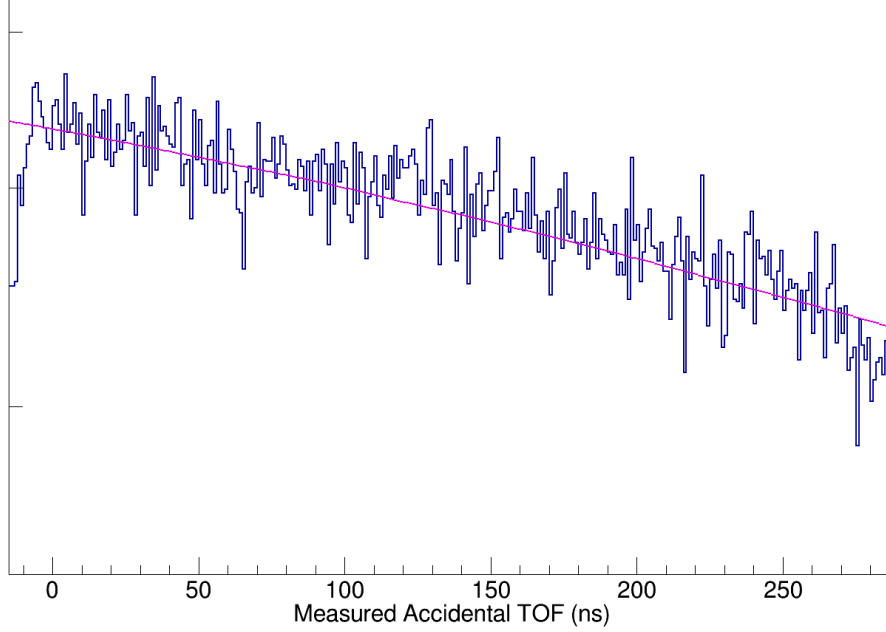


Figure 4.15: Calculated accidental background spectrum in pink. The blue spectrum is a measured accidental background with a FC alpha trigger cut.

The measured accidental spectrum drops to zero at 350 ns not for any physical reason but because that time corresponds to the last non-overflow channel of its TDC. The drop off below 0 ns is caused by the ADC on-scale cut. The reason for this is unknown.

4.7.2 Accidental Energy Spectrum

In the measured data analysis, the FP is a function of a constant perpendicular distance D between the PPAC and the bar center, as well as the hit position Δx of the event relative to the center. The PreBar trigger cut records the measured “TOF” of each bar PMT relative to the bar meantime. The individual bar PMTs measure a time relative to the meantime because the BAR-OR is made up of 16 bar meantimer outputs, and it is the BAR-OR that is the input into the pre-scaler module that creates the PreBar trigger pulse. However, since both PMTs are measuring a TOF that is relative to the same zero time, the time difference of the two PMTs are converted from time difference in ns to Δx in cm position using the same conversion function discussed earlier in this chapter. With this, the FP

is calculated using equation 4.8.

$$FP(\Delta x) = \sqrt{D^2 + \Delta x^2} \quad (4.8)$$

However, part of the strength of the accidental background calculation method is the use of singles trigger data which has high count rates which allows for a high precision calculation of the accidental background. If the PreBar trigger cut beam TOF histograms required a cut for every bar position Δx this advantage would be lost. Therefore, to avoid this an alternative approach that relied on the singles rate at position Δx was used. The probability $P(\Delta x)$ of a singles event occurring at Δx , is calculated by equation 4.9.

$$P(x) = \frac{Yield(\Delta x)}{Yield_{total}} \quad (4.9)$$

The $Yield_{total}$ is the sum over all Δx of $Yield(\Delta x)$.

Since the experimental data are binned per MeV, then the accidental spectrum $A(E)$ is as well. Given an energy bin center E the upper energy E_1 is $E+0.5$ MeV, while the lower energy E_2 is $E-0.5$ MeV. The TOFs $t_1(\Delta x)$ and $t_2(\Delta x)$ are calculated using equations 4.10 and 4.11 with E_1 and E_2 substituting for E . These times represent how long it takes a neutron to travel from the PPAC to a bar at position Δx .

$$\gamma = \frac{E}{M_n} + 1 \quad (4.10)$$

$$t(\Delta x, E) = \frac{FP(\Delta x)}{c} \left(\frac{\sqrt{\gamma^2 - 1}}{\gamma} - 1 \right) \quad (4.11)$$

These times $t_1(\Delta x)$ and $t_2(\Delta x)$ are the lower and upper bounds of a TOF bin with center t_b . The time difference between t_1 and t_2 is the time bin width and it increases with decreasing neutron energy. Summing $X(t)$ (equation 4.7) over t from t_1 to t_2 gives the accidental energy spectrum $B(x,E)$ as a function of position

x relative to the bar center.

$$B(x, E) = \sum_{t=t_1(x,E)}^{t_2(x,E)} X(t) \quad (4.12)$$

Finally, summing over all x positions gives the accidental energy spectrum A(E).

$$A(E) = \sum_{x=-100cm}^{100cm} P(x)B(x, E) \quad (4.13)$$

The net, accidental-corrected PFNS N(E) is obtained by subtracting A(E) from the ETOF spectrum T(E) on an energy bin-by-bin basis.

4.8 Coincident Backgrounds

Coincident backgrounds, unlike accidentals, are due to true coincidences between the bars and PPAC. However, these coincidence events are not direct prompt fission neutrons. One example of such a background is delayed fission neutrons. These neutrons are emitted by beta decays of the fission fragments after fission. However, this source of background is not significant thanks to two key points. First, the delayed nature of these neutrons means they are unlikely to reach the bars within 100 ns of the prompt gamma rays, thus they will not be in the region of interest. Second, within 500 ns prompt neutrons far outnumber delayed neutrons, by a factor of 100 to 1. This ratio was found using an MCNP simulation where a 1 mm diameter sample of ^{235}U was put in the path of a mono-energetic neutron beam of 4 MeV. The neutron outward flux around the sample was measured as a function of time. Only MCNP events with fissions were counted in the tallies to avoid counting outgoing beam neutrons.

Along the same vein are delayed gamma rays which despite their name are still emitted within 10 ns of fission. This short time window means the delayed gamma rays reach the bars long before the 40 ns when the first prompt neutrons arrive.

Another coincident background is due to mistimed prompt neutrons. This is not

a true background in the sense that these are prompt fission neutrons. However, these neutrons did not take a direct path to the bars from the PPAC and instead scattered off of something in the room, usually the floor or walls. If these neutrons take longer than 350 ns to reach the bars then they are effectively the same as the sea of beam neutrons that make up the accidental background. Only when the mistimed neutrons reach the bars within the 350 ns are they coincident, and therefore not accounted for in the accidental background calculation. To mitigate the effect of these neutrons the bars were placed high in the air above a pit.

Some neutrons were mistimed due to scattering within a bar or from bar-to-bar scattering. These cases are best handled using simulations. Bar-to-bar scattering was found to be around 2% of measured fission neutron events. This was found using an MCNP simulation. This simulation involved firing neutrons, with an input energy spectrum given by the MN model at a single bar in the bar array and counting how many neutrons were detected in other bars. The result was 2% of all incident fission neutrons scatter into another bar and are detected. However, nearly all of these detected scattered neutrons end up in directly adjacent bars. This is due to the small distance between directly adjacent bars and a shielding effect caused by the fact that nearly all of the solid angle to the left and right of a bar is covered by the nearest neighbors.

4.9 Uncertainty Analysis

The final PFNS $N(E)$ is calculated by doing a bin-by-bin subtraction of the total ETOF spectrum $T(E)$ minus the accidental spectrum $A(E)$.

$$N(E) = T(E) - A(E) \tag{4.14}$$

The ratio of $N(E)$ to $A(E)$ varies depending on fission neutron energy. For 10 MeV neutrons it is nearly 1 to 15, while for 3 MeV neutrons it is close to 1 to 1. Due to the low signal to background ratio, the uncertainty in the higher energy bins is

dominated by the uncertainty in the total number of counts of the ETOF spectrum σ_T .

$$\sigma_T = \sqrt{T} \quad (4.15)$$

The uncertainty of N, σ_N , depends on the uncertainty of T, σ_T , and the uncertainty in the accidental spectrum, σ_A . Each of these uncertainties is calculated on an energy bin-by-bin basis.

$$\sigma_N = \sqrt{(\sigma_T)^2 + (\sigma_A)^2} \quad (4.16)$$

The uncertainty σ_A depends on P(x) the probability per micro-pulse of measuring an accidental background at position x relative to the bar center, B(x) the accidental energy spectrum as a function of bar position x, and their respective uncertainties.

$$\sigma_A = \sqrt{\sum_{x=-100cm}^{100cm} ((B(x)\sigma_P)^2 + (P(x)\sigma_B)^2)} \quad (4.17)$$

The uncertainty σ_P is calculated using the yields Yield(x) of the various 5 cm bins along the bar position spectrum, with a PreBar trigger cut, divided by the sum of those yields Yield_{total}.

$$\sigma_P = P(x) \sqrt{\frac{1}{Yield(x)} + \frac{1}{Yield_{total}}} \quad (4.18)$$

Since B(x) is the sum of X(t) over the fission neutron TOF t from t₁ to t₂, the B(x) uncertainty depends on σ_X .

$$\sigma_B = \sqrt{\sum_{t=t_1(x)}^{t_2(x)} \sigma_X^2(t)} \quad (4.19)$$

Finally, $\sigma_X(t)$ depends directly on the yields of the singles beam TOF spectra of the neutron bars $Y_n(t_f+t)$, and PPAC $Y_f(t_f)$, and the number of micro-pulses N .

$$\sigma_X(t) = \sqrt{\sum_{t_f=t_{f1}}^{t_{f2}} \frac{Y_f(t_f)Y_n(t_f+t)(Y_f(t_f) + Y_n(t_f+t))}{N^2}} \quad (4.20)$$

Despite this long calculation, σ_A makes up 10% of the error of the 10 MeV energy bin, while σ_T is responsible for remaining error. For the other energy bins σ_A is negligible and σ_N could be approximated as $\sigma_N=\sqrt{T}$. This implies that statistics are the limiting factor with this measurement, and increasing the runtime in a future experiment will lead to more accurate results.

Chapter 5

MCNP Simulations

5.1 MCNP Pre-Processor and ^{228}Th Simulation

Simulations are used to create virtual experiments. The benefit in doing this is complete control of the simulated experimental variables. This allows for the isolation of certain phenomena or the extraction of difficult to measure quantities. These simulations are done using the Monte Carlo neutron transport code called “Monte Carlo N-Particle Transport Code” (MCNP)/`citemcnp`. MCNP has been in development at Los Alamos National Lab (LANL) since the late 1950’s. MCNP is very good at simulating interactions of neutrons and gamma rays. MCNP does not handle optical scintillation light propagation via refraction. Instead the photons are treated like gamma rays and interact with the material as a particle. This leads to an enormous number of calculations for each simulated event. To combat, this optical photons are not allowed to propagate by setting the gamma ray creation threshold above 10 keV. Since optical scintillation light is not propagated the energy deposition of each interaction is found via the particle track file (PTRAC) created at the end of each simulation. The PTRAC file is a large ASCII file that details every interaction line by line. Fig. 5.1 shows an example PTRAC file. The most important pieces of information extracted from these files are interaction time, position, energy, and particle type.

```

-1
%CNP      6                      05/08/13 08/06/18 14:30:49
=ff
1.4000E+01 1.0000E+00 1.0000E+02 0.0000E+00 3.0000E+00 2.0000E+00 1.0000E+00 5.0000E+00 1.0000E+00 1.0000E+00
0.0000E+00 1.0000E+00 2.1475E+09 1.0000E+00 1.0000E+04 0.0000E+00 0.0000E+00 0.0000E+00 0.0000E+00 0.0000E+00
1.0000E+00 2.0000E+00 0.0000E+00 0.0000E+00 0.0000E+00 0.0000E+00 0.0000E+00 0.0000E+00 0.0000E+00 0.0000E+00
2 7 9 8 9 8 9 8 9 8 9 0 4 0 0 0 0 0
1 2 7 8 9 16 17 18 19 20 21 22 23 24 25 26 27 28 7 8 10 11 16 17 18 19 20 21 22 23
24 25 26 27 28 7 8 12 13 16 17 18 19 20 21 22 23 24 25 26 27 28 7 8 10 11 16 17 18 19
20 21 22 23 24 25 26 27 28 7 8 14 15 16 17 18 19 20 21 22 23 24 25 26 27 28

1 1000
5000 1 40 1 21 0 0
-0.78711E+02 0.00000E+00 0.15000E+03 0.00000E+00 0.41651E-01 0.99913E+00 0.24094E+01 0.99900E+00 0.00000E+00
2030 4 2 1 1 20 2 12
-0.26681E+03 0.80425E+02 -0.10796E+01 -0.62029E+00 0.12176E+00 -0.77487E+00 0.39979E-02 0.99891E+00 0.12154E+03
5000 5 1001 -99 9 20 2 0
-0.26681E+03 0.80425E+02 -0.10796E+01 -0.70084E+00 -0.52760E+00 0.48007E+00 0.78722E-02 0.99891E+00 0.12154E+03
2030 5 2 2 9 20 2 60
-0.26681E+03 0.80425E+02 -0.10796E+01 -0.10451E-01 -0.78049E+00 0.62508E+00 0.10000E-02 0.99891E+00 0.12154E+03
5000 5 1001 -99 9 20 2 0
-0.25599E+03 0.80592E+02 -0.22518E+01 0.51144E-01 -0.49280E+00 0.86864E+00 0.21848E-02 0.99894E+00 0.11308E+03
2030 5 2 3 9 20 2 30
-0.25599E+03 0.80592E+02 -0.22518E+01 -0.58511E-01 0.70239E+00 -0.70938E+00 0.10000E-02 0.99894E+00 0.11308E+03
5000 5 1001 -99 9 20 2 0
-0.25356E+03 0.87239E+02 -0.71521E+00 0.84656E-01 0.39526E+00 -0.91466E+00 0.45237E-01 0.99896E+00 0.10460E+03
2030 5 2 4 9 20 2 123
-0.25356E+03 0.87239E+02 -0.71525E+00 0.72030E+00 0.42673E+00 -0.54688E+00 0.10000E-02 0.99896E+00 0.10460E+03
5000 3 1001 -99 9 10 1 0
-0.79471E+02 0.64505E+01 0.29445E+03 -0.76862E-01 0.99326E+00 0.86783E-01 0.29982E-01 0.99897E+00 0.69193E+01
2030 3 2 5 9 10 1 85
-0.79471E+02 0.64506E+01 0.29445E+03 0.60734E-01 0.92458E+00 0.37611E+00 0.95017E-03 0.99897E+00 0.69193E+01
5000 3 1001 -99 9 10 1 0
-0.78911E+02 0.61392E+01 0.29408E+03 -0.41982E+00 0.26986E+00 -0.86656E+00 0.16980E+01 0.99898E+00 0.67588E+01
9000 3 2 6 9 10 1 204
-0.78913E+02 0.61407E+01 0.29407E+03 0.53355E+00 -0.45037E+00 -0.71589E+00 0.40026E-03 0.99898E+00 0.67593E+01
2 1000

```

Figure 5.1: Example PTRAC output file. Boxed in red is a single event “line”. The first line includes some header information such as what type of interaction is taking place, which particle is tracked, etc. The second line indicates quantities, such as position, energy, and time.

The PTRAC files are analyzed using a pre-processor code, separate from MCNP, which reads the file and extracts events which occur inside a neutron bar cell. A cell in MCNP is a well defined closed volume, such as a detector or the room surrounding it. When the pre-processor find a PTRAC event that includes a recoiling electron or proton, it records the time, energy and position. Then with this information the code simulates propagating light. First, the scintillation light is generated. For electrons the amount of light generated is proportional to its energy loss in keV. The number of photons generated N is determined by Birk’s Law[17] given by equation 5.1, with dE/dx the energy loss, S the scintillation efficiency, and k_b Birk’s constant.

$$\frac{dN}{dx} = S \frac{\frac{dE}{dx}}{1 + k_b \frac{dE}{dx}} \quad (5.1)$$

For electrons, k_b is close to zero, so light production is proportional to energy loss of the electron. Since the neutron bars are large compared to the average path

length of the electrons (a few millimeters) a simplifying assumption is made that all of the recoiling electron's energy is deposited. Thus the energy the electron has at the time of its creation is used to determine the number of photons to propagate. While MCNP does not propagate photons the pre-processor code is designed to. The creation time is recorded for use in determining the detection time. Once the energy of an electron is known a number of photons are generated. For the neutron bars there are 55 photons per MeVee of recoiling electron energy. This number was measured by first measuring the pulse height of a single photoelectron in a oscilloscope. Then, using a Na source, the pulse height of the 1068 keV Compton edge was measured again using an oscilloscope. From there the conversion of MeVee to photons $N(E)$ is calculated via equation 5.2, with V the measured voltage of the 1068 edge, and V_{single} the voltage of a single photoelectron.

$$N(E) = \frac{V}{V_{single}} \quad (5.2)$$

For recoiling protons the number of photons per MeV energy loss is not a linear relationship like it is for electrons. Therefore the proton recoil response of the plastic scintillator was measured. The details of this experiment are covered in Appendix C. The result of this experiment was a quadratic equation that related proton energy loss in MeV to MeVee. With this relationship proton recoil energy is converted into MeVee and from there to a number of photons using the same 55 photon/MeVee as for electrons. Equation 5.3 shows this relationship with, E in MeV.

$$E_{MeVee} = 2.01 * 10^{-5} * E^2 + 0.330 * E \quad (5.3)$$

To propagate the light produced, the pre-processor first divides the light into leftward and rightward halves. To do this a Gaussian approximation of the binomial distribution with probability $p=0.5$ was used. The mean of a Gaussian

approximating the binomial distribution is given by $\mu = Np$ and the variance by $\sigma^2 = Np(1 - p)$. Thus, in this case, the mean of the Gaussian is $N/2$ and the sigma is $\sqrt{N/4}$. This gives the normal distribution, equation 5.4, from which pre-processor samples the leftward photons N_L . Once N_L is sampled the rightward photons N_R can be obtained by simply subtracting N_L from the total number of photons N .

$$P(n) = \exp\left(\frac{-(n - N/2)^2}{N/4}\right) \quad (5.4)$$

From the PTRAC file the position of the recoiling particle inside the bar was obtained. By aligning the bar geometry such that the x-direction is parallel to the length of the bars and the center of each bar is at $x=0$ cm, then the x-coordinate from the PTRAC file is the x-position along the bar. Equation 5.5 is used to determine how much light reaches a PMT for both leftward and rightward light. The length of the bar is denoted as L and is about 200 cm. The attenuation length λ is also about 200 cm for the plastic scintillators.

$$\begin{aligned} N_l &= N_L \exp\left(\frac{-x - \frac{L}{2}}{\lambda}\right) \\ N_r &= N_R \exp\left(\frac{x - \frac{L}{2}}{\lambda}\right) \end{aligned} \quad (5.5)$$

Once the photons reach a PMT they are further subjected to a Poisson distribution to account for the efficiency of the PMT. The number of photo-electrons produced in the PMTs is sampled from a Poisson distribution with a mean of $N/4$ where N is the number of leftward N_l or rightward photons N_r reaching the PMT. The final number of photo-electron counts is then tallied by ROOT and sorted into a photon count histogram. Finally, a mono-energetic isotropic gamma ray source is placed in the center of the bar arc and simulated. The results of this simulation are used to calibrate the photon count histograms by finding the Compton edge via fitting a Gaussian convoluted step function. Figure 5.2 shows a 2.6 MeV gamma ray simulation used to calibrate later simulations. The x-axis in the figure has

already been calibrated to keVee. Only one calibration point is needed as there is no pedestal in the simulation and the number of photons/MeVee is fixed for gamma rays (at least in the 0.1 to 10 MeV energy range).

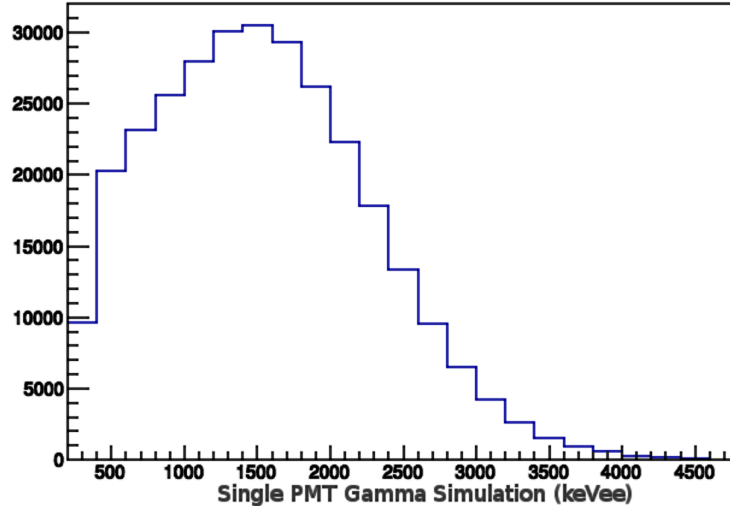


Figure 5.2: A simulated Compton edge of a 2.6 MeV gamma ray for one PMT. Each bin represents a different integer number of photo-electrons.

In order to simulate threshold effects, an energy threshold was set for each side of the bar. An event is only added to the final analyzed spectra if both PMT signals overcome their respective energy thresholds. Both sides are required because this is how the DAQ of the experiment is set up, as only events with both PMTs measuring something above threshold can trigger the DAQ. To get over the threshold either a single event needs to have an energy greater than the threshold energy or several events within a specified time gate need to add up to be greater than the threshold. The gate window simulates the DAQ FERA gate. The gate period is set such that usually only a single detector pulse can make it into the gate. However, occasionally two or three pulses can fit into a single gate, increasing the measured energy. This typically happens because a particle interacts multiple times in the detector before scattering out or being captured. To measure the TOF from the simulation, the creation time from the PTRAC file was collected. This time is referenced to when the source particle of the simulation was created. The source particle's creation time is $t=0$ ns. The creation time is

equal to the TOF of neutrons from PPAC to bars if the source is placed at the location of the PPAC. However, each PMT measures not just the TOF but also how long it takes the generated photons to reach them. To simulate this effect the position-dependent time delay t_l and t_r to each PMT is given by equation 5.6.

$$\begin{aligned} t_l &= \frac{L}{2c_n} + \frac{x}{c_n} + \delta t_l \\ t_r &= \frac{L}{2c_n} - \frac{x}{c_n} + \delta t_r \end{aligned} \tag{5.6}$$

These times are then added to the TOF to create histograms as simulated TDC's. The index of refraction for the bars is 1.58. This means the speed of light c_n in the bars is 19.0 cm/ns. The photons do not always travel in a straight line from the event to the PMT. The photons occasionally totally internally reflect off the surfaces of the scintillator and these reflections lead to a longer travel time. This increase in travel time is calculated by the δt terms given by equation 5.7. The value of b was measured by adjusting it such that the simulated and measured time difference histograms had the same maximum time difference. The measured value of $b=0.005$ per cm.

$$\begin{aligned} \delta t_l &= \frac{b(L/2 + x)^2}{c_n} \\ \delta t_r &= \frac{b(L/2 - x)^2}{c_n} \end{aligned} \tag{5.7}$$

At this point the pre-processor's job is done and a ROOT tree file is created with 32 ADCs and 32 TDCs of simulated event data. There are also histograms that log the particle type that deposited the energy, which was either an electron or a proton. At this stage the simulated data are analyzed using nearly identical methods to the experimental data.

5.2 ^{252}Cf Simulation

Built into MCNP6 is a spontaneous ^{252}Cf source that simulates prompt fission neutrons as well as prompt fission gammas. The prompt neutron and gamma

ray energies distributions were sampled from the LLNL model as described in the MCNP user manual[18]. The LLNL model samples the total fission energy release then distributes the energy among; the kinetic energy of the fragments, the prompt neutrons and gamma rays. For each simulated fission event energy conservation is imposed on this distribution process. A ^{252}Cf simulation geometry is used which mimics the experimental geometry of WNR 15L. The bars are in an arc 1.8 m above the source with a 3 m deep pit below. The ^{252}Cf source emits neutrons and gammas isotropically. After the simulation is over and the pre-processor has created a ROOT file with all the ADCs and TDCs, the ROOT file is then analyzed.

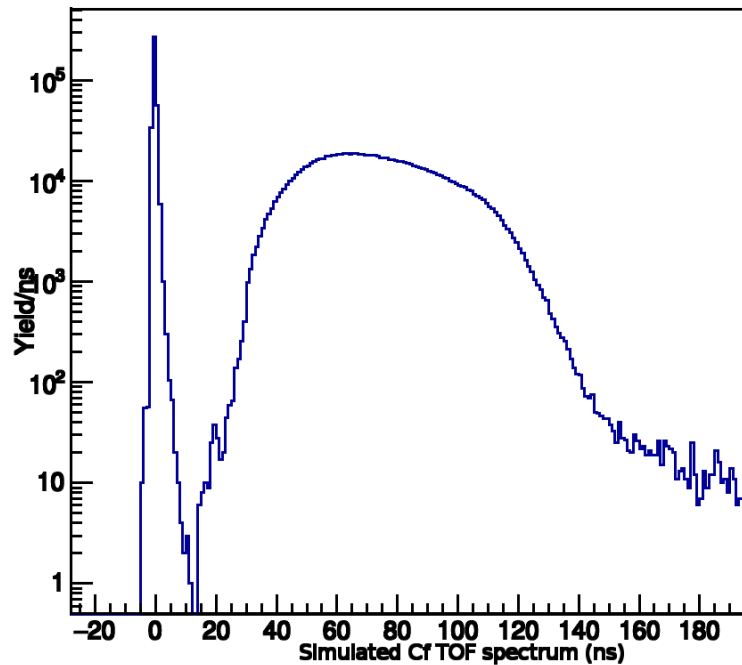


Figure 5.3: Simulated TOF spectrum with ^{252}Cf source. The gamma flash is set to 0 ns as it is for experimental data. The sharp drop off after 120 ns is due to the energy threshold of 150 keVee. The events that occur after 120 ns are due to neutrons hitting concrete and creating gamma rays.

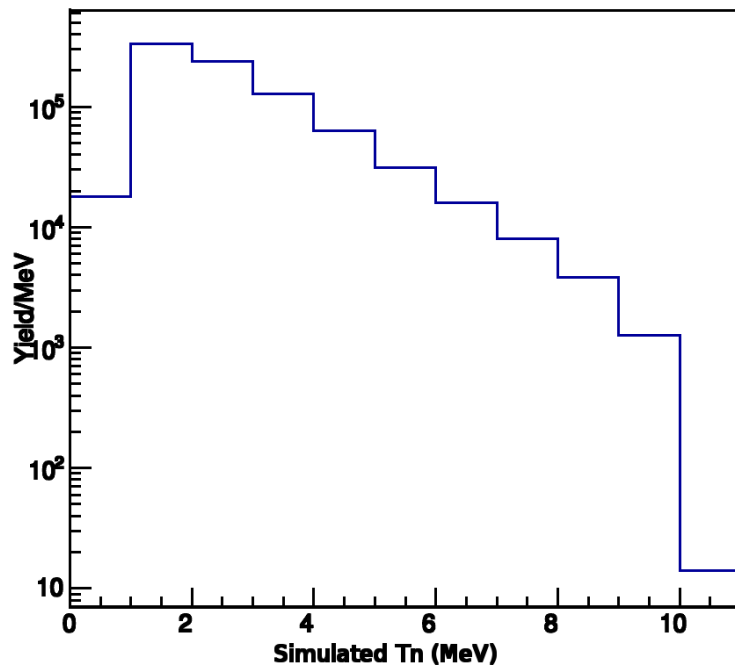


Figure 5.4: Simulated ^{252}Cf prompt fission neutron energy spectrum.

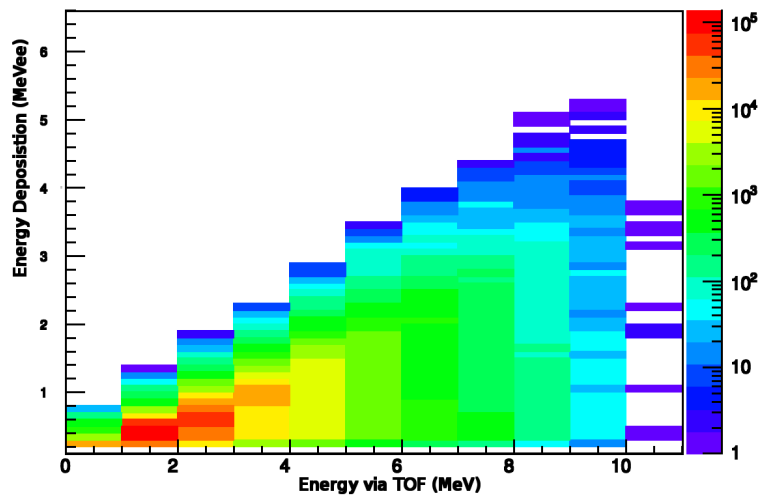


Figure 5.5: Energy via TOF vs energy deposition of a simulated ^{252}Cf source, with gamma rays turned off.

The energy via TOF vs energy deposition, figure 5.5, shows how neutrons of a given kinetic energy T_n deposit energy. The upper linear edge of the distribution are neutrons that deposited all of their energy, some of which did so through multiple scattering. The continuum that goes from the upper edge to zero energy deposition represent neutrons that scattered once and left the detector, leaving

behind only a fraction of their energy. The TOF of these neutrons however, still reflects the correct energy via TOF. This is thanks to the fact that CFD timing is independent of energy deposition, so long as the amount of energy deposited is larger than the energy threshold.

5.3 Madland and Nix $n+^{235}\text{U}$ simulations

Simulations were done using Madland and Nix (MN) PFNS as the input spectra for MCNP. MCNP supports manually defined source particle energy distributions. To do this the MN spectrum is converted from a relative distribution into a cumulative distribution. This is done because it is simpler to input into MCNP. Once this was done the MCNP simulations were run with the source emitting neutrons isotropically. However, only one neutron is emitted at a time. The source was positioned 1.8 m from the bar arc in a similar position to the PPAC. To increase statistics the simulations were run on University of Kentucky's DLX computer cluster. After the simulations were done, the data were analyzed using same analysis code as the experiment with a few exceptions. Most notably the initial source particle energy was tracked and recorded in its own histogram for comparison with the neutron energy via TOF (ETO) result. This comparison can be used to measure the bar response function (although this was not done during the scope of this work). The initial fission neutron energy spectrum was also used to calculate the detection efficiency of the detectors. This was done using a special version of the simulation. The source angular distribution was changed from isotropic to a beam and the beam aimed directly at one of the bars. Since all of the neutrons were directed at a single bar the detection efficiency for a given energy is the number of neutrons detected divided the number emitted incident on the bar. This beam was then swept over the length of the bar to get the efficiency as a function of position as well.

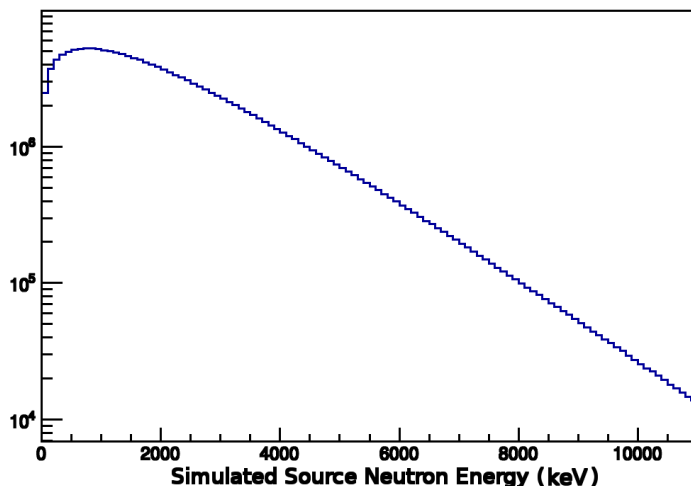


Figure 5.6: MN model source neutron energy distribution.

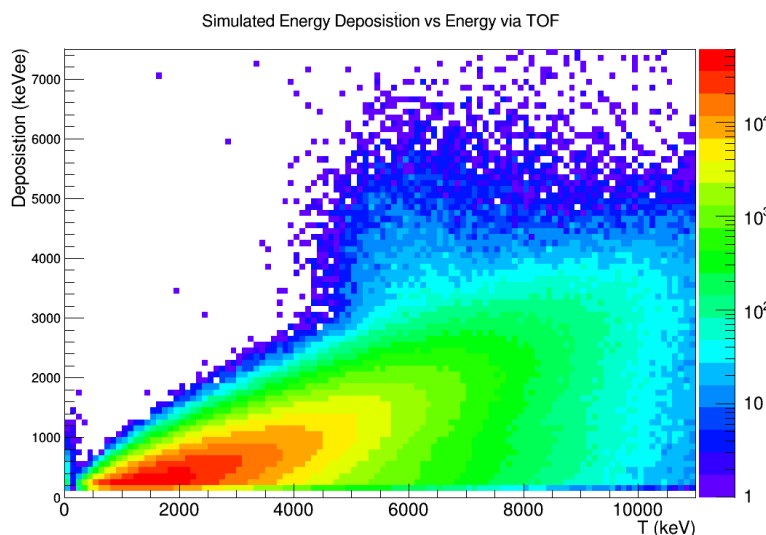


Figure 5.7: Simulated energy deposition vs ETOF using MN source neutrons.

The lobe centered around 6 MeV etof is caused by the $2+$ transition of carbon 12. This transition has a Q -value of around 6 MeV ETOF. Thus a gamma ray of 4.4 MeV is emitted along with the scattered neutron carrying away the excess energy. The light produced by an electron recoil of a 4.4 MeV gamma ray can be much larger than a 4.4 MeV neutron. Thus whenever one of these inelastic collisions occurs a larger energy deposition is measured than would be expected. Further the scattered neutron can also be detected which increases the light production. The lobe shape is caused by a combination of the inelastic scattering cross-section which has a peak at 6.1 MeV and the fact that as the energy

increases the number of neutrons exponentially decreases.

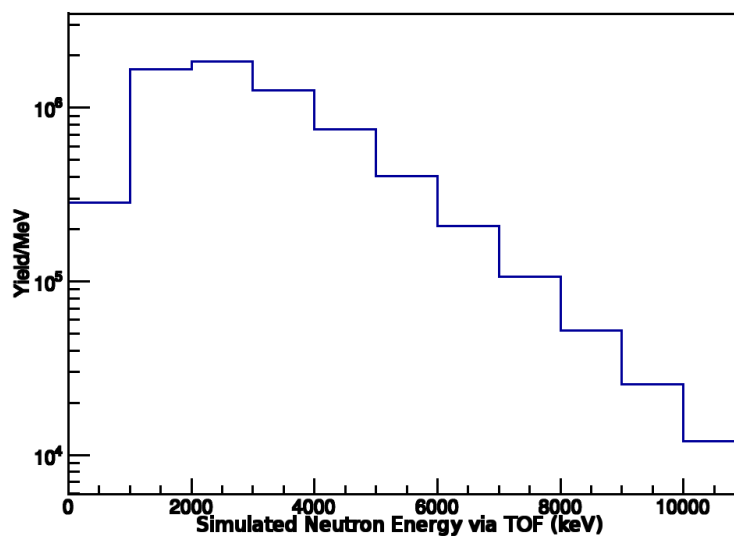


Figure 5.8: Simulated energy via tof spectrum with the MN input spectrum for beam energies between 1 and 5 MeV.

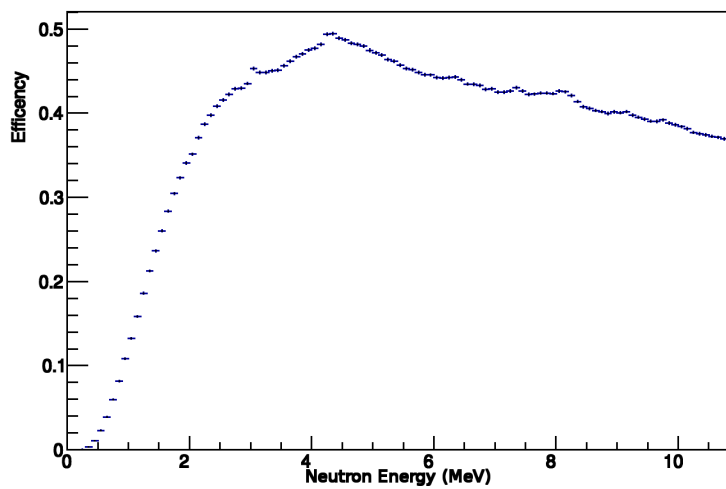


Figure 5.9: Neutron detection efficiency spectrum with 100 keV bins.

Chapter 6

Results

6.1 ^{252}Cf Analysis and Results

One weakness of the ^{235}U PPAC is it is difficult to check if the DAQ setup is working properly. This because the backgrounds from the beam are intense and the fission neutron event rate is low. One way around this is to replace the ^{235}U PPAC with a ^{252}Cf PPAC. Since ^{252}Cf is a spontaneous fission source it does not require a neutron beam to produce fission neutrons. Therefore the beam shutter was closed while the ^{252}Cf data were collected and analyzed to ensure the DAQ worked properly. With the shutter closed and ^{252}Cf being a spontaneous fission source, the accidental backgrounds lost their beam TOF to PPAC dependence. This meant that the accidental background calculation method used for U does not apply to ^{252}Cf . Instead an additional data cut was made to distinguish between uncorrelated backgrounds and fission neutrons. With a PPAC trigger cut, the measured bar TOF and bar energy deposition were correlated, as seen in the ^{252}Cf simulation. A 2D histogram is created with one axis being the energy via TOF (ETOF) and the other axis the energy deposition. A 2D cut is then applied such that any event inside a defined shape satisfies that cut and is included in the final PFNS for ^{252}Cf . The exact shape of the 2D cut is chosen such that only events that have at least some correlation between energy deposition and energy via TOF make it past the cut. Figure 6.1 shows the 2D cut and 2D histogram for a single bar.

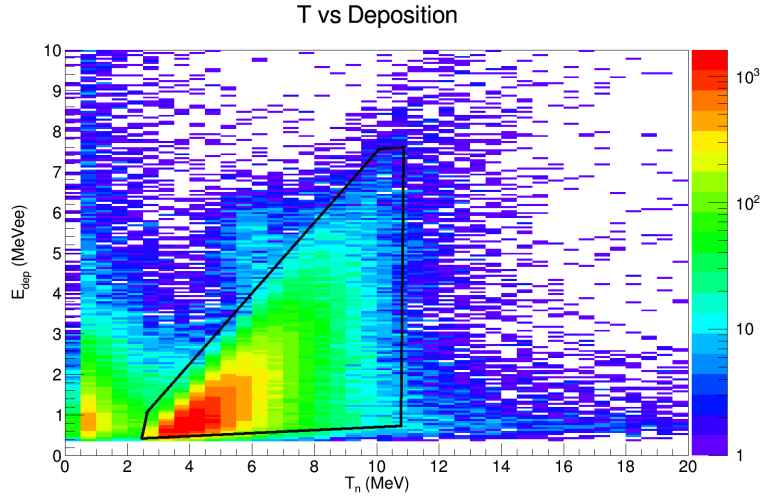


Figure 6.1: Energy deposition vs energy via TOF for a single bar. The events inside the black outline satisfy the 2D cut and are sorted into the final PFNS for ^{252}Cf .

The ^{252}Cf PPAC produced more fission events with much lower backgrounds. This meant that each bar had high enough statistics to compare with the simulation on a bar-by-bar basis. The bar-by-bar comparison is shown in figure 6.2 of the measured PFNS vs the simulated spectrum. The agreement between the simulation and experimental data shows that the DAQ and analysis yield reasonable results in a low background environment.

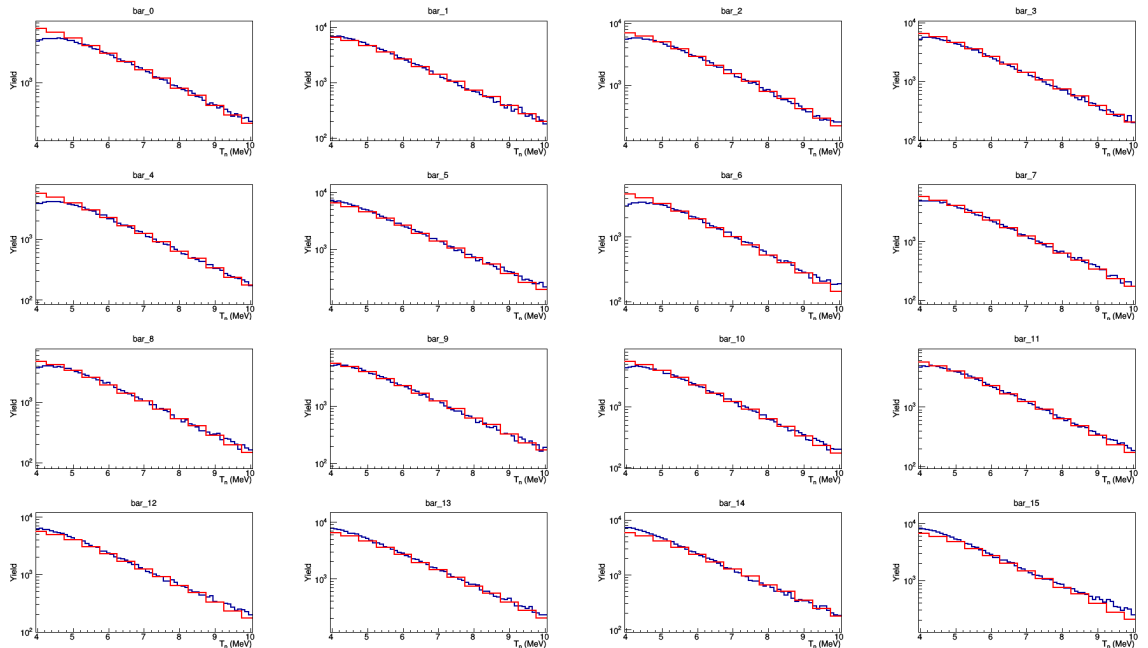


Figure 6.2: All 16 bars measured spectra compared with the ^{252}Cf MCNP simulation. The simulation is in red and the data are in blue.

6.2 ^{235}U Results

The PFNS of ^{235}U was measured and analyzed using a double TOF method for two beam energy ranges, 1-5 MeV and 5-10 MeV. Simulations using the MN PFNS as an input spectrum were also done for comparison with the measured spectra. The result of this work is shown in figures 6.3 and 6.4.

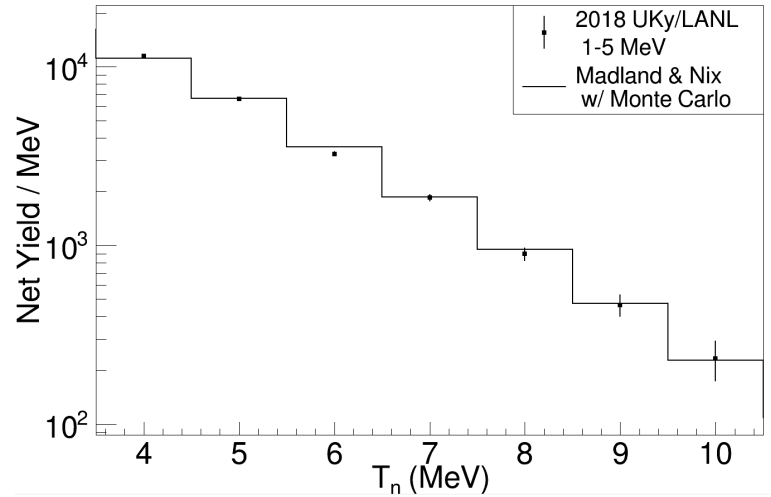


Figure 6.3: All bar ^{235}U PFNS added together, with background subtraction, over a beam energy range of 1-5 MeV, with a PPAC trigger cut.

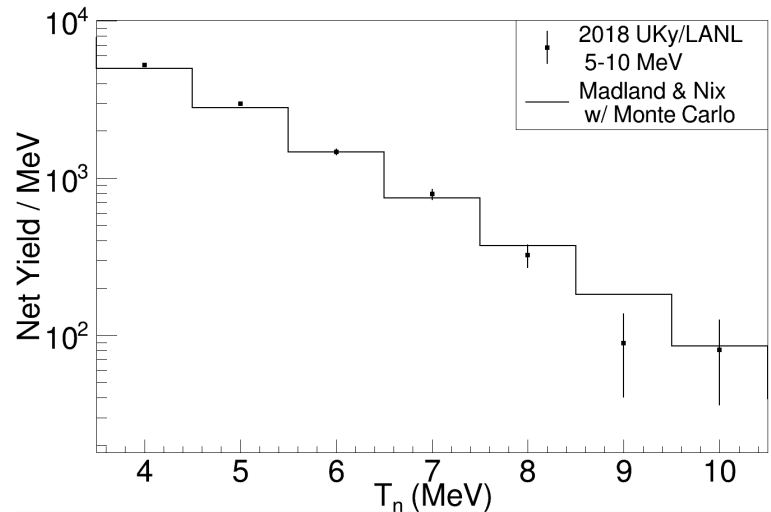


Figure 6.4: All bar ^{235}U PFNS added together, with background subtraction, over a beam energy range of 5-10 MeV, with a PPAC trigger cut.

Both comparisons show good agreement with the simulation. This implies the experimental results agree with the MN calculated PFNS over this energy

range. More importantly this shows that the fundamental methods used in this experiment are effective means to measure the PFNS.

6.3 Conclusions

The 16-bar array had detection efficiency greater than 40% at most fission neutron energies, and covered a large solid angle, $\tilde{1}$ sr. The high up geometry helped reduce potential backgrounds from prompt gamma rays and scattered fission neutrons. The detectors in concert with the DAQ also managed to collect good data with a count rate greater than 10 kHz per bar. The robustness of the detectors could allow for more forward angle measurements, where the accidental rates will be higher. A limiting factor for this experiment was the analog DAQ. The 16 bars required over a thousand lemo and BNC connections and dozens of NIM modules. Future measurements will require a digitized DAQ, which will not only reduce the burden during setup but also allow for new methods of analysis. Potentially the 2D cut which was used for the ^{252}Cf analysis could also be introduced with digitized data.

The MCNP simulations were an excellent way of analyzing the response of the bars to neutrons and gamma rays. While MCNP did not handle scintillation light propagation, a pre-processor code was developed to handle that last step. The simulations showed how bar-to-bar scattering as well as floor to bar scattering affected the result. It is also possible to extract a response function from the simulated data and decouple the detector efficiency from our PFNS result. Then using MCNP's custom source option to insert the MN model into the simulation also proved to be an effective way to compare the measured result to the theory. Using high statistics singles data to predict the accidental background generates a low uncertainty background for subtraction. It also does not require any form of normalization, as the method not only predicts the shape but also the magnitude of the background.

Appendices

A Neutron Bar Repair

We repaired and tested 12 of our neutron bars. The bar ends repaired were: 3, 5, 7, 8, 13, 17, 19, 20 top, and 4, 11, 14, 15 bottom. This appendix outlines this process.

A.1 Repair

The damaged bars were brought to the 2nd floor lab in the Chemistry-Physics Building and inspected to see the extent of the damage. Typically, only the light guide had become separated from the scintillator. However, some bars also had loose photomultiplier tubes (PMTs). The light guide and scintillator were then both sanded using a grit progression of 240, 320, and 400. Once sanding was completed the glue was mixed. The optical cement mixture was 100 parts St. Gobain BC-600 resin and 28 parts hardener. Overall, we made about 4 grams of total mass. After carefully applying the cement, the bar was placed on top of the light guide in a specially made stand such that the weight of the bar rested on the new glue joint. A bar in the stand can be seen in figure A.1. After approximately 72 hours the bar was removed from the stand and tested.

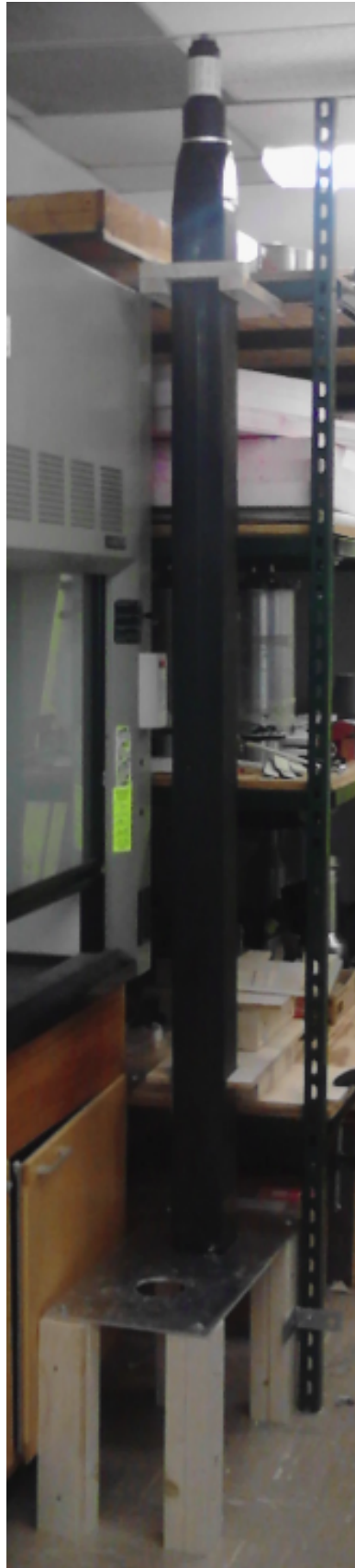


Figure A.1: Completed bar stand. The weight of the bar puts pressure on the glue joint. This pressure helps the glue to fill in scratches and form a more uniform interface.

A.2 Bar Testing

The new glue joint was wrapped in aluminum foil and black electrical tape. The bar was then tested to see if it was light tight. To test for light leaks the bar was covered with a black towel and raised to a voltage of 1000 V. Then it was slowly raised to 1500 V, monitoring the output on a scope to ensure the tube was not saturating. When the desired voltage of 1500 V was reached, the bar was slowly uncovered its response was monitored with an oscilloscope. As the bar was uncovered if there was a change in the response on the scope it meant a light leak was near the area that had just been uncovered. To find the exact spot a flashlight was used. When the flash light would shine on the leak the response on the scope would increase accordingly. This method was used to pinpoint the leak. Whenever a leak was found, black electrical tape was used to cover it. After the bar was found to be light tight, it was set on a workbench, as shown in figure A.2.

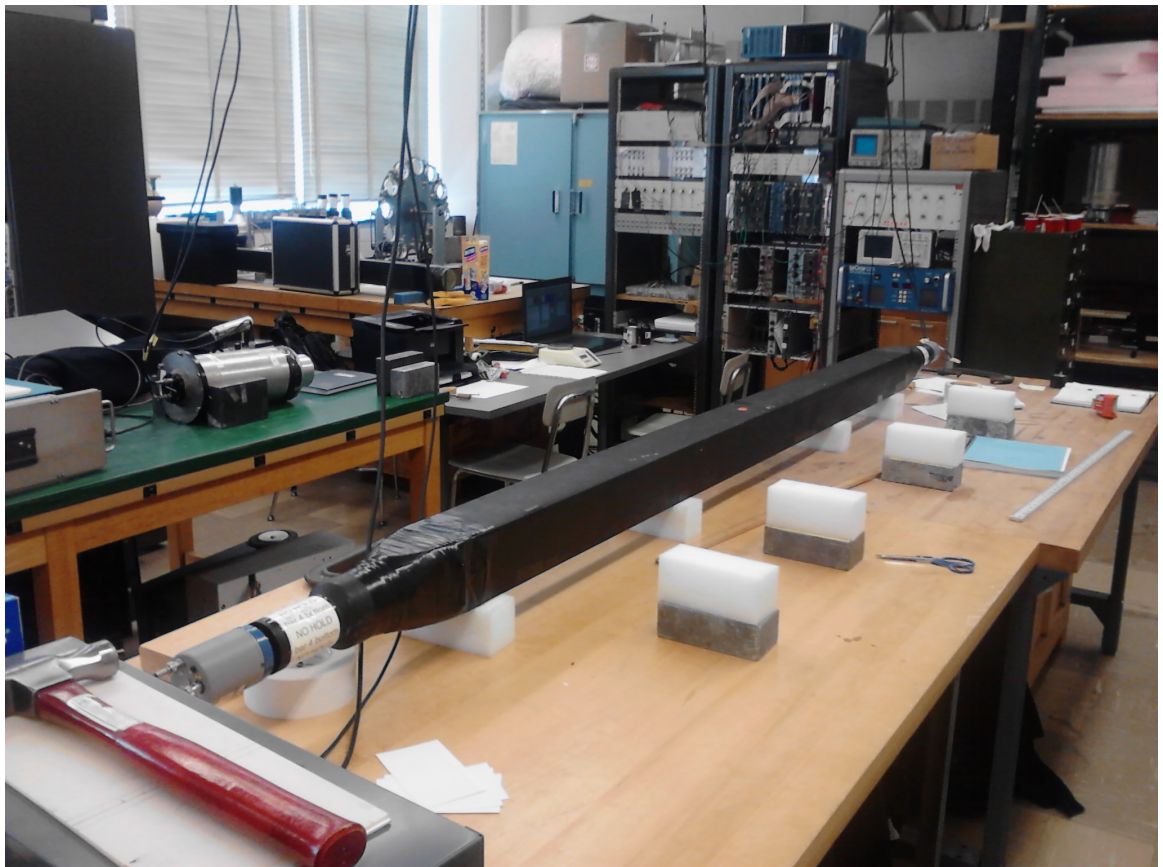


Figure A.2: A bar on the bench ready for gamma ray testing.

The bar was placed on foam blocks to make it easier to handle and to help keep the bar level. Once set up on the table, the bar was tested for light leaks, and its response to various sources was measured. To test the bar's gamma response a ^{228}Th was placed on the center of the bar. The voltage of each PMT would then be adjusted such that the 2.38 MeV Compton edge lined up with roughly 1000 channels above pedestal. At this point the spectrum of each PMT was compared to ensure they were the same. If it was impossible to get the spectrum of both PMTs to be similar than something was wrong with one of the two sides. However, this situation was never observed. To make the 2.38 MeV edge stand out in the single PMT spectrum, a center of bar cut was used. A ^{228}Th spectrum with and without a center cut, are shown in figure A.3.

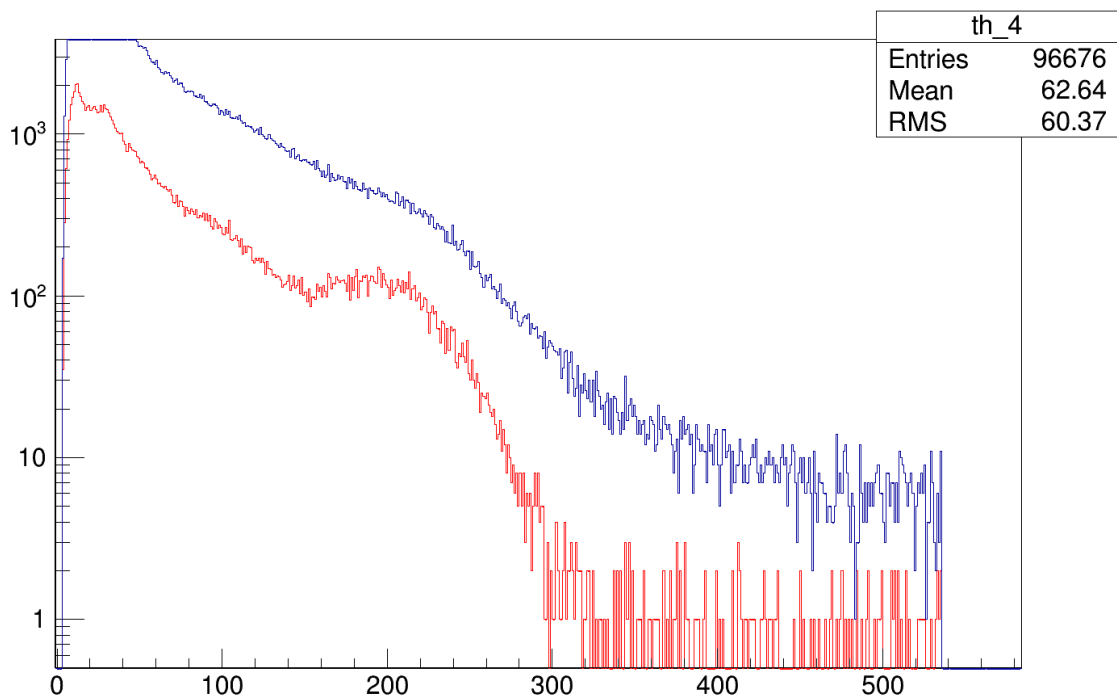


Figure A.3: Overlay of ^{228}Th spectra with (red) and without (blue) a center-cut. The pronounced feature just above 200 channels in the red center-cut spectrum is the 2.38 MeV Compton edge of ^{228}Th .

We then moved on to tested the bar with a ^{22}Na source. A BGO detector was placed near the center of the bar with a perpendicular distance of 1 m. A sketch of the setup is seen in figure A.4.

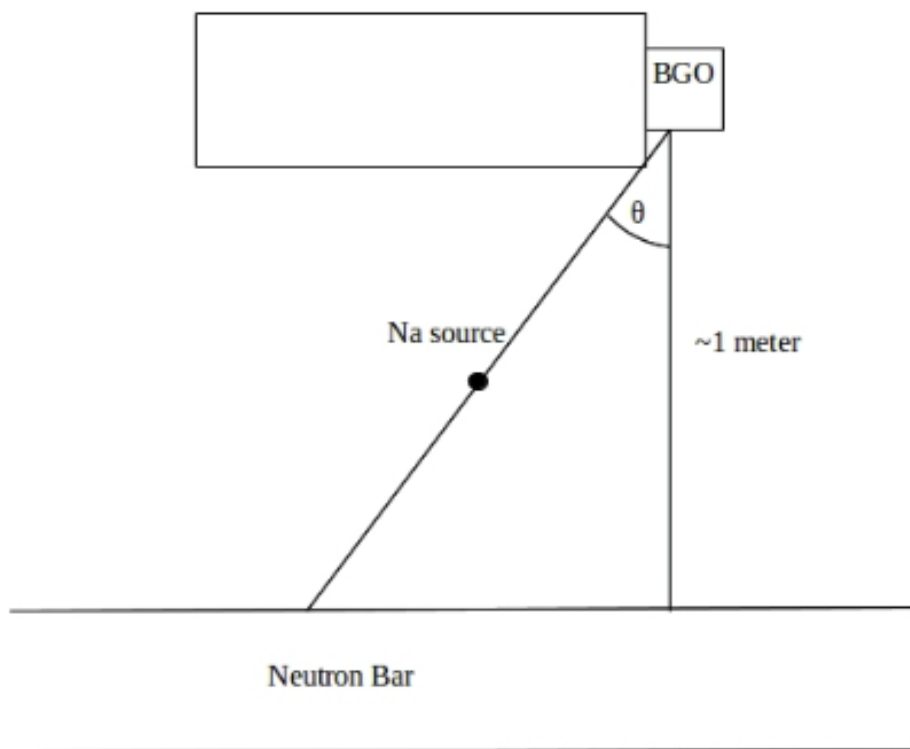


Figure A.4: The ^{22}Na source is placed halfway between the BGO and neutron bar.

The ^{22}Na source emits back-to-back 511 keV gamma rays. By placing the source in-between the bar and BGO, back-to-back coincidence events are measured. By placing the Na source at various angles relative to the bar face normal, the response is measured at various positions along the bar. A ^{22}Na spectrum is shown in figure A.5.

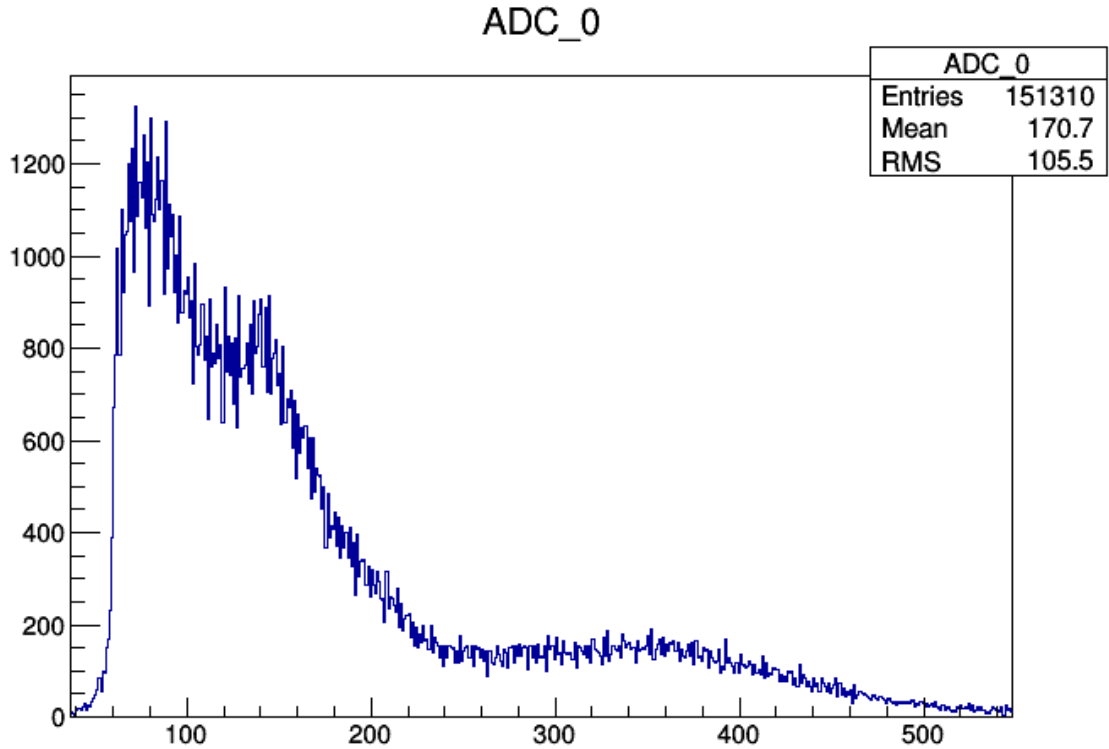


Figure A.5: ^{22}Na spectrum at center of bar. The 340 keV Compton edge is around channel 180, and the 1068 keV Compton edge is near channel 400.

B Neutron Bar Stand

B.1 Stand Design Specifics

A support stand designed to hold the weight and configuration our our 16 neutron bars is outlined in this section. The neutron bar stand had to meet a few criteria. It needed to bear the weight of 16 neutron bars. The stand had to be as light-weight as possible to reduce both neutron and gamma ray scattering. No substantial part of the stand could be directly between the neutron bars and PPAC. To accomplish these goals aluminum unistrut was chosen to build the bulk of the support stand. Aluminum unistrut is lightweight, easy to work with, and aluminum has a smaller neutron and gamma ray scattering cross section than steel. Finally to hold the bars in a useful configuration arc shaped aluminum plates were designed. These arcs had a series of 11.5 cm long flats. These flats are what the neutron bars rested on. The midpoints of these flats formed an arc with a radius of curvature

of 1500 mm. Sources were placed at the center of this arc so that the center of each bar was 1500 mm from the source. A sketch of these plates can be seen in figure B.1.

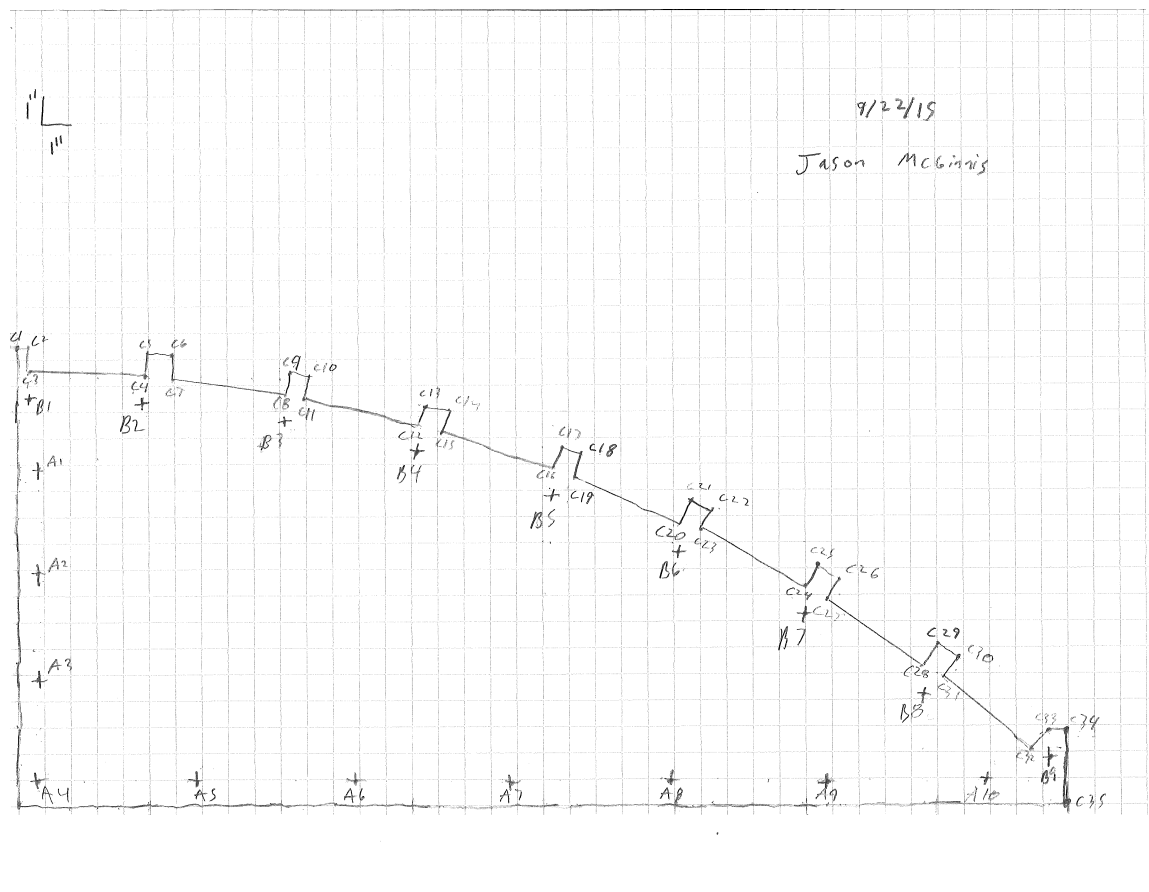


Figure B.1: Bar holding aluminum plate.

Two pairs of these plates were made, with each pair forming an arc. The radius of curvature, for the midpoints of each flat, is 1500 mm. The plates were cut out of sheets of aluminum using an automatic milling machine. This machine needed an autoCAD schematic to know where to cut the aluminum and where to drill holes. The numbers and letters in the sketch represent labels for coordinates. The “A” points represent holes drilled for bolts that attach the plate to the support stand. The “B” points are holes for a rope to pass through to help hold the bars in place. The “C” points represent an outline of the plate that the milling machine cut around. The support stand was designed in such a way that these plates support the scintillator section of the bar on both ends. This was done to reduce stress on

the glue joint.

The basic outline of the support stand can be seen in figure B.2.

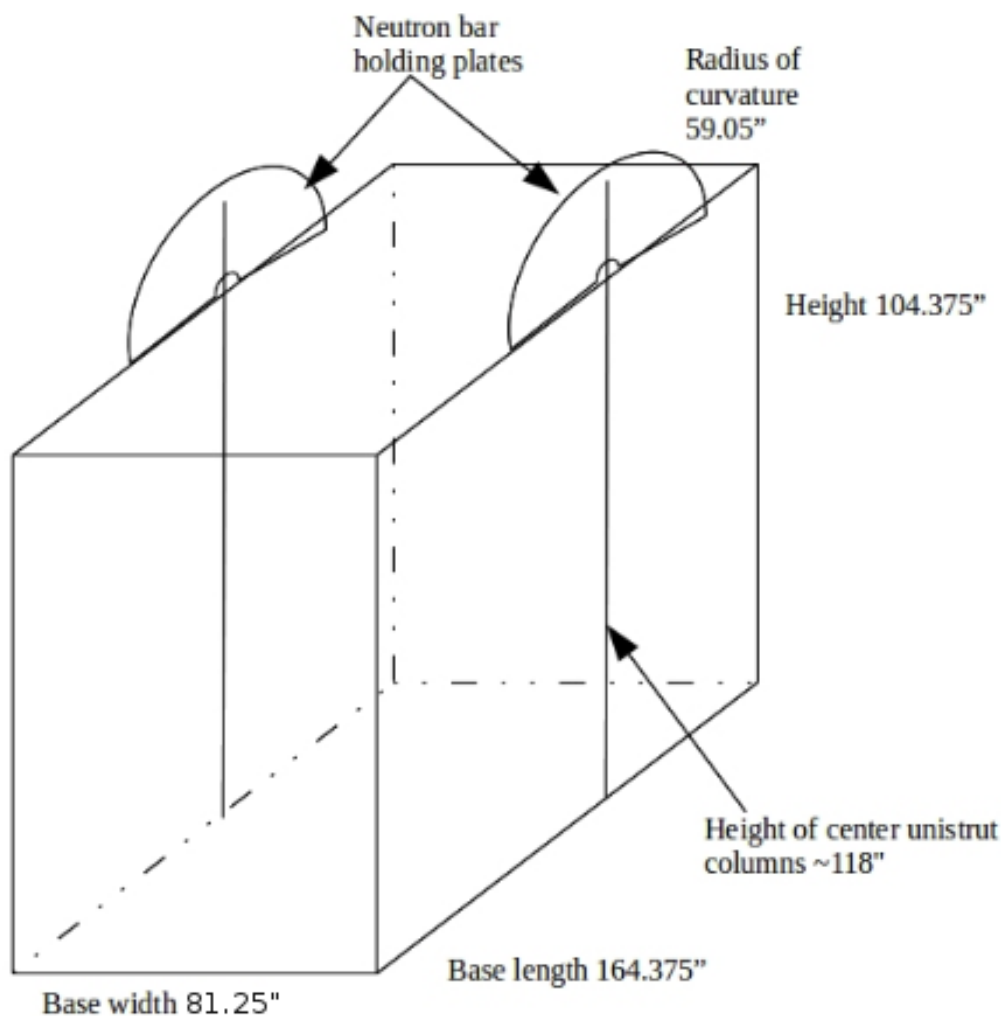


Figure B.2: Support stand. Not shown are the corner supports and cross wires. Each line represents an aluminum unistrut channel, and the two arcs represent the aluminum bar holding plates.

In the center, along the length of the base, are two strut channels 118" long. These channels help support the arc-shaped aluminum plates. The bars span 80" across the middle of the support stand. The stand is 164" wide. This width allowed for 42" of space on either side of the bars. This space allowed for corner supports that do not come between the neutron bars and any source placed in the center of the arc. Each of these corner support configurations is identical so an

example corner is drawn in figure B.3.

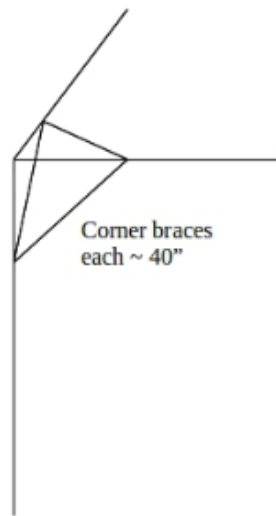


Figure B.3: Corner example. Note each corner support channel is the same length, 1 meter. These corner supports were designed to prevent twisting of the support stand.

Once the stand was assembled two wires were strung across each face forming an “X” or cross. These wires were then put under tension to ensure the stand was properly aligned and stayed that way. Six bars placed in a completed stand are shown in figure B.4.

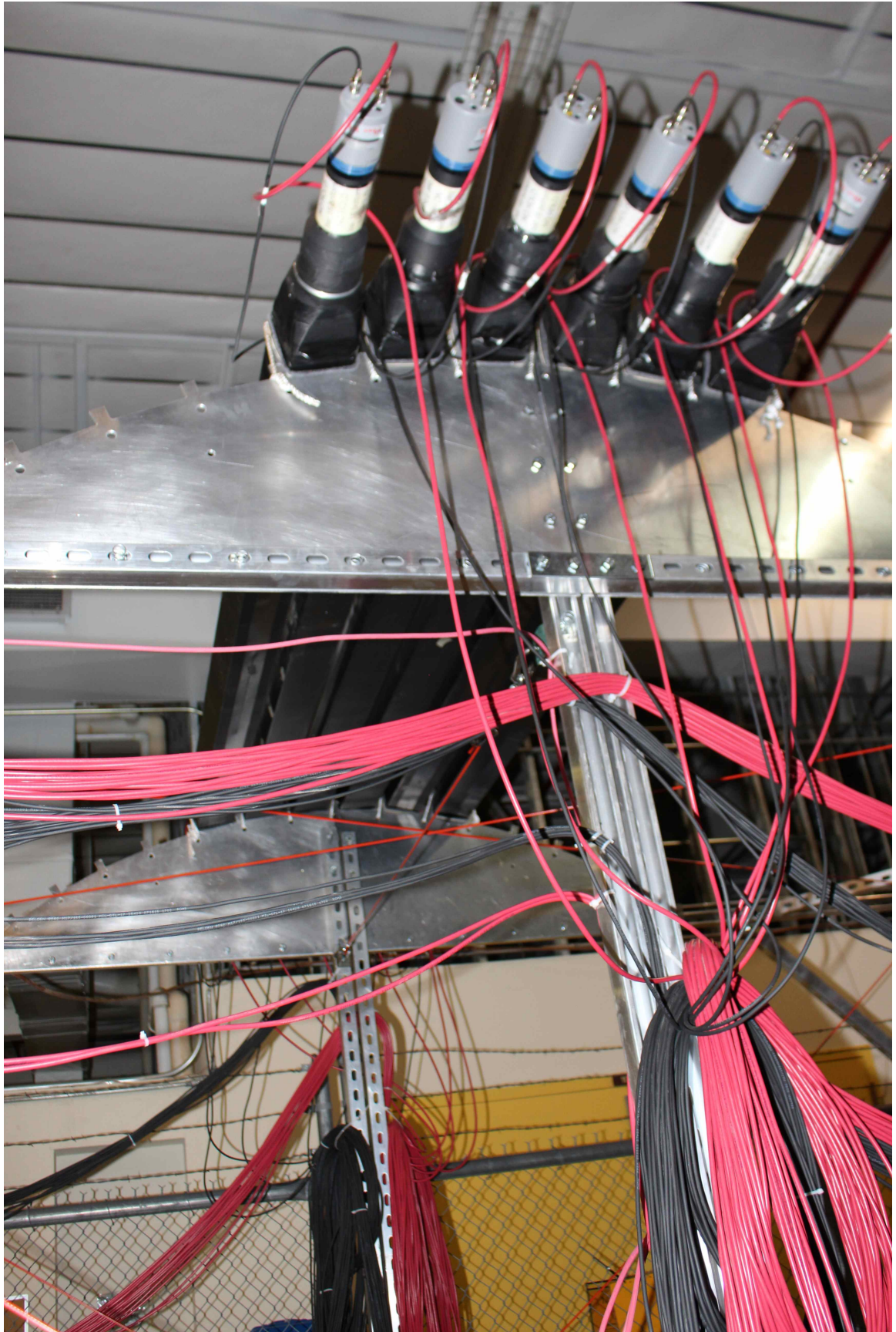


Figure B.4: Finished stand with 6 neutron bars. The aluminum holding plates are seen beneath the bars.

C Proton Recoil

In order to do the simulations of the bars, the proton recoil light response function was needed. To find this function an experiment was carried out using a detector made of the same material as the bars. This detector is referred to as the active target (AT), which was 2.5" square and 6 mm thick. The AT had two phototubes – one at each end of the plastic scintillator, similar to the bars. A second neutron detector (referred to as the 5" detector) was used to detect scattered neutrons. This detector was 5" in diameter and used liquid organic scintillator to detect neutrons. The experiment took place at the UK Van de Graff accelerator and used a 4 MeV deuteron beam incident on a deuterium gas cell target. This created 7.263 MeV neutrons via the $d(d,^3\text{He})n$ reaction. The AT was placed just 13 cm from the deuterium gas cell target to maximize the count rate and ensure the AT was placed directly above the pivot of the movable shielding assembly. The 5" detector was placed on the movable shield assembly which allowed for measuring various neutron scattering angles. The movable shield assembly also shielded the 5" detector from direct beam neutrons and gamma rays. Due to the acceptance of the 5" detector only five scattering angles were needed to cover the scattered neutron energy range from 1 to 5 MeV. The scattering angles were 65°, 56°, 48°, 40°, and 32°, each with a runtime of 9 hours. Figure C.1 shows a sketch of the detector layout.

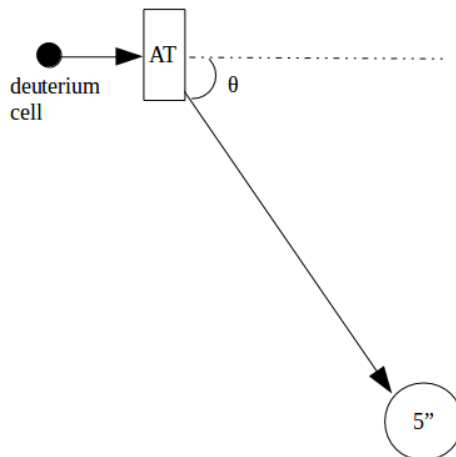


Figure C.1: Sketch of detector setup at the UK Van de Graff. The distance from the deuterium cell to AT is 13 cm, and the distance from the 5" diameter liquid organic neutron detector is 178.5 cm.

The DAQ for this experiment measured the pulse height of both AT PMTs, and the 5" detector. The DAQ also measured the TOF of beam neutrons to the AT and the TOF of scattered neutrons from the AT to the 5" detector. The AT acted as the trigger for the DAQ. When an incident neutron scattered in the AT, it would detect the recoiling proton and measure the pulse height. The AT's pulse height ADCs were calibrated to keVee using the 340 keV and 1068 keV Compton edges of ^{22}Na . The 5" detector would detect the scattered neutrons and record their TOF t_s relative to the AT trigger. The energy of the scattered neutrons via TOF T_s is calculated with equation 6.1 with the flight path (FP) of 178.5 cm.

$$\beta = \frac{FP}{c * t_s}$$

$$\gamma = \frac{1}{\sqrt{1 - \beta^2}} \quad (6.1)$$

$$T_s = (\gamma - 1)M_n$$

Since the beam was mono-energetic the energy difference between the beam energy of 7.263 MeV and the energy of the scattered neutron T_s is the proton recoil energy. Figure C.2 shows the result of this experiment.

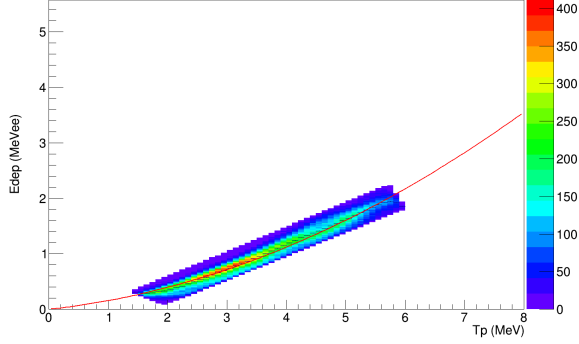


Figure C.2: Proton recoil vs energy deposition with an AT trigger and beam TOF cut. The red curve is the fitted function.

The red curve shows the quadratic fit function and is the function used to convert from MeV to MeVee in the pre-processor code used to propagate light for the MCNP simulations. The MeV to MeVee proton recoil fit function is given by equation 6.2.

$$E_{MeVee} = 2.01 * 10^{-5} * E^2 + 0.330 * E \quad (6.2)$$

This method to measure the proton light response was simple and collected data at a rate faster than anticipated. With that same amount of time it would have been possible to take data at shallower angles, where the proton recoil light response is less linear, without sacrificing much in the way of precision in the energy range 1-5 MeV.

D Fermi-Gas Model Calculation of the Level Density a

The Fermi-gas model description of neutrons in a nucleus models the neutrons as a gas made up of non-interacting fermions. The number of macro-states depends on the number of neutrons and the excitation energy. A combinatorial approach is employed to count the number of states[19]. Let N fermions be divided among the single-particle states k , with the occupancy n_k of 0 or 1, then $N = \sum_k n_k$. If the energy states are of the form $\epsilon_k = k * \epsilon_1$, then the total energy is given by

equation 6.3.

$$\sum_k n_k \epsilon_k = E_0^N + E^* \quad (6.3)$$

Where E_0^N is the ground state energy of the system and E^* is the excitation energy of the nucleus. The ground state energy is calculated by occupying sequential energy states starting at ϵ_1 and ending with ϵ_N , giving equation 6.4.

$$E_0^N = \epsilon_1 N^2 / 2 \quad (6.4)$$

Let $W(K)$ be the number of configurations of the set n_k that add up to the integer K , with the value of K given by equation 6.5.

$$\frac{E^*}{\epsilon_1} \quad (6.5)$$

The density of states is then obtained by summing over all states k , shown in equation 6.6.

$$\rho(E^*) = \sum_k W(k) \delta(E^* - k\epsilon_1) \quad (6.6)$$

The value of $W(K)$ is approximated by equation 6.7[19].

$$W(K) = \frac{1}{\sqrt{48K}} \exp\left(\pi \sqrt{\frac{2K}{3}}\right) \quad (6.7)$$

Combining equations 6.6 and 6.7 with the level density parameter a we get the density of states as a function of E^* given by equation 6.8.

$$\rho(E^*) = \frac{1}{\sqrt{48E^*}} \exp(2\sqrt{a * E^*}) \quad (6.8)$$

The level density $\rho(E^*)$ defines the nuclear temperature T by equation 6.9.

$$\frac{d \ln(\rho(E^*))}{dE^*} = \frac{1}{T} \quad (6.9)$$

Which simplifies to the familiar equation 6.10.

$$E^* = aT^2 \tag{6.10}$$

Bibliography

- [1] K.S. Krane. *Introductory Nuclear Physics*. Wiley, 1987.
- [2] Neutron proton asymmetry energy difference sketch. https://en.wikipedia.org/wiki/Semi-empirical_mass_formula, .
- [3] Coulomb barrier sketch. <http://www.pas.rochester.edu/~blackman/ast104/reactions.html>, .
- [4] J.R.Nix D.G.Madland. New calculation of prompt fission neutron spectra and average prompt neutron multiplicities. *Nuclear Science and Engineering*, 81:213–271, 1982.
- [5] Weisskopf. Statistics and nuclear reactions. *Phys. Rev.*, 52:295, 1937.
- [6] H.A. Bethe. An attempt to calculate the number of energy levels of a heavy nucleus. *Physical Review*, 50:332, year=1936.
- [7] J. Terrell. Neutron yields from individual fission fragments. *Phys. Rev.*, 127: 880, 1962.
- [8] Mark B Chadwick Denise Neudecker Michael E Rising Patrick Talou, Toshihiko Kawano. Uncertainties in nuclear fission data. *Journal of Physics G*, 42: 034025, 2015.
- [9] R. O. Nelson M. Devlin J. M. O'Donnell A. Chatillon T. Granier G. Bélier J. Taieb T. Kawano S. Noda, R. C. Haight and P. Talou. Prompt fission neutron spectra from fission induced by 1 to 8 mev neutrons on ^{235}u and ^{239}pu using the double time-of-flight technique. *Physical Review C*, 83:034604, 2015.

- [10] St. gobain bc-408 product page. <https://www.crystals.saint-gobain.com/products/bc-408-bc-412-bc-416>.
- [11] C. Jiang. Precision measurement of neutron-neutron scattering length a_{nn} via $\pi^-d \rightarrow \gamma nn$. *Univeristy of Kentucky*, 1996.
- [12] S. CHIBA T. FUKAHORI M. HARADA, Y. WATANABE. Evaluation of neutron cross sections of carbon-12 for energies up to 80mev. *Nuclear Science and Technology*, 34:2:116–127, 1997.
- [13] R.C.Haight H.Y.Lee T.N.Taddeucci B.Bucher A.Chyzh M.Devlin N.Fotiades E.Kwana J.M.O'Donnell B.A.Perdue J.L.Ullmann C.Y.Wu, A.Henderson. A multiple parallel-plate avalanche counter for fission-fragment detection. *Nuclear Instruments and Methods Section B: Beam Interactions with Materials and Atoms*, 794:76–79, 2015.
- [14] N. Fukuda H. Takeda D. Kameda N. Inabe K.Yoshida T.Kubo H. Kumagai, T. Ohnishi. Development of parallel plate avalanche counter ppac for bi-grips fragment separator. *Nuclear Instruments and Methods Section B: Beam Interactions with Materials and Atoms*, 317:717–727, 2013.
- [15] Lances website. <https://lansce.lanl.gov>.
- [16] J.M.O'Donnell. A new method to reduce the statistical and systematic uncertainty of chance coincidence backgrounds measured with waveform digitizers. *Nuclear Instruments and Methods in Physics Research A*, 805:87–94, 2016.
- [17] J.B. Birks. Proceedings of the physical society. section a scintillations from organic crystals: Specific fluorescence and relative response to different radiations. *Proceedings of the Physical Society. Section A*, 64(10):874–877, 1951.
- [18] M.L. Fensin et al. J.T. Goorley. *MCNP6 User's Manual Ver. 1*. 2013.
- [19] J.R. Engelbrecht C.A. Engelbrecht. Fermi gas descriptions of nuclear level densities. *Annales of Physics*, 207:1–37, 1991.

- [20] Mcnp summary page. <https://mcnp.lanl.gov/>.
- [21] A. Brown R.C. Haight C.M. Layon T.M. Lee P.W. Lisowski W. McCorkle R.O. Nelson S.A. Wender, S. Balestrini and W. Parker. A fission ionization detector for neutron flux measurements at a spallation source. *Nuclear Instruments and Methods in Physics Research Section A: Accelerators, Spectrometers, Detectors and Associated Equipment*, 336:226–231, 1993.

Vita

Jason M. McGinnis

EDUCATION

University of Kentucky

Lexington, KY

M.S., Physics

December 2015

Morehead State University

B.S., Physics

May 2013

PROFESSIONAL POSITIONS

Teaching Assistant

University of Kentucky, Dept. of Physics and Astronomy

2013-2015 2018-2019

Research Assistant

University of Kentucky, Dept. of Physics and Astronomy

2015-2018